Physics, Astrophysics and Applied Physics PhD School
Università degli Studi di Milano

Arenberg Doctoral School - Faculty of Physics
KU Leuven

Cluster-transfer reactions with radioactive beams:

a spectroscopic tool for neutron-rich nuclei

Author: Simone Bottoni

Supervisors:
Prof. Silvia Leoni
Prof. Riccardo Raabe
Co-Supervirsor:
Prof. Angela Bracco

Academic year 2014-2015

Commission of the final examination

Prof. Angela Bracco
Prof. Silvia Leoni
Prof. Riccardo Raabe
Prof. Nathal Severijns
Prof. Piet Van Duppen
Prof. Andrea Vitturi

Final examination

26/01/2015
Università degli Studi di Milano, Dipartimento di Fisica - Milano - Italy

Co-operation Agreement for a Joint Doctorate between:
Università degli Studi di Milano
KU Leuven

Università degli Studi di Milano
Dipartimento di Fisica
Corso di Dottorato in Fisica, Astrofisica e Fisica Applicata
Ciclo XXVII
Coordinator: Prof. Marco Bersanelli

MIUR subject: FIS/04 - FISICA NUCLEARE E SUBNUCLEARE

PACS: 25.70.Hi, 29.30.Kv, 21.10.Re

Celestijnenlaan 200D box 2418, B-3001 Heverlee (Belgium)

D/2015/10.705/3
ISBN 978-90-8649-793-5

Dissertation presented in partial
fulfilment of the requirements
for the degree of Doctor in Science.

Alla mia mamma

To my Mum

L'arte e la scienza sono libere e libero ne è l'insegnamento.

Costituzione Italiana, Art. 33, Comma 1

The arts and sciences are free as is their teaching.

Italian Constitution, Art. 33, Paragraph 1

Contents

Summary

In this thesis work, an exploratory experiment to investigate cluster-transfer reactions with radioactive beams in inverse kinematics is presented. The aim of the experiment was to test the potential of cluster-transfer reactions at the Coulomb barrier, as a possible mean to perform γ spectroscopy studies of exotic neutron-rich nuclei at medium-high energies and spins. The experiment was performed at ISOLDE (CERN), employing the heavy-ion reaction ^{98}Rb+^{7}Li at 2.85 MeV/A. Cluster-transfer reaction channels were studied through particle-γ coincidence measurements, using the MINIBALL Ge array coupled to the charged particle Si detectors T-REX. Sr, Y and Zr neutron-rich nuclei with A $\approx$ 100 were populated by either triton- or α transfer from ^{7}Li to the beam nuclei and the emitted complementary charged fragment was detected in coincidence with the γ cascade of the residues, after few neutrons evaporation. The measured γ spectra were studied in detail and the residue distributions were investigated as a function of the excitation energy and different spin distributions of the nuclei produced in the cluster-transfer process. Moreover, the reaction mechanism was qualitatively studied as a two-body process, considering the direct transfer of a cluster-like particle and using a Distorted Wave Born Approximation (DWBA). The results of this work show that cluster-transfer reactions can be well described as a direct process and that they could be considered for the population of neutron-rich nuclei at medium-high energies and spins. The same experimental technique can therefore be used in future experiments to study different exotic regions of the nuclides chart using radioactive ion beams of new generation.

Riassunto

In questo lavoro di tesi viene presentato un esperimento finalizzato allo studio di reazioni di trasferimento di cluster di nucleoni con fasci radioattivi in cinematica inversa. Scopo dell'esperimento è testare questo meccanismo di reazione alla barriera Coulombiana per popolare nuclei esotici ricchi di neutroni a energie e spin medio-alti. L'esperimento è stato condotto presso ISOLDE (CERN), studiando la reazione tra ioni pesanti ^{98}Rb+^{7}Li a 2.85 MeV/A. I canali di reazione di interesse sono stati investigati tramite misure di coincidenza particella-γ, grazie ad un setup sperimentale costituito da un array di rivelatori al Ge, MINIBALL, acccopiato ad un rivelatore al Si, T-REX, per la rivelazione di particelle cariche. Nuclei di Sr, Y e Zr ricchi di neutroni con A $\approx$ 100 sono stati prodotti attraverso il trasferimento di un tritone o di una particella α e la particella carica complementare emessa è stata rivelata in coincidenza con la cascata γ dei nuclei residui, dopo l'evaporazione di alcuni neutroni. Gli spettri γ misurati sono stati analizzati in dettaglio e le distribuzioni dei nuclei residui sono state studiate in funzione dell'energia di eccitazione e di diverse distribuzioni di spin. Inoltre, il meccanismo di reazione è stato studiato qualitativamente utilizzando un modello a due corpi e considerando il trasferimento diretto di un cluster in approssimazione di Born in onde distorte (DWBA). I risultati di questo lavoro mostrano che reazioni di trasferimento di cluster di nucleoni possono essere utilizzate per produrre nuclei ricchi di neutroni ad energie e spin medio-alti e che il meccanismo di reazione può essere qualitativamente interpretato come un processo diretto. La stessa tecnica sperimentale potrà essere usata in esperimenti futuri per esplorare diverse regioni esotiche della tavola dei nuclidi, utilizzando fasci radioattivi di nuova generazione.

Samenvatting

In dit werk wordt een nieuwe experimentele benadering voorgesteld om cluster-transfer reacties te onderzoeken met radioactieve bundels in inverse kinematica. Het doel van het experiment was het potentieel te testen van het gebruik van cluster-transfer reacties voor de spectroskopische studie van exotische neutron-rijke kernen bij medium-hoge energieën en spins. Het experiment werd uitgevoerd in ISOLDE (CERN), gebruikmakend van de zware-ionen reactie ^{98}Rb+^{7}Li bij 2.85 MeV/A. De cluster-transfer reactie kanalen werden bestudeerd door middel van deeltje-coincidentie metingen met de MINIBALL germanium opstelling gekoppeld aan geladen-deeltje silicium detectoren T-REX. Sr, Y en Zr neutron-rijke kernen met A $\approx$ 100 werden gepopuleerd met tritium- of α-transfer van ^{7}Li naar de bundel kernen en het uitgezonden complementair geladen fragment werd gedetecteerd in coincidentie met de cascade van residus na weinig neutron evaporatie. De opgemeten spectra werden in detail bestudeerd en de verdelingen van de residus werden onderzocht in functie van de excitatie energie en de verschillende spin verdelingen van de kernen geproduceerd tijdens het cluster-transfer proces. Meer nog, het reactie mechanisme werd kwalitatief bestudeerd als een twee-lichamen proces, rekening houdend met de directe transfer van een cluster-achtig deeltje en met de Verstoorde Golf Born Benadering (DWBA). De resultaten van dit werk tonen aan dat cluster-transfer reacties goed kunnen beschreven worden als een direct proces en dat zij in aanmerking kunnen genomen worden voor de populatie van neutron-rijke kernen bij medium-hoge energieën en spins. Dezelfde experimentele techniek kan daarom in te toekomst gebruikt worden om verschillende exotische gebieden van de kernkaart te bestuderen aan de hand van radioactieve bundels van de nieuwe generatie.

Introduction

One of the central topic in modern nuclear physics is the study of the structure and decay modes of exotic nuclei, moving away from the valley of stability. Exotic nuclei are unstable systems, characterized by an N/Z ratio different from stable nuclei, being N and Z the number of neutrons and the number of protons, respectively. Exotic nuclei are not only a test bench for theoretical models aiming at a unified description of the nuclear many-body quantum system, but they are also fundamental for the understanding of the formation of the elements in the Universe [1–6].

In recent years, the study of exotic nuclei has progressed substantially, due to the possibility of accelerating radioactive beams [3,7], as well as to the development of sophisticated detection systems. Several types of reaction mechanisms have also been employed, allowing to investigate in detail the properties of these systems.

Experiments performed with stable beam-targets combinations have shown that multinucleon transfer reactions are a powerful tool to study moderately neutron-rich nuclei [8–11] and, in particular, cluster-transfer reactions can be used to populate states at medium-high spin and excitation energy [12–17]. ^{7}Li is especially suitable for this purpose, since it has a pronounced cluster structure with α and t particles as components [18]. Owing to a separation energy of 2.5 MeV, it easily breaks-up and one of the two fragments has a sizeable probability to be captured [19].

In this work, an exploratory experiment, aiming at the investigation of cluster-transfer reactions at the Coulomb barrier with radioactive beams, is presented as a possible spectroscopic tool for neutron-rich nuclei.

The experiment was performed at the ISOLDE facility [29] at CERN, by accelerating at 2.85 MeV/A a neutron-rich ^{98}Rb beam on a 1.5 mg/cm^2 thick LiF target. The aim of the experiment was to study the cluster-transfer reaction mechanism by performing spectroscopy studies of neutron-rich Sr, Y and Zr nuclei with A $\approx$ 100. In fact, from the spectroscopy point of view, these nuclei have been investigated so far in β decay or spontaneous fission experiments only [20–28]. Cluster-transfer reaction channels were studied by particle-γ coincidences, using the MINIBALL-T-REX set-up [30–32], consisting of a Ge array coupled to a charged particle detection systems based on Si telescopes. This allowed to detect the emitted complementary charged particle in coincidence with the γ cascade of the residue, after few neutrons evaporation.

The reaction mechanism is also discussed in terms of a direct transfer of a cluster-like particle, using a simple one-step Distorted Wave Born Approximation (DWBA) [33] and the FRESCO code [34].

In Chapter 1, the importance of nuclear structure studies of neutron-rich nuclei will be briefly discussed. Cluster-transfer reactions as a possible mean to access medium-high energy and spin states in exotic nuclei will be presented, together with few results of cluster-transfer reactions with stable beams in direct kinematics. In the second part of the chapter, the theoretical model of transfer reactions will be presented, focusing on its applications to cluster-transfer reaction channels.

In Chapter 2, the experimental details will be presented. The ISOLDE facility at CERN as well as the detection system, consisting of the MINIBALL Ge array coupled to the charged particle detector T-REX, will be shown in details.

In Chapter 3, the experimental analysis performed in this work will be illustrated. Special attention will be given to particle-γ coincidences, the tool used in this experiment to perform spectroscopic studies of cluster-transfer reactions.

Chapter 4 is dedicated to the achieved results. First of all, the reactions channels observed in the experiment will be discussed in terms of γ spectroscopy and reaction dynamics. In particular, elastic and inelastic scattering, one-nucleon transfer, break-up and fusion-evaporation channels will be illustrated. The main part of this work is related to the analysis of cluster-transfer channels. Results of both triton- and α transfer will be presented and the γ spectroscopy results will be discussed in terms of excitation energy and populated spins.

The analysis of the neutron evaporation following the transfer process will be also illustrated. The residue distributions will be presented as a function of the excitation energy of the systems, following a two-body kinematics approach, and of different spin distributions. In the second part of Chapter 4, the cluster-transfer reaction dynamics will be discussed, assuming a direct transfer of a cluster-like particle and using a DWBA approximations. Two models will be illustrated: a weakly-bound approximation to describe the states in the final mass partition, as well as a proper discretization of the continuum.
In the Conclusions, the possibility of using cluster-transfer reactions with other radioactive ion beams will be discussed and few physics cases that might take advantages of this technique will be illustrated.

CHAPTER 1

Cluster-transfer reactions with radioactive beams

In this chapter, the physics motivation behind the work presented in this thesis will be discussed.

In the first part, cluster-transfer reactions with radioactive beams in inverse kinematics will be illustrated, as a possible mechanism to perform nuclear structure studies of exotic neutron-rich nuclei. In particular, their potential in connection with radioactive beams will be discussed, in parallel with results achieved in direct kinematics experiments with stable beams, paying attention to the experimental techniques used in this work.

In the second part, a theoretical introduction to transfer reactions will be given, focusing on the description of cluster-transfer processes.

1.1 Nuclear structure of exotic neutron-rich nuclei

The atomic nucleus is a many-body open quantum system made of protons and neutrons. Protons and neutrons, the nucleons, are interacting particles which are bound together by the attractive short-range nuclear force, which counterbalances the repulsive long-range Coulomb interaction between protons [35].

According to the N/Z ratio between the number N of neutrons and the number Z of protons, a nucleus can be either stable or unstable. In the former case, the N/Z ratio is such that the proton-neutron system is already at the equilibrium and it naturally occurs in the surrounding matter. In the ”chart of nuclides” of Fig. 1.1 stable nuclei are shown as black dots and form the so called ”valley of stability”. On the other hand, unstable nuclei tend to rich the equilibrium by changing their N/Z ratio decaying towards more stable systems, until the valley of stability is reached.

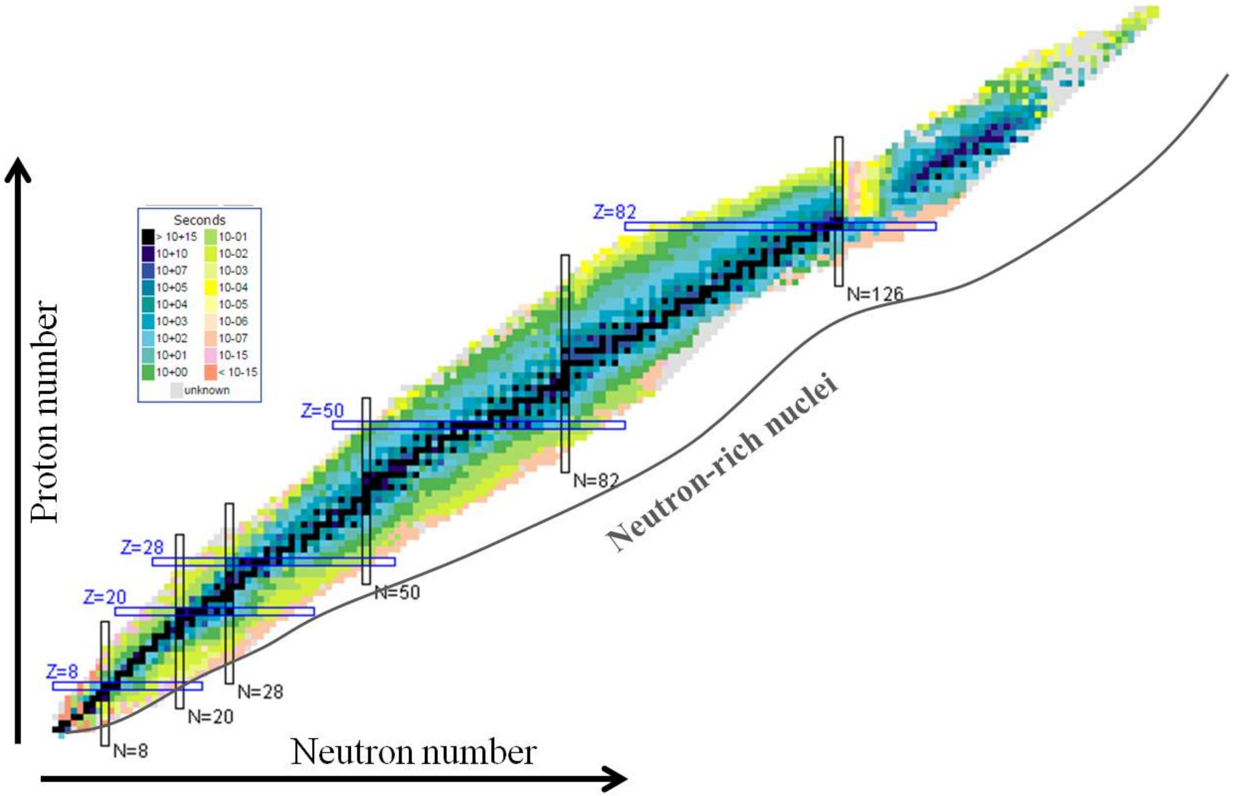

Figure 1.1: Chart of nuclides showing stable isotopes (black dots) and radioactive nuclei with a colour-code according to their lifetime, as given in the legend. The solid line shows the supposed location of the neutron-drip line, which defines the limit of existence of neutron-rich nuclei.

Such nuclei are called *radioactive isotopes* and those with a very different N/Z ratio compared to the corresponding stable isotopes are usually called *exotic nuclei*. These nuclei are characterized by a lifetime which becomes shorter and shorter moving away from the valley of stability. The known exotic nuclei are shown in Fig. 1.1 with a colour-code given in the legend, according to their lifetime. Exotic nuclei are usually called neutron-rich or neutron-deficient, depending on whether they have a neutron excess or a neutron deficiency with respect to stable nuclei at the valley of stability. Neutron-deficient nuclei are less extended than neutron-rich ones because of the Coulomb repulsion which quickly overcomes the attractive nuclear force, limiting the number of protons that can be added along an isotopic chain. Exotic nuclei exist within the limits of the so-called proton and neutron drip lines. Beyond these, nuclei undergo spontaneous proton and neutron emission, respectively. The exact location of the drip lines is an open problem of modern nuclear physics [6].

Among exotic nuclei, the neutron-rich ones are particularly interesting in terms of nuclear structure studies. It has been shown that theoretical models that well reproduce both the macroscopic and microscopic properties of stable isotopes have difficulties in describing the evolution of the nuclear structure towards the neutron-drip line [1,2,4,5]. For example, standard Shell Model descriptions turns out to be rather inadequate to predict the quenching of the classical "magic numbers" and to explain the appearance of new shell closures [2, 36]. This aspect is particularly interesting in connection with the observation of multiplets of states arising from the coupling between single particles and elementary modes of collective core excitations, which result quite robust around closed shells [35]. Moreover, as the number of neutrons increases, collective excitations may change as a result of sharp shape transitions from spherical to deformed configurations, as well as of different shape coexistences [37]. The excess of neutrons may also give rise to new collective excitations modes, as for example the Pigmy Dipole Resonance, characterized by the oscillation of the neutron excess (neutron skin) against the inert proton-neutron core [38].

Finally, the properties of neutron-rich nuclei are of particular interest in connection with Nuclear Astrophysics and nucleosynthesis. In fact, these studies may help to delineate the exact location of the rapid neutron capture process (r-process), which runs in the neutron-rich side of the chart of nuclides and it is responsible of the formation for all the elements heavier than Fe in the Universe [39].

For many years, the study of exotic nuclei was concentrated on the basic nuclear properties, such as masses, and ground state properties such as radii and electromagnetic momenta measurements [40,41]. Information on excited states were mainly obtained in β-decay experiments [42].

However, one of the main achievements in the last decade has been the development of accelerated radioactive ion beams which allowed to start exploring exotic regions of the chart of nuclides, not accessible otherwise, and to extend our knowledges about the structure of excited states in exotic systems [3,7]. In parallel, new experimental techniques are investigated to explore more and more exotic regions, including also reaction mechanisms not usually employed with stable beams.

In this thesis work, the potential of cluster-transfer reactions for populating neutron-rich nuclei at medium-high energy and spin is investigated.

1.2 Cluster-transfer reactions

Among multi-nucleon transfer reactions, cluster-transfer reactions result especially fascinating as a mechanism to access medium high-energy and spin states, being rather similar to a deep-inelastic process [19,43].

Cluster-transfer reactions are transfer reactions between heavy ions in which one of the colliding nuclei has a prominent cluster structure. It is typically a light weakly bound nucleus, such as ^{7}Li, which shows a α-t cluster structure with an α-t separation energy of 2.5 MeV [18]. During the collision, the weakly bound nucleus has a sizeable probability to break-up and one of the two fragments may be captured by the other nucleus [19]. This process is favoured at energies around the Coulomb barrier and below a critical value of angular momentum of the relative motion, such that the final system can survive against fission [13,44].

The best experimental technique that can be used to study the effectiveness of cluster transfer reactions as a spectroscopic tool relies on particle-γ coincidence measurements. In particular, the complementary emitted charged fragment is detected to select the reaction channel of interest, in coincidence with the γ-cascade following the de-excitation of the final products.

1.2.1 Cluster-transfer in direct kinematics

During the last two decades, cluster-transfer reactions induced by a weakly-bound nucleus with a cluster structure, such as ^{7}Li or ^{9}Be, have been exploited for γ-ray spectroscopic studies [12–17].

The success of these studies relied on the fact that cluster-transfer processes offer access to states at relatively high angular momentum in neutron-rich heavy nuclei, which are otherwise inaccessible by standard fusion evaporation reactions involving stable beam-target combinations. It has also been shown that in cluster-transfer processes it is possible to populate states with a significantly higher angular momentum than can be reached with ^{7}Li-induced fusion-evaporation reactions [12]. For example excited states in ^{125}Sb with spins up to 23/2 $\hbar$ have been studied following the ^{124}Sn(^{7}Li,α2n)^{125}Sb cluster-transfer at 37 MeV of beam energy [15].

The cross section of cluster-transfer reactions depends on the process of interest. It has been shown that in ^{7}Li-induced reactions, triton-transfer is favoured with respect to α-transfer, at energies around the Coulomb barrier. In Fig. 1.2, the excitation function for the reaction ^{7}Li + ^{209}Bi is presented, showing the contribution to the total fusion cross section given by the cluster-transfer channel, called incomplete fusion by the authors of Ref. [45]. It can be seen that cluster-transfer accounts for almost 300 mb at energies around the Coulomb barrier ($\approx$ 35 MeV). Fig. 1.3 shows the cross section for each cluster-transfer channel, in particular the triton-transfer case, corresponding to the emission of α particles. Since the transfer occurs at high excitation energy, neutron evaporation is also observed, and the 2n channel is found to be the one with the largest cross section.

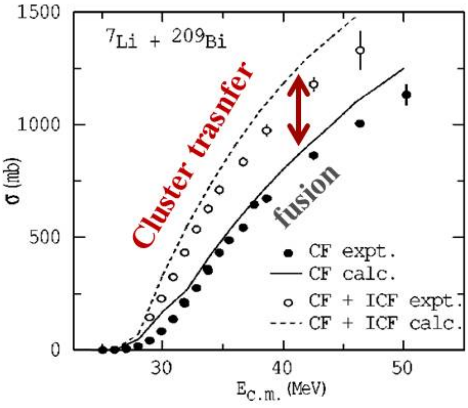

Figure 1.2: Excitation function for the ^{7}Li + ^{209}Bi reaction, showing the contribution due to the cluster-transfer channel (ICF) to the total fusion cross section (CF) [45].

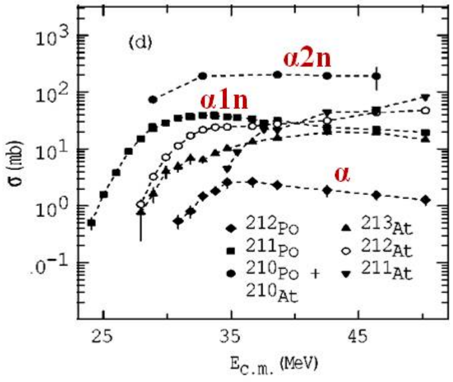

Figure 1.3: Cross section for cluster-transfer in the ^{7}Li + ^{209}Bi reaction, showing the contribution due to the neutron evaporation in coincidence with α particle (triton-transfer) [45].

1.2.2 Cluster-transfer with radioactive beams: the ISOLDE test case

The success of using cluster-transfer reactions in direct kinematics, as a spectroscopic tool, has suggested that this reaction mechanism may be used in experiments with accelerated radioactive beams to populate exotic neutron-rich nuclei at medium-high energy and spin. The aim of this work is therefore to study, for the first time, cluster-transfer reactions induced by radioactive beams, in connection with γ-spectroscopy of neutron-rich nuclei.

In this work, a test experiment, performed at ISOLDE [29] accelerating a radioactive neutron-rich ^{98}Rb beam at 2.85 MeV/A (the highest available energy at ISOLDE) on a ^{7}Li target is presented. The main goal of the experiment was the study of the cluster-transfer reaction mechanism with radioactive beams in inverse kinematics. As said in Sec. 1.2.1, cluster-transfer reactions were investigated, so far, in direct kinematics experiments only, using stable beam-target combinations. In the present work, to get insights into the reaction dynamics when accelerated radioactive neutron-rich nuclei are involved, total and differential cross sections are analysed in details, having in mind the possibility to exploit the same reaction mechanism with other neutron-rich radioactive beams in future experiments (see Conclusions).

From the spectroscopy point of view, the experiment explored the neutron-rich region around A $\approx$ 100, studied so far in β decay or spontaneous fission experiments only [20–28]. In this mass region, neutron-rich Kr, Rb, Sr, Y, Zr and Mo nuclei are expected to show a stable deformation at N = 60 [46]. The experimental measurement of the first 2^+ state energy in even-even isotopes of Kr, Sr, Zr and Mo is shown in Fig. 1.4 [47].

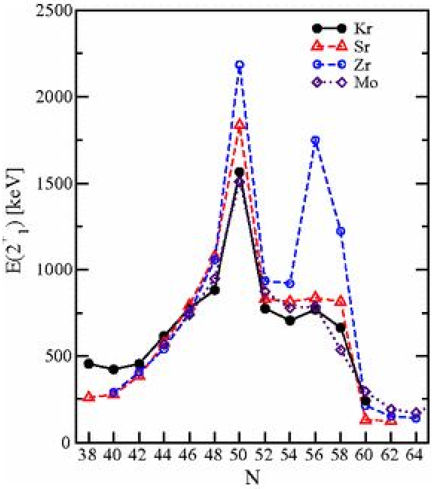

Figure 1.4: Experimental energy of the first 2^+ state in neutron-rich even-even isotopes of Kr, Sr, Zr and Mo [47].

In each isotopic chain, the energy of the first 2+ state shows a pronounced peak at N = 50, which is typical of a shell closure, where a large amount of energy must be given to promote particles to excited states. On the contrary, the onset of a deep minimum at N = 60 is a clear indication of a transition towards a well deformed shape, which is characterized by low energy excited states associated to the rotation of a deformed nucleus as a whole [35]. In the Zr case, a second peak is also observed at N = 56, while in Kr and Sr nuclei, with N $\approx$ 56, the 2^+ energies exhibit a rather smooth plateau. This can be interpreted as a partial neutron sub-shell closure in the transitional region between spherical and deformed shapes.

The employed experimental technique relies, as in the case of ^{7}Li-induced cluster-transfer reactions in direct kinematics, on the measurement of the complementary charged particle emitted in coincidence with the γ-cascade following the transfer. The simple structure of ^{7}Li (shown in Fig. 1.5 [18]), guarantees that the main reaction channels will be associated to either triton- or α-transfer to the beam nuclei, being the α-t binding energy 2.5 MeV only.

The transfer is expected to occur at high excitation energy, above the neutron threshold, therefore the evaporation of few neutrons is observed.

As a result, a number of neutron-rich isotopes will be produced after the transfer, allowing the study of more than one nucleus at the same time. The main advantages of the experimental technique can be summarized as follows:

- The very inverse kinematics of the reaction guarantees that the product nuclei all travel downstream in a very small recoil cone, thus Doppler reconstruction of the γ-ray data does not require recoil detection.
- Cluster-transfer channels of interest will be uniquely associated to the emission of an α particle or a triton (trition- and α-transfer, respectively). By detecting this particles, a very clean trigger will be produced for the ^{7}Li(^{98}Rb, αxnγ) and ^{7}Li(^{98}Rb, txnγ) processes.

To clarify the experimental technique, a schematic illustration of a triton-transfer reaction induced by an heavy ^A_ZX nucleus on a ^{7}Li target is given in Fig. 1.6 which shows the

$$^7\mathrm{Li}(^A_Z\mathrm{X}, \alpha 2\mathrm{n}\gamma)^{A+1}_{Z+1}\mathrm{X} \tag{1.1}$$

process, in which a heavy neutron-rich radioactive nucleus, such as ^{98}Rb, is accelerated on a ^{7}Li target.

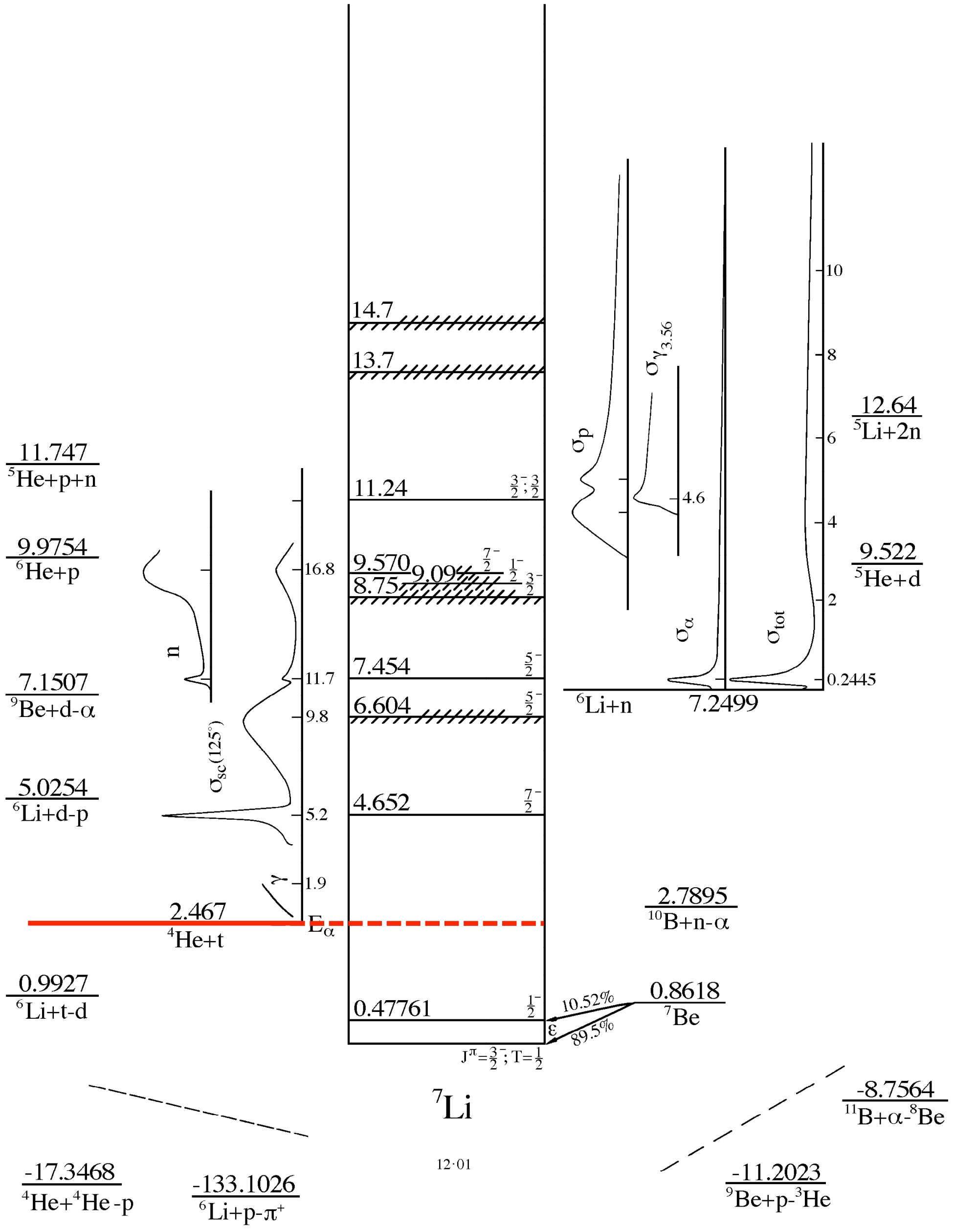

Figure 1.5: Level scheme of ^{7}Li [18]. The α-t binding energy at 2.467 MeV, relevant for this work, is indicated by a red line.

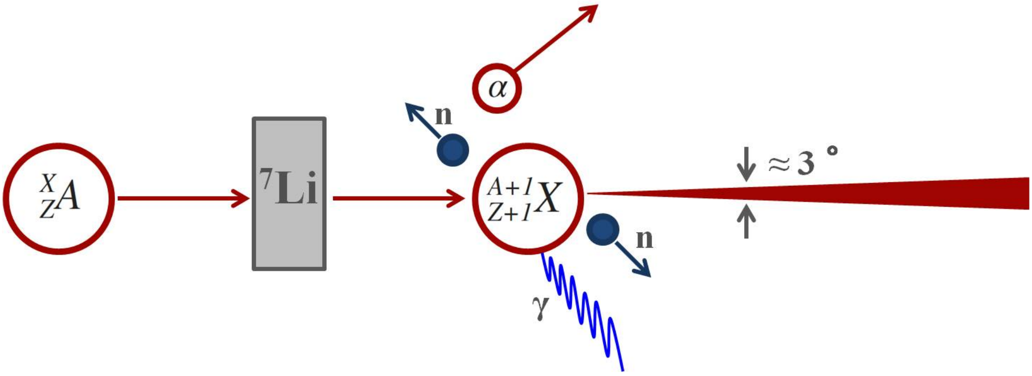

Figure 1.6: Schematic illustration of a triton-transfer reaction involving a heavy ^A_ZX nucleus and a ^{7}Li target. The emission of the α complementary fragment is followed by the evaporation of two neutrons and by the γ decay of the residue.

A triton is transferred to the beam and the α-particle is emitted. The system, after the transfer, decays by neutron evaporation (2n in the example) and afterwards by the γ cascade of the residue. As illustrated in the picture, the recoil travels in a very foreword-peaked cone, such that it can be assumed moving along the beam axis. In Fig. 1.7 the relation between the scattering angles of the recoil (heavy) and the ones of the emitted charged particle (light) can be seen for a typical triton-transfer process, like the one described in 1.1.

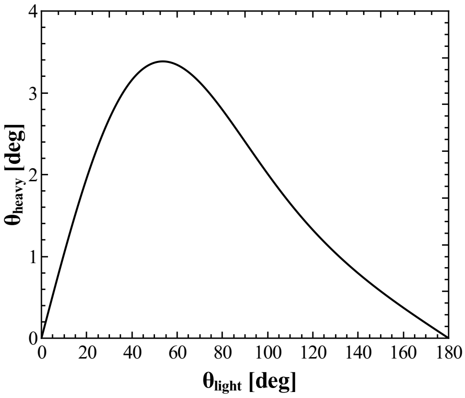

Figure 1.7: Scattering angle of the recoil (heavy) as a function of the angles of the emitted charged particle (light), for a typical triton-transfer process, like the one described in 1.1. The relation follows by the two-body kinematics (see App. A).

1.3 Theory of transfer reactions

In this section, the theory of transfer reactions will be presented, after a brief introduction to the scattering theory and to the one-channel scattering [33,48–50]. Particular attention will be given to the implications in the description of cluster-transfer reactions.

1.3.1 Scattering theory

The goal of the scattering theory is to provide a model to describe cross sections by solving the dynamical equations of the system with a realistic structure model of the colliding nuclei.

In a nuclear reaction an incident beam scatters from a potential V(R), giving rise to outgoing scattered waves. The center of mass coordinates can be chosen such that the beam is a plane wave with momentum $\hbar k_i$ along the +$\hat{\mathbf{z}}$ direction. The total wave function of the system Ψ is made by an incident plane wave and an outgoing scattered wave and, for large distances from the center of scattering, it satisfies the asymptotic form

$$\Psi(R,\vartheta,\varphi) \to e^{ik_i z} + f(\vartheta,\varphi)\frac{e^{ik_f R}}{R} \tag{1.2}$$

where $\hbar k_f$ is the momentum for the outgoing relative motion and R is the distance from the center of scattering. $f(\vartheta,\varphi)$ is the coefficient of the scattered waves, usually called *scattering amplitude*.

The angular distribution of the scattered particles is described by the differential cross section, namely the cross section as a function of the scattering angle. It is defined as the number of particle N scattered per unit of time , per unit of scattering center n and per unit of incident flux j_i, into a solid angle $\Delta\Omega$

$$\frac{dN}{dt} := j_i n \Delta\Omega\sigma \tag{1.3}$$

The cross section is therefore given by the coefficient σ in Eq. 1.3. The incident flux j_i is the number of particles per unit of time and per unit of area which is equivalent to the density probability of particles per unit of volume $|\psi|^2$ multiplied by the velocity $\mathbf{v}$. According to Eq. 1.2, j_i = v_i while the outgoing flux is j_f = $v_f|f(\vartheta,\varphi)|^2/R^2$. Assuming the scattered angular flux $\hat{j}_f = R^2 j_f$ and n = 1, the differential cross section defined as the ratio between the outgoing angular flux and the incident flux becomes

$$\frac{d\sigma}{d\Omega}(\vartheta,\varphi) = \frac{v_f}{v_i}|f(\vartheta,\varphi)|^2 \tag{1.4}$$

In general, if there is no dependence on the φ-angle in the incident beam (e.g. no dependence on the spin) and the scattering potential does not break the cylindrical symmetry of the incoming plane wave, then the cross section is also independent from the φ azimuthal angle. Since this is often the case, in the following discussion $f(\vartheta, \varphi) = f(\vartheta)$ will be assumed.

From Eq. 1.4, it can be seen that the scattering problem consists in determining the scattering amplitude $f(\vartheta)$. In order to do that, the Schrödinger equation

$$\left[-\frac{\hbar^2}{2\mu}\nabla_R^2 + V(R) - E\right]\Psi(R,\vartheta) = 0 \tag{1.5}$$

is solved, where μ is the reduced mass, V(R) is the interaction potential, E is the total energy and $\Psi(R,\vartheta)$ is the total wave function of the system which must satisfy the asymptotic form of Eq. 1.2.

1.3.2 One-channel scattering

If the scattering does not involve the internal degrees of freedom of the colliding nuclei, Eq: 1.5 describes the elastic scattering only. In this case, only one channel can be considered. The wave function $\Psi(R,\vartheta)$ is usually expanded in partial waves, such that the Schrödinger equation in three dimensions is reduced to a series of radial equations in one dimension, one for each L value of the angular momentum of the relative motion

$$\Psi(R,\vartheta) = \sum_{L=0}^{+\infty}(2L+1)i^L P_L(\cos\vartheta)\frac{1}{kR}\chi_L(R) \tag{1.6}$$

being ħk the momentum of the relative motion, $P_L(\cos\vartheta)$ the Legendre polynomials and $\chi_L(R)$ the radial wave function. By substituting Eq. 1.6 in Eq. 1.5, it is possible to find a separate partial wave Schrödinger equation for the radial wave function for each L value

$$\left[-\frac{\hbar^2}{2\mu}\left(\frac{d^2}{dR^2} - \frac{L(L+1)}{R^2}\right) + V(R) - E\right]\chi_L(R) = 0 \tag{1.7}$$

The solution χ_L of Eq. 1.7 is then substituted into Eq. 1.6 and the result is compared to the asymptotic form of Eq. 1.2. This provides an expression for the scattering amplitude

$$f(\vartheta) = \frac{1}{k}\sum_{L=0}^{+\infty}(2L+1)P_L(\cos\vartheta)e^{i\delta_L}\sin\delta_L \tag{1.8}$$

where δ_L is the *phase-shift* which is positive (negative) for attractive (repulsive) potentials.

It useful to introduce the formalism of the *S-matrix*[1]. It is related to the phase-shift by

$$\mathbf{S}_{\mathrm{L}} = e^{2i\delta_L} \tag{1.9}$$

where $\mathbf{S}_{\mathrm{L}}$ are called *partial wave S-matrix elements* or *reflection coefficients* and are complex. Using $\mathbf{S}_L$, Eq. 1.8 becomes

$$f(\vartheta) = \frac{1}{2ik}\sum_{L=0}^{+\infty}(2L+1)P_L(\cos\vartheta)(\mathbf{S}_{\mathrm{L}}-1) \tag{1.10}$$

Sometimes, instead of the S-matrix, the $\mathbf{T}_{\mathrm{L}}$ *partial wave T matrix elements* (or *transmission coefficients*) are used. They are connected to the S-matrix by

$$\mathbf{S}_{\mathrm{L}} = 1 + 2i\mathbf{T}_{\mathrm{L}} \tag{1.11}$$

In this case, Eq. 1.8 becomes

$$f(\vartheta) = \frac{1}{k}\sum_{L=0}^{+\infty}(2L+1)P_L(\cos\vartheta)\mathbf{T}_{\mathrm{L}} \tag{1.12}$$

While $\mathbf{T}_{\mathrm{L}}$ represent the outgoing waves only, $\mathbf{S}_{\mathrm{L}}$ contain the incoming waves too and they are uniquely determined by the scattering potential. If no potential is present, no outgoing waves are generated, hence $\mathbf{S}_{\mathrm{L}} = 1$ for each L (or equivalently $\mathbf{T}_{\mathrm{L}} = 0$) and the scattering amplitude $f(\vartheta) = 0$ (i.e. the cross section is zero). The same situation can be obtained when a potential is present, for large values of L. In fact, in this case, the projectile keeps apart from the target and the effect of the potential is negligible. Therefore, for $L \to \infty \Rightarrow \mathbf{S}_{\mathrm{L}} \to 1$.

Moreover, if the scattering potential is real, the outgoing flux must be conserved and therefore $|\mathbf{S}_{\mathrm{L}}| = 1$. On the contrary, if the potential has an imaginary term, part of the flux leaves the elastic channel in favour of other channels (see Sec. 1.3.3), hence $|\mathbf{S}_{\mathrm{L}}| < 1$.

1.3.3 Scattering potential

The scattering potential $V(R)$ of Eq. 1.5 is made of a Coulomb part and a nuclear part

$$V(R) = V_{\mathrm{C}}(R) + V_{\mathrm{N}}(R) \tag{1.13}$$

---

[1] The S-matrix in the pure elastic scattering contains one channel only, and the term "matrix" might be confusing. The terminology is taken from the multi-channel scattering where the S-matrix contains all the channels included in the model space (see Sec. 1.3.4)

to take into account both the Coulomb interaction and the nuclear one. The Coulomb potential is defined by

$$V_{\mathrm{C}}(R) = \begin{cases} \frac{Z_1 Z_2 e^2}{2R_{\mathrm{C}}}\left(3 - \frac{R^2}{R_{\mathrm{C}}^2}\right) & \text{if} R \leq R_{\mathrm{C}} \\ \frac{Z_1 Z_2 e^2}{2R_{\mathrm{C}}} & \text{if} R > R_{\mathrm{C}} \end{cases} \tag{1.14}$$

where Z_1 and Z_2 are the charge of the colliding nuclei and R_C is the Coulomb radius defined by

$$R_{\mathrm{C}} = R_{0\mathrm{C}}\left(A_1^{1/3} + A_2^{1/3}\right) \tag{1.15}$$

being A_1 and A_2 the masses of the nuclei involved in the reaction. The nuclear potential is usually complex and it is called *optical potential*

$$V_{\mathrm{N}}(R) = V(R) + iW(R) \tag{1.16}$$

The real part describes the elastic interaction between the two nuclei while the imaginary part takes into account those reactions channels which are not included explicitly but that remove flux from the elastic one. The nuclear potential has typically a Wood-Saxon shape

$$V_{\mathrm{N}}(R) = -\frac{V}{1 + e^{\frac{r - r_{\mathrm{V}}}{a_{\mathrm{V}}}}} - i\frac{W}{1 + e^{\frac{r - r_{\mathrm{W}}}{a_{\mathrm{W}}}}} \tag{1.17}$$

where V, r_V and a_V are the real depth, radius and diffuseness while W, r_W and a_W are the imaginary depth, radius and diffuseness, respectively. The radii are defined by

$$r_{\mathrm{V(W)}} = r_{0\mathrm{V(W)}}\left(A_1^{1/3} + A_2^{1/3}\right) \tag{1.18}$$

Sometimes, on top of the volume terms of the scattering potential, other terms are included such as surface contributions or spin-orbit interactions.

The solution of Eq. 1.7 for an interaction potential described by Eq. 1.13 provides a total scattering amplitude given by the sum of the Coulomb scattering amplitude and the nuclear scattering amplitude

$$f(\vartheta) = f_{\mathrm{C}}(\vartheta) + f_{\mathrm{N}}(\vartheta) \tag{1.19}$$

where

$$f_{\mathrm{C}}(\vartheta) = -\frac{\eta}{2k\sin^2(\vartheta/2)} e^{\left[-i\eta\ln(\sin^2(\vartheta/2)) + 2i\sigma_0(\eta)\right]} \tag{1.20}$$

and

$$f_{\mathrm{N}}(\vartheta) = \frac{1}{2ik}\sum_{L=0}^{+\infty}(2L+1)P_L(\cos\vartheta)e^{2i\sigma_{\mathrm{L}}(\eta)}(\mathbf{S}_{\mathrm{L}} - 1) \tag{1.21}$$

In the previous expressions, σ_{L} is the *Coulomb phase-shit* while η is the *Sommerfeld parameter*

$$\eta = \frac{Z_1 Z_2 e^2}{\hbar v} \tag{1.22}$$

Despite the fact that the sum in Eq. 1.21 is an infinite series, the relevant partial waves are finite. In practise, above a certain value of L, the associated impact parameter $b = L/k$ is such that the nuclear potential $\mathrm{V_N}$(b) = 0 and no outgoing scattered waves are generated.

1.3.4 Multi-channel scattering

The dynamics of the system in a scattering process in encoded in the full wave function Ψ, solution of Eq. 1.5. Nevertheless, the outgoing spherical wave contains all possible reaction channels and practical calculations require to reduce the full space to a smaller model space containing the relevant channels only. The model wave function ψ_{model} will be solution of the Schrödinger equation for an effective Hamiltonian $\mathrm{H_{eff}}$

$$(H_{\text{eff}} - E)\psi_{\text{model}} = 0 \tag{1.23}$$

Furthermore, the structure of the colliding nuclei must be taken into account in those reaction channels where internal degrees of freedom are involved, such as inelastic excitations, transfer, break-up etc. Expanding Eq. 1.23 in partial waves and considering the radial part of the scattering wave function only, the outgoing model wave function ψ_{model} can be written as the sum, for each channel α included in the model space, of the product of a structure wave function and a scattering wave function

$$\psi_{\text{model}} = \sum_{\alpha} \phi_\alpha(\xi_\alpha)\chi_\alpha(R_\alpha) \tag{1.24}$$

where ϕ_α is the structure wave function of projectile and target[2] with internal coordinates ξ_α while χ_α is the radial wave function with coordinates of the relative motion R_α. The effective Hamiltonian $\mathrm{H_{eff}}$ will have the general form

$$H_{\text{eff}} = \sum_{\alpha} H^0_\alpha(\xi_\alpha) + T_\alpha(R_\alpha) + V^{\text{eff}}_{\alpha,\alpha'}(R_\alpha, \xi_\alpha) \tag{1.25}$$

being T_α the kinetic term and $V^{\text{eff}}_{\alpha,\alpha'}$ an effective projectile-target interaction suitable to describe the dynamics of the system from the partition α to the partition α'. H^0_α is the

---

[2] It is often assumed that only one of the two nuclei has an internal structure. This means that ϕ_α is usually referred to either the projectile or the target, according to the reaction channel of interest.

internal Hamiltonian which satisfies

$$(H^0_\alpha - \varepsilon_\alpha)\phi_\alpha = 0 \tag{1.26}$$

where ε_α denotes the energy of the internal state ϕ_α. The total energy of the system will be

$$E = \sum_\alpha E_\alpha + \varepsilon_\alpha = \sum_\alpha \frac{\hbar^2 k^2_\alpha}{2\mu_\alpha} + \varepsilon_\alpha \tag{1.27}$$

The Schrödinger equation for the radial wave function contains now as many unknown scattering wave function χ_α as the number of partitions included in the model space. Projecting into the internal states ϕ_α of each α partition and integrating over all the internal coordinates ξ_α, it is possible to find a set of equations called *coupled equations*, for each partition

$$[E - \varepsilon_\alpha - T_\alpha(R_\alpha) - V_{\alpha,\alpha}(R_\alpha)]\,\chi_\alpha(R_\alpha) = \sum_{\alpha'\neq\alpha} [V_{\alpha,\alpha'}(R_\alpha)\chi_{\alpha'}(R_{\alpha'}) + \mathcal{N}_{\alpha,\alpha'}] \tag{1.28}$$

where

$$V_{\alpha,\alpha'} = \langle\phi_{\alpha'}|V^{\text{eff}}_{\alpha,\alpha'}|\phi_\alpha\rangle \tag{1.29}$$

are usually called *coupling potentials* or *radial form factors*, while the diagonal terms $V_{\alpha,\alpha}$ are the scattering potentials within the α partition. $\mathcal{N}_{\alpha,\alpha'}$ are terms that contain the non-orthogonal overlap function $\langle\phi_\alpha|\phi_{\alpha'}\rangle$ between states of different mass partitions. They are called *non-orthogonal terms* and they can be neglected in some circumstances, as it will be shown in Sec. 1.3.5 .

The solutions of Eq. 1.28 allows to determine the wave function ψ_{model}, which must satisfy the asymptotic behaviour of Eq. 1.2, and therefore the scattering amplitude $f(\vartheta)$. Also in this case, the scattering amplitude is uniquely determined by the S-matrix and it is proportional to the T-matrix $\mathbf{T}$

$$f(\vartheta) = -\frac{\mu}{2\pi\hbar^2}\mathbf{T}_{\alpha,\alpha'}(\mathbf{K}_\alpha, \mathbf{K}_{\alpha'}) \tag{1.30}$$

The cross section of multi-channel scattering is then calculated by using Eq. 1.4, summing over final m-states and averaging over the initial states.

It can be useful to write explicitly the different contributions in the outgoing model wave function, according to the different mass partitions associated to the possible relevant channels

$$\psi_{\text{model}} = \phi_\alpha(\xi_\alpha)\chi_\alpha(R_\alpha) + \sum_{\alpha'\neq\alpha}\phi_{\alpha'}(\xi_{\alpha'})\chi_{\alpha'}(R_\alpha) + \sum_\beta \phi_\beta(\xi_\beta)\chi_\beta(R_\beta) \tag{1.31}$$

In the previous expression, α denotes the initial mass partition, α' different states within the same mass partition and β a different mass partition. Eq. 1.31 shows therefore the contributions to the total outgoing model wave function by the elastic channel (first term), inelastic excitations (second term) and transfer channels (third term).

The scattering amplitude $f(\vartheta)$ can be written in a convenient integral form. Let's consider here the general case of two-channels, where the system in the initial α partition scatters in the final β partition (such as transfer). If the interaction is described by the $V_\beta(\mathbf{R}_\beta,\xi_\beta)$ scattering potential [3], the exact T-matrix can be written as

$$\mathbf{T}_{\alpha,\beta} = \int\int e^{-i\mathbf{K}_\beta\mathbf{R}_\beta}\phi^*_\beta(\xi_\beta)V_\beta(\mathbf{R}_\beta,\xi_\beta)\Psi^{(+)}_\alpha(\mathbf{R}_\alpha,\xi_\alpha)d\xi_\beta d\mathbf{R}_\beta \tag{1.32}$$

where $\Psi^{(+)}_\alpha$ is the exact wave function of the entrance channel α, made of the incoming and outgoing wave functions. Eq. 1.32 is known as the *Lippmann-Schwinger equation*.

1.3.5 DWBA approximation

A more general expression of Eq. 1.32 can be found by decomposing the interaction potential into two parts, i.e. $V_\beta = \mathcal{V}_\beta + U_\beta$. U_β can be chosen such that it describes the elastic scattering in the exit β partition, while $\mathcal{V}_\beta$ represents the interaction that causes the transition from the α to the β channels. U_β satisfies

$$[T_\beta(\mathbf{R}_\beta) + U_\beta(\mathbf{R}_\beta) + \epsilon_\beta - E]\,\chi^{(+)}_\beta(\mathbf{R}_\beta) = 0 \tag{1.33}$$

where $\chi^{(+)}_\beta$ is the elastic wave function in the channel β. Using this decomposition, Eq. 1.32 can be written as

$$\mathbf{T}_{\alpha,\beta} = \int\int \chi^{(-)}_\beta(\mathbf{R}_\beta)\phi^*_\beta(\xi_\beta)\,[\mathcal{V}_\beta - U_\beta]\,\Psi_\alpha(\mathbf{R}_\alpha,\xi_\alpha)d\xi_\beta d\mathbf{R}_\beta \tag{1.34}$$

which is know as the *Gell-Mann-Goldberg transformation* or *two potential formula*. This expression is exact but it can not be solved since it contains the exact wave function $\Psi^{(+)}_\alpha$.

When $\mathcal{V}_\beta$ is weak compared to U_β, Eq. 1.34 can be solved by approximating the exact wave function $\Psi^{(+)}_\alpha$ with

$$\Psi^{(+)}_\alpha(\mathbf{R}_\alpha,\xi_\alpha) \approx \chi^{(+)}_\alpha(\mathbf{R}_\alpha)\phi_\alpha(\xi_\alpha) \tag{1.35}$$

where $\chi^{(+)}_\alpha$ describes the elastic scattering in the α entrance channel for a potential U_α

$$[T_\alpha(\mathbf{R}_\alpha) + U_\alpha(\mathbf{R}_\alpha) + \epsilon_\alpha - E]\,\chi^{(+)}_\alpha(\mathbf{R}_\alpha) = 0 \tag{1.36}$$

---

[3] This corresponds to the *post* representation of the interaction. The difference between *prior* and *post* representation is described in Sec. 1.3.6

This approximation is called *First Order Distorted Wave Born Approximation (DWBA)* and $\chi_\alpha^{(+)}$ are called *distorted waves*. Since only two channels are involved and the coupling is performed from the α to β partition only, this approximation is often called *one-step DWBA*. In this case, the T-matrix becomes

$$\mathbf{T}_{\alpha,\beta}^{DWBA} = \int\int \chi_\beta^{(-)}(\mathbf{R}_\beta)\phi_\beta^*(\xi_\beta)\left[\mathcal{V}_\beta - U_\beta\right]\chi_\alpha^{(+)}(\mathbf{R}_\alpha)\phi_\alpha(\xi_\alpha)d\xi_\beta d\mathbf{R}_\beta \tag{1.37}$$

1.3.6 Transfer reactions

In a transfer reaction, a nucleon or a cluster is transferred from the projectile to the target or vice versa. A schematic representation of a transfer process is shown in Fig. 1.8.

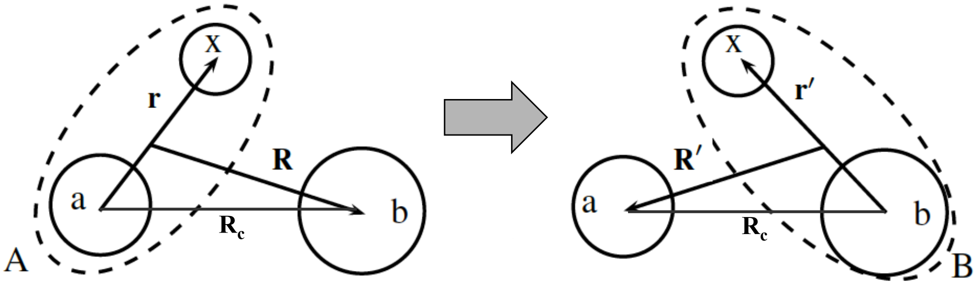

Figure 1.8: Scheme of a transfer reaction A + b = a + B, where A = (a+x) and B = (b+x).

In the picture, a projectile-nucleus **A** = (**a**+**x**) scatters on a target-nucleus **b** and the particle (cluster) **x** is transferred, giving rise to the final system **B** = (**b**+**x**). **a** and **b** are usually called *core*.

The bound states ϕ_{A} of the nucleus **A** in the initial mass partition and those ϕ_{B} of the nucleus **B** in the final mass partition are described by the internal Hamiltonians $\mathrm{H_A}$ and $\mathrm{H_B}$, respectively

$$\left[H_{\mathrm{A}} - \varepsilon_A\right]\phi_{\mathrm{A}}(\mathbf{r}) = \left[T_{\mathbf{r}} - V_{ax}(\mathbf{r}) - \varepsilon_A\right]\phi_{\mathrm{A}}(\mathbf{r}) = 0 \tag{1.38}$$

$$\left[H_{\mathrm{B}} - \varepsilon_B\right]\phi_{\mathrm{B}}(\mathbf{r}) = \left[T_{\mathbf{r}'} - V_{bx}(\mathbf{r}') - \varepsilon_B\right]\phi_{\mathrm{B}}(\mathbf{r}') = 0 \tag{1.39}$$

The total Hamiltonian describing the transfer can be expanded in the *prior* or *post* forms, according to whether the coordinates of the initial or final mass partition are chosen

$$H_{\text{prior}} = T_{\mathbf{R}} + U_{\mathrm{Ab}}(\mathbf{R}) + H_{\mathrm{A}}(\mathbf{r}) + \mathcal{V}_{\text{prior}}(\mathbf{r},\mathbf{R}) \tag{1.40}$$

$$H_{\text{post}} = T_{\mathbf{R}'} + U_{\text{aB}}(\mathbf{R}') + H_{\text{B}}(\mathbf{r}') + \mathcal{V}_{\text{post}}(\mathbf{r}', \mathbf{R}') \tag{1.41}$$

U_{Ab} and U_{aB} are the diagonal potential of the entrance and exit channels, respectively, while $\mathcal{V}_{\text{prior}}$ and $\mathcal{V}_{\text{post}}$ are the i*nteraction terms* in the *prior* and *post* representations. They can be written as

$$\mathcal{V}_{\text{prior}}(\mathbf{r}, \mathbf{R}) = V_{\text{bx}}(\mathbf{r}') + [U_{\text{ab}}(\mathbf{R}_c) - U_{\text{Ab}}(\mathbf{R})] \tag{1.42}$$

$$\mathcal{V}_{\text{post}}(\mathbf{r}', \mathbf{R}') = V_{\text{ax}}(\mathbf{r}) + [U_{\text{ab}}(\mathbf{R}_c) - U_{\text{aB}}(\mathbf{R}')] \tag{1.43}$$

V_{bx} and V_{ax} are the *binding potentials* while the terms in brackets are called *remnant terms*. Since the mass of the transferred particle (cluster) is typically small compared to those of the cores, the remant terms have usually the same magnitude and they are sometimes neglected. It is important to note that if the full remnants are considered, the *prior* and *post* representation must provide the same results.

The transition matrix element can be calculated using a first order (one-step) DWBA approximation

$$\mathbf{T}^{\text{DWBA}} =< \chi_{\text{aB}}\phi_{\text{B}}|\mathcal{V}^{\text{prior}}_{\text{post}}|\chi_{\text{Ab}}\phi_{\text{A}} > \tag{1.44}$$

In terms of coupled equations, this approximation is equivalent to

$$[E - \varepsilon_{\text{A}} - T_{\text{Ab}} - U_{\text{Ab}}]\,\chi_{\text{Ab}} = 0 \tag{1.45}$$

$$[E - \varepsilon_{\text{B}} - T_{\text{aB}} - U_{\text{aB}}]\,\chi_{\text{aB}} =< \phi_{\text{B}}|\mathcal{V}^{\text{prior}}_{\text{post}}|\phi_{\text{A}} > \chi_{\text{Ab}} \tag{1.46}$$

It is important to note that, within this approximation, the *non-orthogonal* terms mentioned in Sec. 1.3.4 never appear.

The internal wave functions ϕ_{A} and ϕ_{B} are described as *overlap functions* between the core **a** and the fragment **x** in the first case and between the core **b** and the fragment **x** in the second one. Let's consider the first case. ϕ_{A} is usually written as

$$\phi_{\text{A}}(\mathbf{r}, \sigma_{\text{a}}, \sigma_{\text{x}}) = \mathrm{C}^{\text{A}}_{\text{ax}}\frac{u(r)}{r}\left\{[Y_l(\hat{\mathbf{r}}) \otimes \chi_s(\sigma_x)]_j \otimes \chi_{I_a}(\sigma_a)\right\}_J \tag{1.47}$$

where l and s are the orbital angular momentum and the intrinsic spin of **x**, coupled to j, while I_a is the intrinsic spin of the core coupled with j to give the total angular momentum J of the nucleus **A**.

$\mathrm{C}^{\text{A}}_{\text{ax}}$ is called *spectroscopic amplitude* or *coefficient of fractional percentage*. It takes into account the fact that the radial part $u(r)$ of the wave function is meant as single-particle (cluster) wave function normalized to unity. The absolute value squared of $\mathrm{C}_{\mathrm{ax}}^{\mathrm{A}}$ is called *spectroscopic factor*

$$\mathrm{S}_{\mathrm{ax}}^{\mathrm{A}} = |\mathrm{C}_{\mathrm{ax}}^{\mathrm{A}}|^2 \tag{1.48}$$

It can be interpreted as the probability of finding the composite state J of the nucleus **A** made of a core state I_a and a particle (cluster) in the state (lsj).

1.3.7 Cluster model

In this work, the transfer of a cluster-like particle is considered. For this purpose, the nuclei involved in the reaction are treated within a cluster model, considering a core-cluster system, as shown in Fig. 1.9.

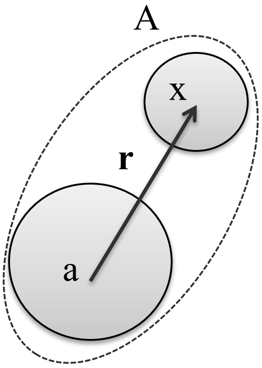

Figure 1.9: Scheme of a nucleus **A** made of a core **a** and a cluster **x**.

In the figure, the nucleus **A**, with spin and parity J^{π} is made of a core **a** and a cluster **x**. Both the core and the cluster are considered structureless. Their intrinsic properties are encoded in the ground state intrinsic spins I_a and s of **a** and **x**, respectively.
The structure wave function ϕ can be written as in Eq. 1.47. In this case, the cluster **x** will be labelled by the cluster quantum numbers N and L. N is the number of radial nodes and L is the angular momentum of the relative motion of the system (**a**+**x**)
The number of nodes N and the relative angular momentum L in the cluster-model can be determined from the shell model structure of the nucleus **A**, represented as a core **a** and as many nucleons as those forming the cluster **x**, to give the required total J^{π}. This can be done by using the Talmi-Moshinsky transformation [51]

$$2(N-1) + L = \sum_i 2(n_i - 1) + l_i \tag{1.49}$$

where i runs over the number of nucleons. n_i and l_i are the number of nodes and the orbital angular momentum of the i-th nucleon.

N is usually determined by constraining the total parity π of the state J

$$\pi = (-)^{I_a}(-)^{I_x}(-)^{L} \tag{1.50}$$

It should be noted that this model does not treat the antisymmetrization between clusters. However, the Pauli principle can be satisfied by choosing a proper core-cluster binding potential, suitable to reproduce the allowed J$^\pi$ states in the **A** system [51].

1.3.8 Transfer to the continuum

In this work, not only the cluster-transfer to bound states described by Eq. 1.49 was considered, but also the transfer to states lying in the continuum, as it will be discussed in Chapter 4. In this section, the basic ingredients needed for the description of transfer to unbound states will be illustrated [33].

In the transfer to the continuum, a particle or a cluster is transferred from a bound state of the projectile (target) to unbound states of the target (projectile)[4]. This process can be described within a three-body model, using three different set of coordinates. These are called Jacobi coordinates and they are shown in Fig. 1.10.

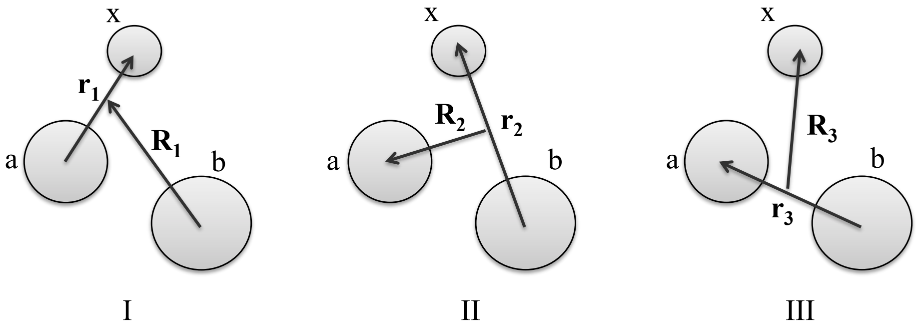

Figure 1.10: Jacobi coordinates typically used to describe a three-body process.

---

[4] This approach is similar to what it is usually done to calculate break-up cross sections, using the so-called Continuum Discretized Coupled Channel method (CDCC). In that case, the break-up is typically interpreted as an inelastic excitation of the one of the two fragments to unbound states, *within the same mass partition* [33].

The total wave function Ψ of the system is written as the sum of each Jacobi component

$$\Psi = \sum_{n=1}^{3} \Psi_n(\mathbf{r}_n, \mathbf{R}_n) \tag{1.51}$$

The three-body Hamiltonian is

$$H_{\text{tot}}^{\text{3b}} = T_n + V_{\text{ax}} + V_{\text{bx}} + V_{\text{ab}} \tag{1.52}$$

where T_n is the kinetic term for any choice of Jacobi coordinates. The Schrödinger equation is written as a set of three equations coupling the three components

$$(E - T_1 - V_{\text{ax}})\Psi_1 = V_{\text{ax}}(\Psi_2 + \Psi_3) \tag{1.53}$$

$$(E - T_2 - V_{\text{bx}})\Psi_2 = V_{\text{bx}}(\Psi_3 + \Psi_1) \tag{1.54}$$

$$(E - T_3 - V_{\text{ab}})\Psi_3 = V_{\text{ab}}(\Psi_1 + \Psi_2) \tag{1.55}$$

These equations are called *Faddeev equations* and they have a well-defined asymptotic behaviour for R$_n \to \infty$. In fact, the equations become uncoupled for large R$_n$ (i.e. the right side become zero for n $\neq$ n'), ensuring that possible bound states ϕ_n only appear in the boundary conditions for the wave function Ψ_n.

The transfer process considered in this work describes the evolution of the system I to the system II of Fig. 1.10. Since no bound states are included for the system III, the third Faddeev equation is not considered. The total wave function Ψ is expanded in terms of the internal Hamiltonians (see Sec. 1.3.4), within a model space that contains the ground state of the system (**a**+**x**) and the states in the continuum of the system (b+x). The transfer is computed by using a first-order DWBA approximation so that the non-orthogonal terms disappear.

The unbound states need a special attention. These states have the standard angular momentum decomposition of Eq. 1.47. The radial wave functions u_k are solution of the Schrödinger equation

$$\left[-\frac{\hbar^2}{2\mu_{\text{bx}}}\left(\frac{d^2}{dr_2^2} - \frac{L(L+1)}{r_2^2}\right) + V_{\text{bx}}(r_2) - \epsilon_k\right] u_k(r_2) = 0 \tag{1.56}$$

for $\epsilon_k > 0$, where **k** is the momentum of the internal motion of the system (**b**+**x**). As a consequence, u_k oscillate to infinity. In order to make the u_k scattering wave functions square-integrable, it is suitable to have a finite representation of the continuum.

This can be done by the *continuum bin* method, where the radial wave functions u_k are averaged over the continuous variable k. This method consists in dividing the continuum into discrete bins with momentum p = 0,...,N, where N is the number of bins, for each bin state with average energy $\tilde{\epsilon}_p$ near the mid-point momentum $(k_{p-1} + k_p)/2$. The new radial wave functions $\tilde{u}_p$ are therefore a superposition of scattering eigenstates

$$\tilde{u}_p(r_2) = \sqrt{\frac{2}{\pi N_p}} \int_{k_p - 1}^{k_p} g_p(k) u_k(r_2) dk \tag{1.57}$$

for a weight function $g_p(k)$. N_p is the normalization constant which is chosen to make $\tilde{u}_p$ form an orthonormal set when (k_{p-1}, k_p) are non overlapping continuum intervals

$$N_p = \int_{k_p - 1}^{k_p} |g_p(k)|^2 dk \tag{1.58}$$

For non-resonant states, the weight function $g_p(k)$ has usually the form

$$g_p(k) = e^{-i\delta_l(k)} \tag{1.59}$$

where δ_l is the phase shift of the scattering states. If the states are resonant, an extra factor is included to reproduce the resonance

$$g_p(k) = e^{-i\delta_l(k)} \sin \delta_l(k) \tag{1.60}$$

In this way, the wave function $\tilde{u}_p$ decays to zero for large distances.

1.3.9 Selectivity of transfer reactions and Q-value matching

Transfer reactions are usually strongly selective. One type of selectivity is given by the wave functions of the initial and final states involved in the transfer. In particular, the matching between the angular momenta of the levels is crucial in single-nucleon transfers. In multi-nucleon transfer reactions, such as cluster-transfers, the more are the nucleons transferred the less this selectivity persists. On the other hand, the angular momentum of the relative motion starts dominating the cross section. This indicates that in transfer reactions between heavy-ions, the kinematics conditions of the reaction play a crucial role in the description of the cross section of the process.

The strongest dependence is given by the Q-value of the reaction, which is described in App. A. It is defined as

$$Q := Q_{\text{gg}} - E^{*} \tag{1.61}$$

where Q_{gg} = - ΔM is the Q-value for the transfer when both the final products are in their ground state and E^{*} is the excitation energy of the final system. For energies around the Coulomb barrier, where the orbit description is valid, the transfer probability is the largest when the difference between the distance of closest approach in the entrance and exit channels is close to the the wavelength of the relative motion. Such a difference is the smallest when the Q-value of the reaction is equal to the so called Optimum Q-value (Q_{opt}) [9,52], which is given, for a reaction A + b = a + B, at the leading order, by

$$Q_{\text{opt}} \approx E_{\text{cm}} \left(\frac{Z_{\text{a}} Z_{\text{B}}}{Z_{\text{A}} Z_{\text{b}}} - 1 \right) \tag{1.62}$$

being E_{cm} the center-of-mass energy and Z_{a},Z_{B}, Z_{A}, Z_{b} the atomic numbers of the nuclei in the final and initial mass partitions, respectively.
Q_{opt} defines where the transfer cross section is the largest. For Q-values different from Q_{opt}, the transfer probability drops off smoothly. For the transfer of neutrons only, Q_{opt} is ≈ 0, while in the transfer of charged particles it can be either positive or negative. From Eq. 1.61 it can be seen that the maximum Q-value is obtained when the transfer leaves the final products in their ground states. If the transfer takes place to excited states, the Q-value decreases according to E^{*}. In transfer reactions characterized by $Q_{\text{gg}} > Q_{\text{opt}}$, the transfer to excited states is favoured and the cross section is the highest for $E^{*}{}_{\text{opt}}$, which is related to the Q-value by

$$E^{*}_{\text{opt}} = Q_{\text{gg}} - Q_{\text{opt}} \tag{1.63}$$

On the other hand, when $Q_{\text{gg}} < Q_{\text{opt}}$ either the transfer mainly populates the ground state or the reaction channel is hindered. These two scenarios are schematically presented in Fig. 1.11, where a typical transfer probability is plotted as a function of the Q-value. The left part shows the case in which $Q_{\text{gg}} > Q_{\text{opt}}$ and the yellow area represents the energy window available in the transfer process, peaked at $E^{*}_{\text{opt}} = Q_{\text{gg}} - Q_{\text{opt}}$. On the contrary, the right side shows the case $Q_{\text{gg}} < Q_{\text{opt}}$ and, as it can be seen, the available energy window is much reduced and the highest transfer probability corresponds to Q-value = Q_{gg}.

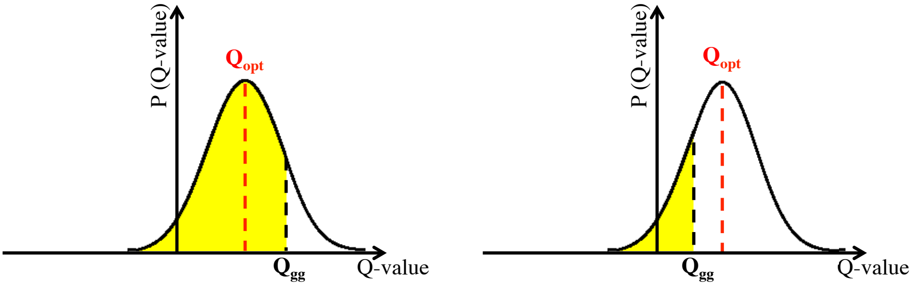

Figure 1.11: Typical transfer probability as a function of the Q-value in the case of $Q_{\rm gg} > Q_{\rm opt}$ (left side) and $Q_{\rm gg} < Q_{\rm opt}$ (right side). $Q_{\rm gg}$ is indicated by a black line while $Q_{\rm opt}$ by a red line. The yellow area represents the energy window available to the transfer process.

CHAPTER 2

The experiment

The aim of the experiment was to study the heavy-ion reaction ^{98}Rb+^{7}Li, focusing, in particular, on cluster-transfer reaction channels. The experiment was performed at ISOLDE (CERN), by using the neutron-rich radioactive ^{98}Rb beam accelerated by the REX-ISOLDE linear accelerator (linac) at 2.85 MeV/A on a LiF target 1.5 mg/cm^2 thick. The reaction channels were investigated by γ-particle coincidence techniques using the MINIBALL-T-REX setup. In this chapter the ISOLDE facility and the MINIBALL-T-REX setup will be presented, as well as the experimental details.

2.1 ISOLDE

Radioactive ion beams are produced at ISOLDE [29] by using the 1.4 GeV proton beam from the PS BOOSTER synchrotron at CERN. Pulses of $3{\cdot}10^{13}$ protons are delivered to the ISOLDE primary target every 1.2 seconds, or multiples of it, resulting in an average current of 2 μA. The primary target is, in most of the cases, UCx and radioactive nuclei are produced via fission, fragmentation and spallation proton-induced reactions. The primary target is kept at very high temperature ($\approx$ 2000 °C) in order to favour the diffusion of radioactive species and their extraction. Atoms are subsequently ionized to a 1^+ charge state by one of the three ion sources used at ISOLDE (surface, plasma and laser ionization). In the present experiment, the surface ionization source was used. The ions are then accelerated to 60 keV and mass separated according to their mass over charge ratio. At ISOLDE there exist two mass separators: the General Purpose Separator (GPS) and the High Resolution Separator (HRS). The first is characterized by a mass resolving power of 2400 while the second has a better resolution up to 7000. In this work, the HRS was used. In Fig. 2.1 a sketch of the ISOLDE facility is shown while in Fig. 2.2 the yield of radioactive nuclei produced at ISOLDE is presented.

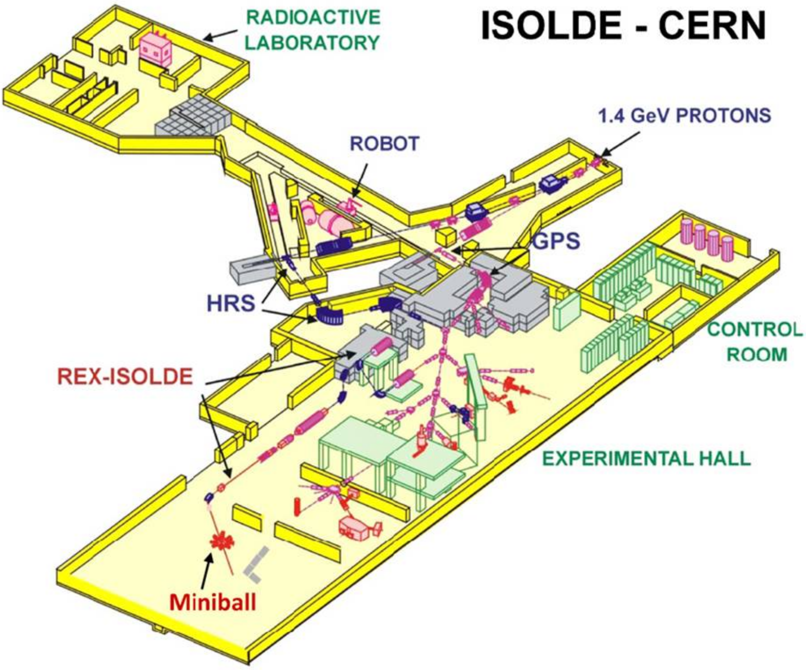

Figure 2.1: Sketch of the ISOLDE facility at CERN [53].

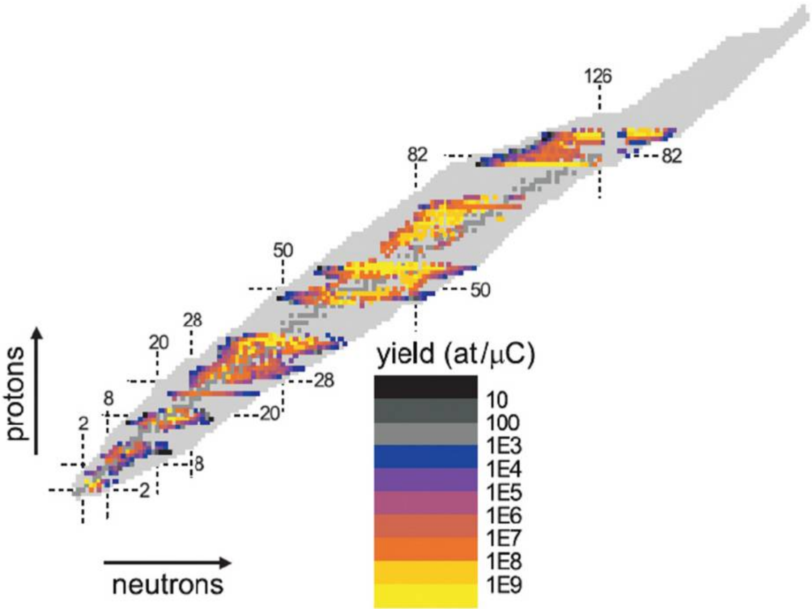

Figure 2.2: Yield of radioactive nuclei produced at ISOLDE [53].

2.2 REX-ISOLDE

After the mass separation, the 60 keV ions are accelerated at 2.85 MeV/A by the REX-ISOLDE post-accelerator [53]. It is a room temperature linac which consists of a RFQ (Radio Frequency Quadrupole), an interdigital H-type (IH) structure, three 7-gap resonators, and one 9-gap resonator. In order to increase the efficiency of injection into the linac, the ions are firstly collected, cooled and bunched in a Penning Trap, called REX-TRAP, with a potential of nearly 60 kV. Ion bunches are then extracted and delivered to an Electron Beam Ion Source (EBIS) where they are further ionized to the required mass-to-charge ratio (A/Q)<4.5. The time for the charge breeding depends on the isotope of interest and can vary from 20 ms to 200 ms for the heaviest elements. The ions are finally extracted from the EBIS and injected into the linac in pulses, with a typical time width of 300 μs. In this experiment, 3 EBIS pulses were accelerated towards the MINIBALL experimental area. In Fig. 2.3 a sketch of the REX-ISOLDE accelerator is presented.

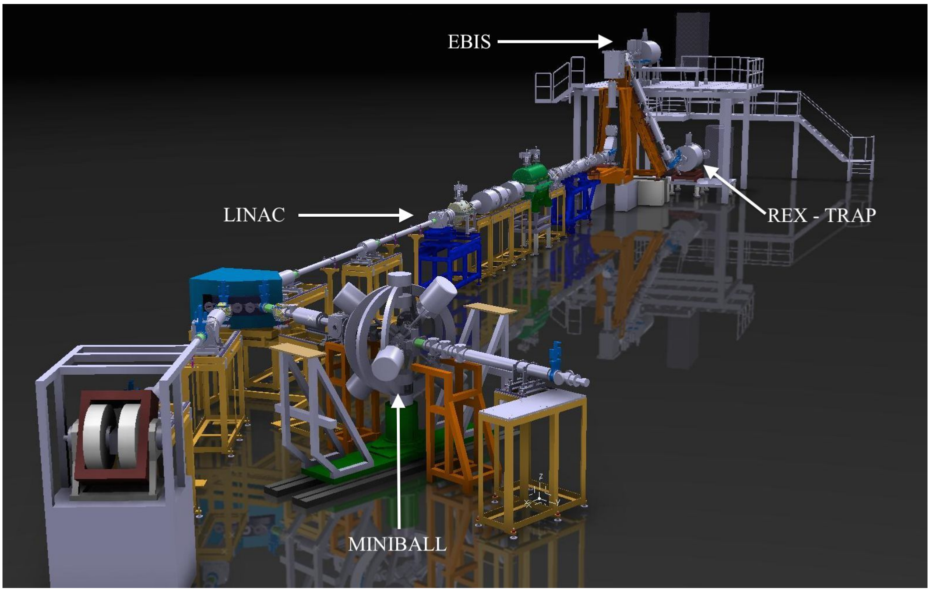

Figure 2.3: Sketch of the REX-ISOLDE linac accelerator [54].

2.3 Beam structure and composition

The time structure of the beam produced at ISOLDE and accelerated by REX-ISOLDE is determined by two aspects. The first one is the release time from the primary target, which is related to the frequency of the proton pulses. A slow release time requires proton pulses with a lower frequency, in order to accommodate the production and the extraction of the radioactive species. The second time information comes from the REX-EBIS. Usually, the ions are extracted from the Electron Beam Ion Source in pulses with a total width of approximately 300 μs and a frequency that depends on the time needed for ionization (e.g. 100 ms). The timing of the EBIS is used as a trigger to record the data. Each EBIS cycle opens a so called ON-beam window of about 800 μs and during that time data are registered. This time window is followed by the read-out of the data, which may take few milliseconds, and an OFF-beam window. During this time, the background radiation is detected. The general time structure of the beam is presented in Fig. 2.4 [30].

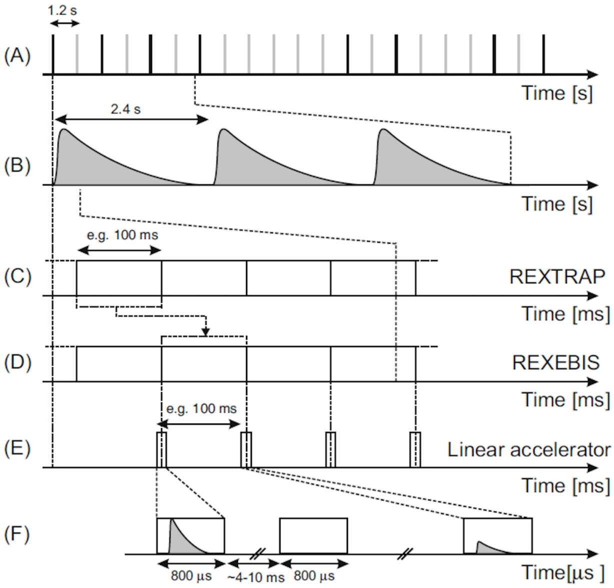

Figure 2.4: (A) The proton bunches distributed to the different experiments at CERN. As an example, the black ones correspond to those provided at ISOLDE. (B) Typical release profiles of isotopes produced in the primary target. (C-D) REX-TRAP and REX-EBIS bunches. (E) Timing of the EBIS used as a trigger for ON-beam, read-out and OFF-beam windows of the MINIBALL setup (F) [30].

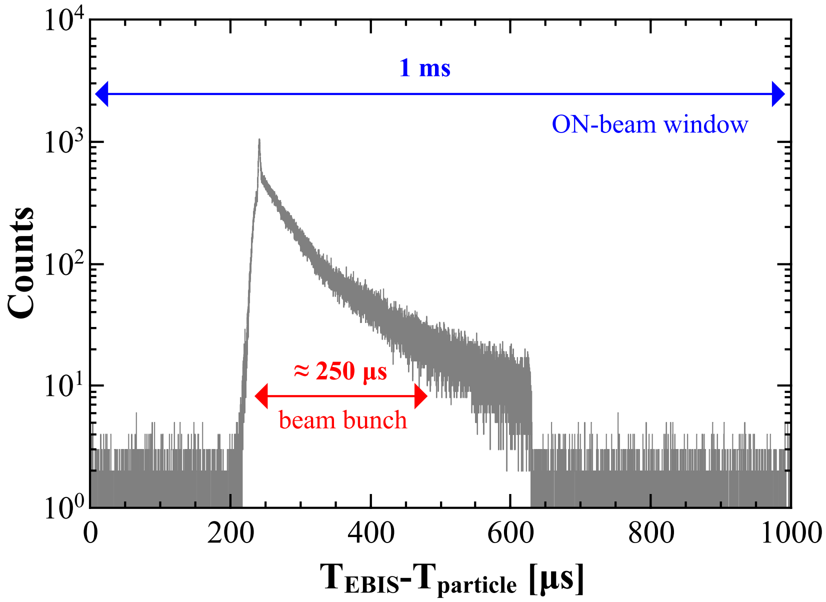

Figure 2.5: Time difference between the EBIS signal and detected particles , as measured in this experiment, showing the average beam time window width of ≈ 250 μs. The full scale of the spectrum corresponds instead to the ON-beam window, during which the data are registered.

In Fig. 2.5 the time structure in the case of the present experiment is shown. The ON-beam window corresponds to ≈ 1 ms and the total beam bunch around 250 μs. The latter is plotted by taking the time difference between the EBIS signal and the detected particles.

Due to the production mechanism, in some cases contaminants are present in the ISOLDE beam. The main sources of contamination come from isobars not well separated, as well as from the in-trap β decay of short-living isotopes. Usually, the beam composition is controlled through a Bragg chamber placed at the end of the acceleration line. Unfortunately, in this experiment, the chamber couldn't be used because of electronic problems. Since a strong component of the isobaric ^{98}Sr was observed together with the required ^{98}Rb beam, the EBIS time was reduced to 73 ms and only the first three pulses were taken in order to reduce the percentage of ^{98}Sr as β daughter of ^{98}Rb. The aim was to limit the in-trap β decay of both the ground state and the first isomer state (both produced at ISOLDE) which have half-lives of ≈ 140 ms. An average value of ≈ 2/3 was estimated for the ^{98}Rb/^{98}Sr beam composition. Such a value was obtained by comparing the counts in the γ-ray spectra associated to α- and t-transfer on both beam components, as it will be explained in Sec. 4.6.2.

The so found ratio points out that, despite the attempt to reduce ^{98}Rb in-trap β decay, most of ^{98}Sr nuclei came directly from the primary target, showing the limitations imposed by the mass separation between ^{98}Rb and ^{98}Sr.
The β-decay of ^{98}Rb populates different levels in the daughter ^{98}Sr nucleus, depending on whether the decay occurs from the ground state or from the isomer [55]. As a result, it gives rise to a different γ-decay path with characteristic γ-rays for each decay, as shown in Fig. 2.6 for two typical γ transitions.

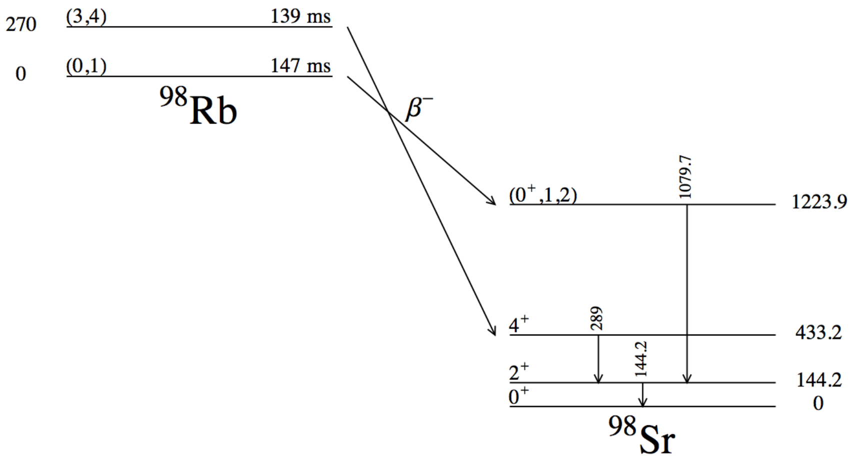

Figure 2.6: β decay of ^{98}Rb to ^{98}Sr showing characteristic γ-rays of the decay from the ground state and from the isomer state [55].

It may be possible, in principle, to determine the ratio between the ground state and the isomer, by looking at the relative percentage of the above mentioned γ-rays. Nevertheless, in this experiment it was not possible to extract a precise value for different reasons. First of all, the measured β decay spectrum comes from decay of ^{98}Rb randomly implanted in and around the scattering chamber. As a consequence, it was not possible to correct the detected γ-rays for the detection efficiency, being the implantation position unknown. Secondly, the tabulated decay branching ratios are provided under certain assumptions for the spins of the levels, although precise values are not measured [21]. However, it is clear that both the ground state and the isomer were delivered to the experimental area. This can be deduced by the total γ spectrum which shows γ-lines characteristic of each decay, according to what is reported in literature [55]. In particular, the 1223.9 keV → 144.2 keV decay, corresponding to a γ-transition of 1079.7 keV, is associated to the ground state decay only, while the 433.2 keV → 144.2 keV decay, corresponding to a γ-transition of 289 keV, is typical of the isomer decay. The spectra measured in this experiment are presented in Fig. 2.7 and Fig. 2.8.

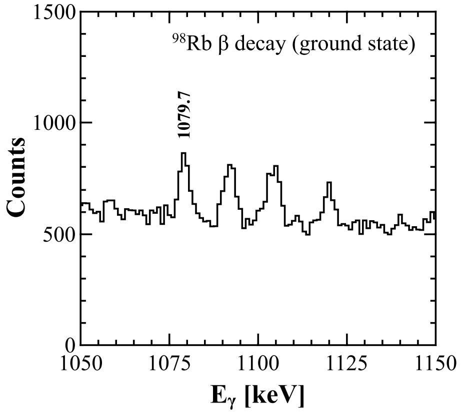

Figure 2.7: Total γ-ray spectrum, showing the region with a characteristic γ-line (1079.7 keV) of ^{98}Rb β-decay from the ground state. In particular, it corresponds to the 1223.9 keV → 144.2 keV decay.

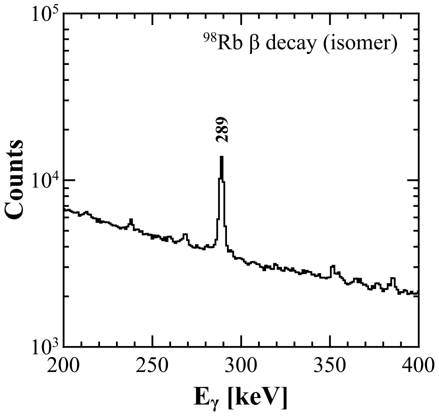

Figure 2.8: Total γ-ray spectrum, showing the region with a characteristic γ-line (289 keV) of ^{98}Rb β-decay from the isomer. In particular, it corresponds to the 433.2 keV → 144.2 keV decay.

Despite the rather high intensity of ^{98}Rb produced in the primary target ($\approx 3{\cdot}10^6$ Ions/μC) [54], an average beam intensity of $2{\cdot}10^4$ pps was delivered on the MINIBALL target, as a consequence of the transmission in REX-ISOLDE. Such a value was obtained by analysing the elastic scattering reaction channel, as it will be described in Sec. 4.1.2.

The nominal energy of the ^{98}Rb beam required for this experiment was 2.85 MeV/A, the maximum energy available at REX-ISOLDE at that time. Nevertheless, the thickness of the target played an important role, since a huge loss of energy in the whole target, of almost 70 MeV, was observed.

2.4 The MINIBALL detector

The MINIBALL γ-spectrometer is a high resolution HPGe array which consists of height clusters of three crystals each (70 x 78 mm), placed symmetrically around the scattering chamber [30]. In this experiment, only seven clusters were used.

Each crystal is divided into six segments, obtained by electronic segmentation. Together with the signals of the segments, a common signal from the central electrode (core) is also taken. The core registers the total energy deposited in the crystal and provides the time signal, while the segments collect the partial energy released and supply the angle of detection. The total working segments during this experiments were 113.

The use of composite segmented detectors, such as MINIBALL, allows to improve the Doppler Correction of γ-rays, providing more precise angles, and to reduce the Doppler broadening. Furthermore, such a segmentation allows to increase the efficiency of the array by means of the *addback* procedure, which consists in summing up the energies deposited in adjacent crystals when Compton scattering occurs (Compton scattering is dominant for γ-rays above 1 MeV). In the present experiment, γ-rays up to 600 keV were associated to the reaction channels of interest therefore the Compton scattering was considered negligible. As a consequence, no *addback* was performed in this analysis. A detailed characterization of the MINIBALL array in terms of energy resolution and detection efficiency will be given in Chap. 3. In this experiment, an efficiency of ≈ 3 % at 1 MeV and a resolution at rest of ≈ 0.3 % at 1 MeV were measured.

2.5 The CD silicon detector

Charged particles were detected by the CD silicon detector belonging to the T-REX setup [31, 32]. The full T-REX configuration consists of two double-sided segmented annular silicon strip detectors (CD's) [56], placed forward and backward with respect to the target, and eight position-sensitive silicon strip detectors (barrel) placed around the target, four forward and four backward. Each detector comprises two layers (ΔE and E_{rest} detectors) and thus it is used as a E-ΔE telescope for particles identification, achieved by their specific energy loss. In this experiment, a special configuration was used, exploiting only the forward CD detector (FCD) placed at 22 mm from the target.

The ΔE part of the CD detectors (shown in Fig. 2.9) are DSSSD's (Double Sided Silicon Strip Detectors) 140 μm thick, with annular segmentation (rings) at the front and radial segmentation (strips) at the back, divided, into four quadrants. Such a segmentation provides position information, allowing the reconstruction of both polar ϑ (rings) and azimuthal φ (strips) scattering angles. The front surface is segmented into 16 rings at 2 mm intervals. Each ring is 1.9 mm wide and the separation between rings is 0.1 mm. The rear part is, instead, segmented in 24 strips in the radial direction. The whole detector is covered by an aluminium dead layer of approximately 0.7 μm. The E_{rest} detector is instead 1500 μm thick and divided into four, non-segmented, quadrants. The whole CD detector is placed into the scattering chamber and it is surrounded by the MINIBALL spectrometer. A schematic representation can be seen in Fig. 2.10 and in Fig. 2.11 .

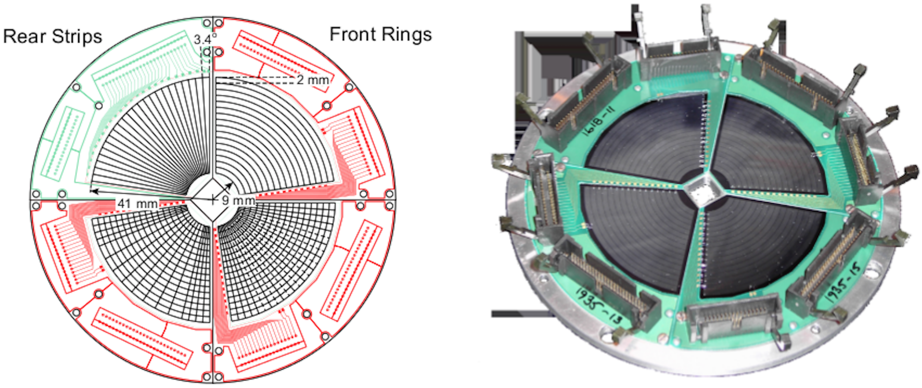

Figure 2.9: Forward CD detector.

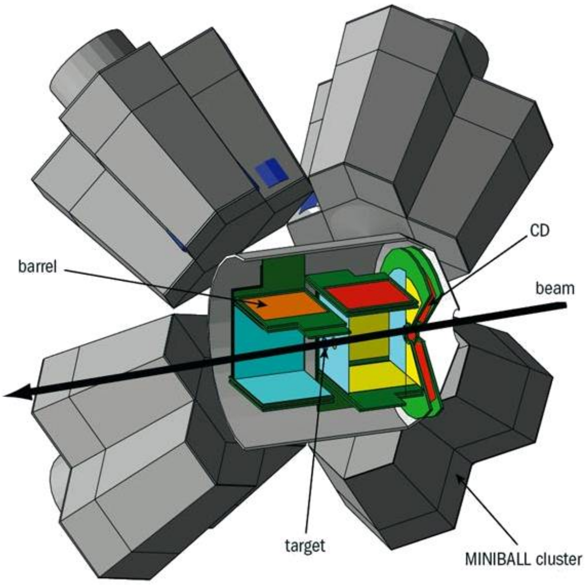

Figure 2.10: Schematic representation of the MINIBALL array coupled to the T-REX setup [57]. In this experiment, only the forward CD detector was used at 22 mm from the target position.

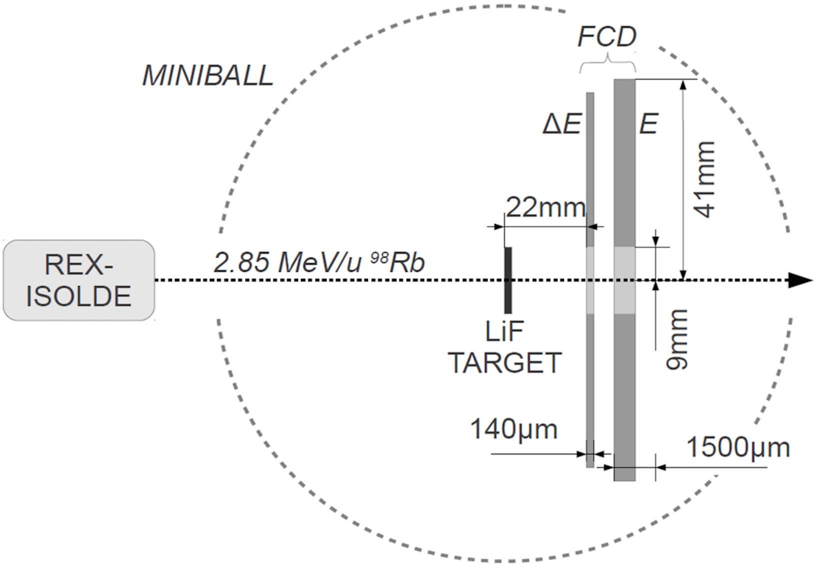

Figure 2.11: Schematic representation, not in scale, of the forward CD detector coupled to the MINIBALL array [58].

2.6 Electronics and data acquisition

MINIBALL and the CD detector are coupled together allowing γ-particle coincidence measurements. While MINIBALL uses digital electronics, the CD detector uses analog electronics.

The signals coming from the MINIBALL pre-amplifiers (168 channels considering the core and the segments of each crystal) are sent to DGF-4C modules, Digital Gamma Finder with 4 channels [59]. Two modules are used for each crystal and one channel is not used. The signal of the core is used as a trigger for the other channels. This is done to ensure the presence of the core signal for each event. Each module has an internal 40 MHz clock, even though an external clock with the same frequency, which corresponds to time stamps of 25 ns, is used to synchronize the signals.

The signals coming from the CD detector are organized into two independent triggers, by an OR of the rings of two adjacent quadrants. A scheme of the CD electronics is shown in Fig. 2.12. The 128 channels from the ΔE detector are encoded into fewer channels by using a multiplexer. In the present setup, the signals are sent to MUX-32 Mesytec modules [60]. These modules have 32 input channels and only 5 output channels. Two channels carry the energy information of two hits in different rings/strips, two carry their position information and one is a global trigger. Rings and strips of the same quadrant are sent to different multiplexers, so that two hits in the same quadrant can be recorded. The time signals are synchronised with the MINIBALL signals using the same external 40 MHz clock. The E_{rest} detector, instead, is connected to a MSI-8 module. The output signals from MUX-32 Mesytec modules and the MSI-8 module are sent to MADC (ADCs) modules.

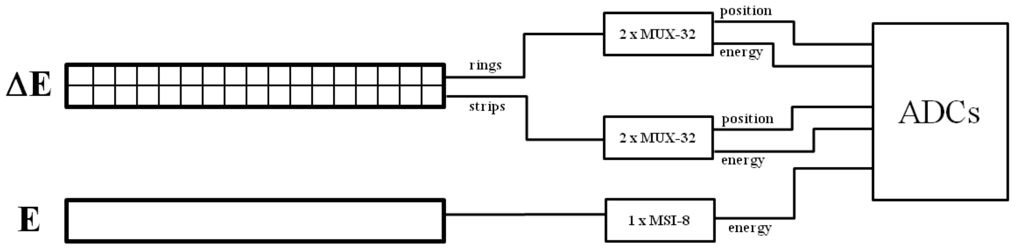

Figure 2.12: Schematic representation of the analog electronics used for the CD Silicon detector.

A scheme of the processed signals is presented in Fig. 2.13. For each event, the figure shows the possible information that can be extracted both from the MINIBALL array and the forward CD detector.

2.7 The LiF target

The target used in this experiment was a compound of LiF (^{7}Li+^{19}F) 1.5 mg/cm^2 thick. The reason of using a molecule is related to the technical difficulties in using a pure ^{7}Li target due to the rapid oxidation in contact with air. The target was provided by the target laboratory of Argonne National Laboratory. The weight ratio between ^{7}Li and ^{19}F is approximately 27 % and 73 % , respectively, as follows from mass weights.
As said before, the thickness of the target caused a notable beam energy spread due to the energy loss of ^{98}Rb in the target. Such an effect reduced the beam energy from 279 MeV to 209 MeV across the whole target. Nevertheless, the thickness of the target was chosen in order to increase the reaction yield, due to the low beam intensity and the relatively low cross sections of the reaction channels of interest, further reduced by the efficiency of the MINIBALL array. The final assumption of mid-target approximation was made and a beam energy of 244 MeV was considered in this analysis.

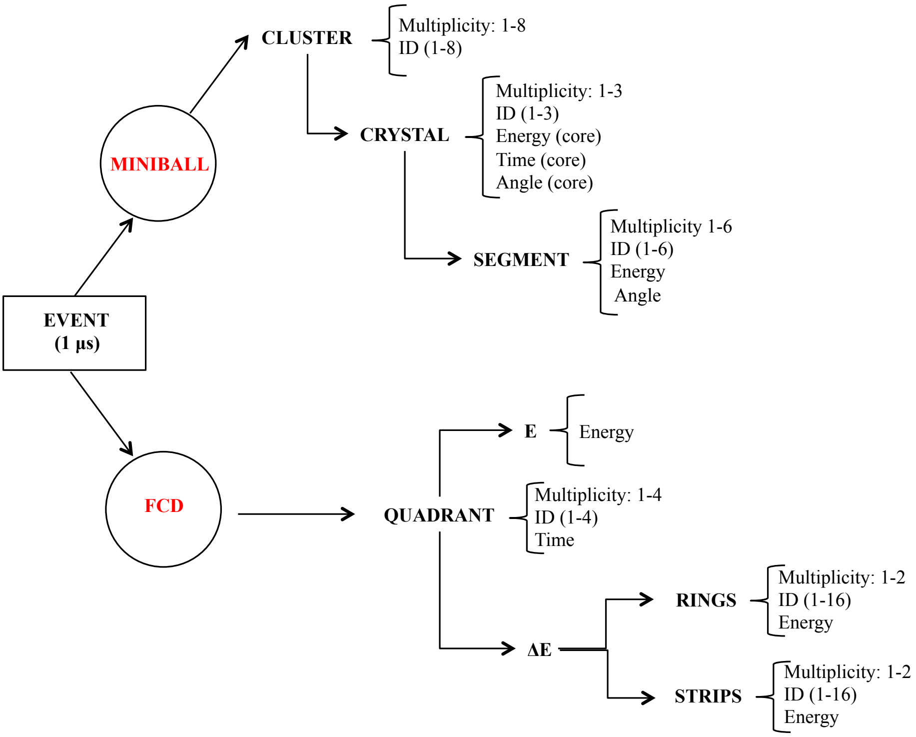

Figure 2.13: Scheme of the information that can be extracted for each recorded event for MINIBALL - FCD setup.

2.8 Duration of the experiment and counting rates

The experiment lasted about 80 h (effective beam time on target) and in the most interesting channel studied in this work, i.e. triton-transfer, an average counting rate of 10^{-2} α-γ coincidences per second was measured.

CHAPTER 3

Data Analysis

To record the data of the MINIBALL-T-REX setup, the MARABOU data acquisition software [61,62] was used. The raw data were unpacked and converted into ROOT [63] files, by building the events creating sub-files within a coincidence time window of 1 μs.

The first step of the data analysis consisted in the calibration of both the MINIBALL array and the CD silicon detector. For the Ge array, energy calibrations were performed for each segment and for the core signals. Furthermore, the angle of each segment was determined. In the case of the CD silicon detector, on top of the energy calibration for each ring and each quadrant, position calibration was done to obtain the angles of each ring.

Afterwards, the MINIBALL-T-REX data were analysed separately.

For MINIBALL data, efficiency and energy resolution were studied and Doppler correction was performed. The γ-ray spectra were investigated, both in singles and requiring coincidences within $\approx$ 200 ns, comparing ON-beam and OFF-beam spectra as well as Doppler-corrected and Doppler-shifted events.

In the case of the CD detector, particle spectra were studied and detected particles were identified according to their loss of energy. The two-body kinematics was reconstructed according to angle and energy information of the detected particles.

Finally, coincidences between γ-rays and particles were investigated, by looking at coincidences within $\approx$ 200 ns.

In this chapter a detailed description of the data analysis will be given. Part of the work presented in this section and related to the CD detector belongs to the master thesis by J. Bouma [58].

3.1 The CD detector

The CD detector must be calibrated in terms of position and energy. The ΔE layer of the CD detector is divided into 4 quadrants and 16 rings and 16 strips for each sector. For each ring and strip, position and energy calibration were performed. The E detector, instead, is not segmented and a general energy calibration for the 4 quadrants was done.

3.1.1 Position calibration

As said in Sec. 2.6, the signals from the FCD detector are multiplexed and each multiplexer provides two signals for the position, two for the energy and one global trigger. Adjacent quadrants are connected to the same multiplexer which is different for rings and strips. The position signals are linearly dependent on the ring (or strip) number, as shown in Fig. 3.1, where each peak corresponds, in this example, to a different ring of a given quadrant. A linear calibration was applied to define 16 windows to allocate each hit to a specific ring. The same procedure was performed for all the quadrants of both rings and strips.

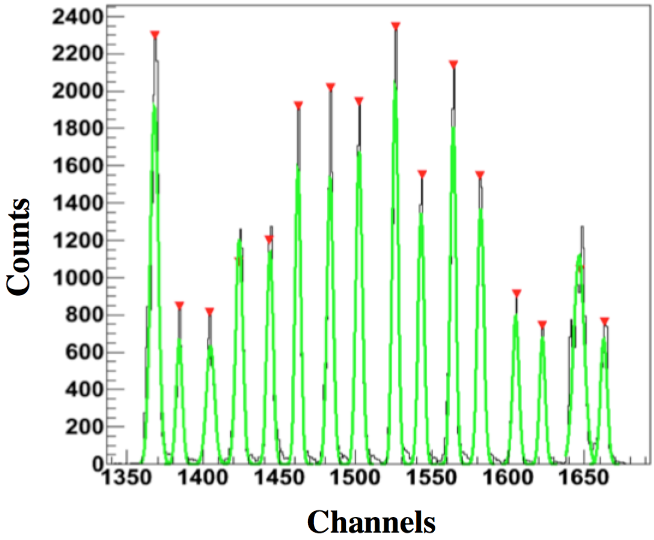

Figure 3.1: Example of position spectra used for demultiplexing the signals. In this case, each peak corresponds to a different ring of one quadrant only [58]. In fact, the figure shows 16 peaks only and it is half of the total spectrum (which would show 32 peaks, as the number of channels of each multiplexer, corresponding to the 32 signals of two adjacent quadrants.)

Because of electronics problems, the strip signals were not correctly recorded and they were not further used in the analysis. However, this was not crucial for the analysis since the information of the azimuthal angle φ (provided by the strips) was not needed, due to the symmetry of the scattering problem.

3.1.2 Energy calibration

Both the ΔE and the E_{rest} detector were calibrated in energy. To do this, a mixed calibration source emitting α particles of known energy, between 3 MeV and 6 MeV, was used. The ΔE detector was calibrated by putting the source in front of it, and by calibrating each ring and each strip. In the case of the E_{rest} detector the source was placed at the rear of the ΔE detector. The calibration obtained was extrapolated up to 30 MeV, the full-scale range of the CD detector used in this experiment. For both the ΔE and E_{rest} detector, a linear calibration was used. As an example, Fig. 3.2 and 3.3 show the α energy spectrum as measured in one quadrant of the E_{rest} detector and the linear fit used to extract the energy calibration.

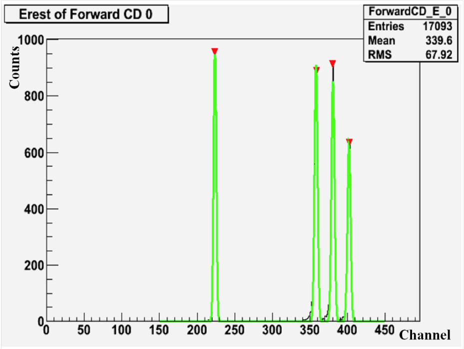

Figure 3.2: α energy spectrum as measured in one quadrant of the E_{rest} detector

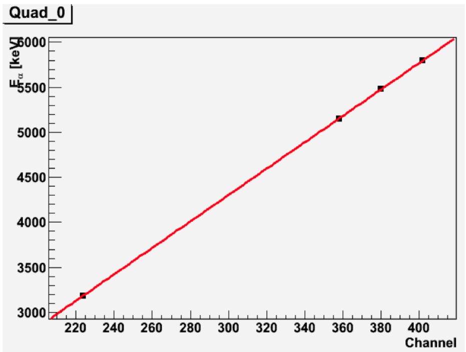

Figure 3.3: Linear fit used to extract the energy calibration.

3.1.3 Efficiency

The efficiency of the CD detector was simulated by using GEANT4 [64]. The simulation was made considering the real geometry of the detector, assuming a distance from the target of 22 mm, as well as the beam width, the target thickness and the dead spots in the detector itself. A flat distribution of events was generated and the ratio with the number of particles detected allowed to determine the efficiency distribution as a function of the scattering angle ϑ. The result can be seen in Fig. 3.4.

The efficiency is almost constant along the angular range. Hence, a common efficiency for each ring can be extracted from the flat region of the distribution

$$\varepsilon = 0.86(1) \tag{3.1}$$

The efficiency of detection deviates from 100 $\%$ due to the dead regions of the detectors between the quadrants. The efficiency was also calculated analytically assuming a Gaussian beam profile [58]. The intensity of the particle scattered through an angle ϑ was then calculated by integrating the beam profile within the limits of each ring. This "theoretical" efficiency is very similar to the simulated one, besides the absolute value that in the former case was forced to 1. The ratio between the two distributions provides the geometrical scaling factor to the efficiency of detection.

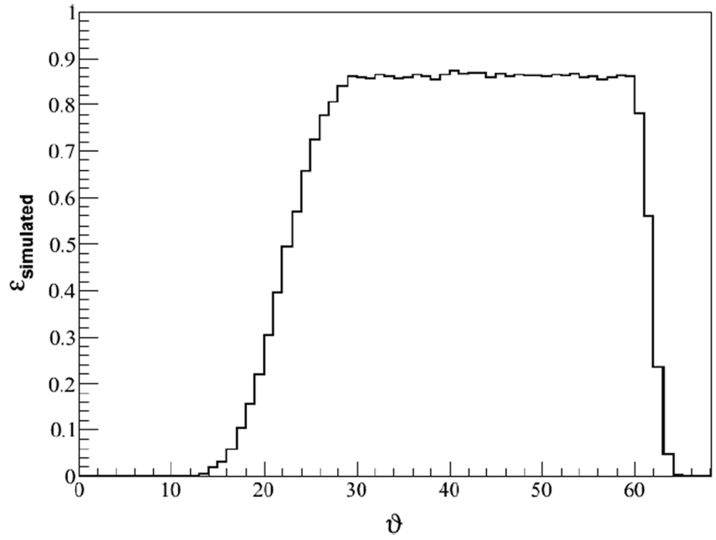

Figure 3.4: GEANT4 simulation of the detection efficiency as a function of the scattering angle for the CD detector, at 22 mm from the target [58].

3.1.4 CD angles

Each quadrant of the CD detector has 16 rings. Due to the azimuthal symmetry of the arrangement, the rings of the quadrant can be considered as one. The polar angle ϑ of each ring was defined experimentally from a point in the middle of the target to the middle of the ring itself. It should be noted that, since each ring has a finite size and the precise interaction point within a ring can not be determined, al the detected events in the same ring are associated to the same mean angle.

The solid angles covered by the rings are different and can be determined from the expression

$$\Delta\Omega = \int_{\vartheta_{min}}^{\vartheta_{max}} \int_{0}^{2\pi} \sin\vartheta d\vartheta d\varphi = 2\pi(\cos\vartheta_{min} - \cos\vartheta_{max}) \tag{3.2}$$

In Tab. 3.1 the details for each ring are reported.

Ring #	ϑ_{min} **[deg]**	ϑ_{max} **[deg]**	$\Delta\vartheta$ **[deg]**	$\bar{\vartheta}$ **[deg]**	$\Delta\Omega$**[sr]**
0	22.2	26.6	4.32	24.4	0.196
1	26.6	30.6	4.01	28.6	0.210
2	30.6	34.3	3.71	32.4	0.218
3	34.3	37.7	3.41	36.0	0.220
4	37.7	40.8	3.12	39.3	0.217
5	40.8	43.7	2.85	42.2	0.210
6	43.7	46.3	2.61	45.0	0.202
7	46.3	48.7	2.38	47.5	0.192
8	48.7	50.8	2.17	49.7	0.182
9	50.8	52.8	1.99	51.8	0.171
10	52.8	54.6	1.82	53.7	0.161
11	54.6	56.3	1.67	55.5	0.151
12	56.3	57.8	1.54	57.1	0.142
13	57.8	59.3	1.42	58.6	0.133
14	59.3	60.6	1.31	59.9	0.124
15	60.6	61.8	1.21	61.2	0.116

Table 3.1: Angles of the CD detector for each ring (see text for details). ϑ_{min} and ϑ_{max} correspond to the borders of the ring, $\Delta\vartheta$ is the angular spread, $\bar{\vartheta}$ is the mean value (center of the ring) and $\Delta\Omega$ is the solid angle covered.

The total solid angle covered by the CD detector is therefore

$$\Delta\Omega = 2.85 \quad \text{sr} \tag{3.3}$$

which corresponds to 22.6 $\%$ of the the full 4π solid angle.

3.1.5 Particle identification

The CD detector was used as a ΔE-E telescope for charged particle detection and identification. The loss of energy of charged particles in the matter follows the analytic expression given by the Bethe-Block formula [65]

$$-\frac{dE}{dx} = Z^2 \left(\frac{e^2}{4\pi\epsilon_0}\right) \frac{4\pi z N_A \rho}{m_e c^2 \beta^2 A} \left[\ln\left(\frac{2mc^2\beta^2}{I}\right) - \ln(1-\beta^2) - \beta^2\right] \tag{3.4}$$

where Z is the atomic number of the particle while z, A and ρ are the atomic number, the mass number and the density of the medium. β is the v/c ratio, N_A is the Avogadro number and m_e is the mass of the electron.
For non relativistic particles ($v/c \ll 1$), the previous expression assumes a simpler form with a dominant dependence given by

$$\frac{dE}{dx} \propto \frac{Z^2 M}{E} \tag{3.5}$$

Therefore, by correlating the loss of energy in the ΔE detector and the total energy E of the particle (measured as the sum of the loss of energy in the ΔE and E_{rest} detector), it is possible to identify the nature of the particle. The spectrum measured by the CD detector is shown in Fig. 3.5 and corresponds to the sum of all rings.
All the particles that punch through the ΔE detector (and deposit their remaining energy in the E_{rest} detector), create hyperbolic traces in the spectrum. The energy loss of the particles depends of course on the thickness of the ΔE detector. It may happen that some particles are not energetic enough to punch through the first layer and they deposit all their energy in the ΔE detector. Especially particles with a high atomic number are more easily stopped in the ΔE detector. These events appear on the diagonal in the spectrum of Fig. 3.5.
The spectrum of Fig. 3.5 allows to determine which charged particles were produced following the reaction ^{98}Rb+^{7}Li. ^{7}Li corresponds to the elastic and inelastic scattering, ^{6}He comes from the transfer of one proton, α particles and tritons are mainly associated to t- and α -transfer.

Deutrons come from the breakup of ^{6}Li, produced from the transfer of one neutron, while protons are contaminants of the target. Elastically scattered ^{19}F, also present in the target, is instead out of range. A detailed description of the reaction channels will be given in Chap. 4.

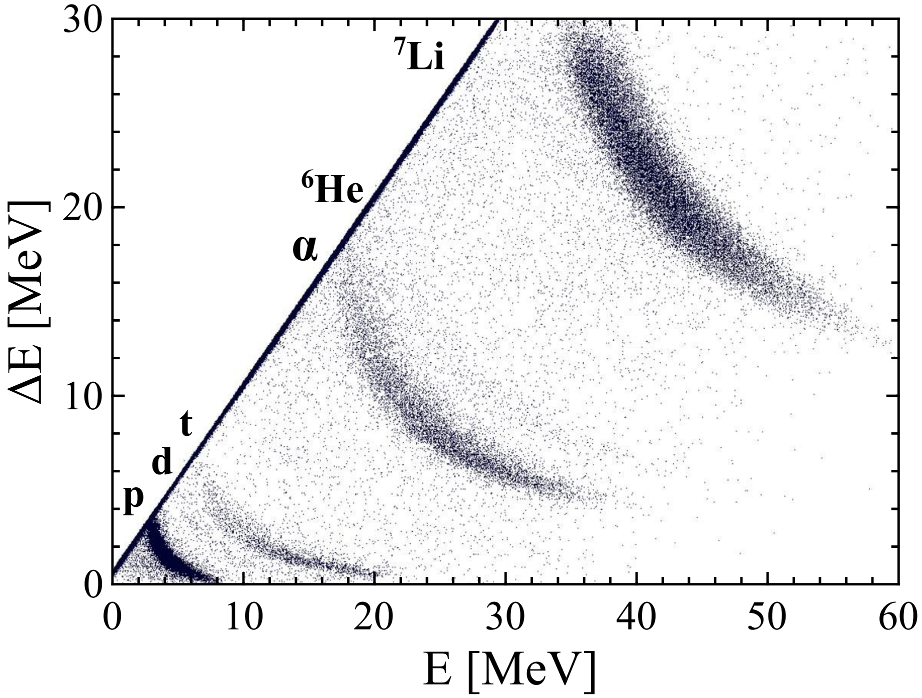

Figure 3.5: ΔE - E spectrum measured in the CD silicon detector which allows to identify emitted charged particles: ^{7}Li from elastic and inelastic scattering, ^{6}He from one-proton pick-up, α particles from triton-transfer and ^{7}Li and ^{6}Li break-up, tritons from α-transfer and ^{7}Li break-up, deuterons from ^{6}Li break-up and protons from the elastic scattering of target contaminates. The diagonal corresponds to those particles which didn't punch through the ΔE detector and therefore can not be identified, such as ^{19}F nuclei elastically and inelastically scattered.

3.1.6 Particles kinematics

The charged particles produced in the ^{98}Rb+^{7}Li reaction are primarily produced in binary processes. This means that the energy E of the emitted particles has a well-know analytic dependence on the scattering angle ϑ. A detailed description of the non relativistic two body kinematics can be found in App. A.
The expected kinematic lines can be calculated and compared to the experimental data. The results are shown in Fig. 3.6.

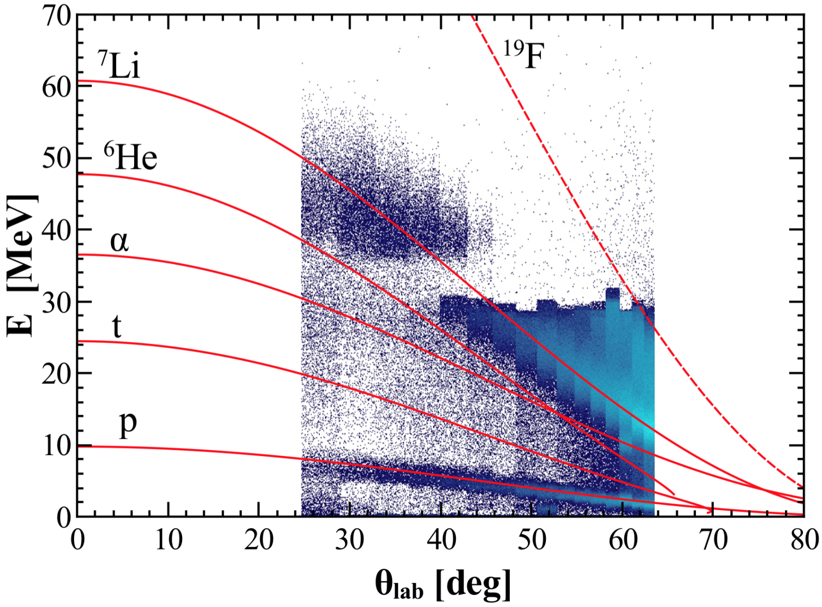

Figure 3.6: Kinematic lines for the detected particle. In the case of ^{7}Li and protons, elastic calculations were performed. ^{6}He events correspond to the one proton transfer channel for expected excitation energy of the projectile-like nuclei of 10 MeV. For α particles and tritons an excitation energy of 17 MeV and 18 MeV was considered, respectively. The predicted elastic scattering of ^{19}F, not identified, is also shown.

The thickness of the target introduces uncertainties in the experimental data, mainly due to the ^{98}Rb beam energy loss of the order of 70 MeV in the full target. This implies that there is not a unique and well defined energy at which the reactions take place. To calculate the kinematic lines, it was assumed that reactions occurred in the middle of the target and a beam energy of 244 MeV was considered. However, the quality of the data is affected by the energy spread in the target. Such an aspect cannot be corrected since it is not possible to determine precisely the interaction point within the target.

While ^{7}Li and protons correspond to elastic scattering data (with no excitation energy involved), in the case of the other particles an average excitation energy of the binary partner was assumed, in order to match the experimental data. In particular, the plotted kinematic lines correspond to projectiles-like excitation energies of 10 MeV, 17 MeV and 18 MeV for ^{6}He, α particles and tritons, respectively.
The elastic kinematic lines of ^{7}Li and protons were also used to determine experimentally the distance of the CD detector from the target, since its position was not measured. The final distance was chosen in order to fit, as best as possible, the elastic experimental data and a value of 22 mm was found.

3.2 MINIBALL array

The MINIBALL Ge array was calibrated in terms of energy and positions of the crystals. The angles of the 113 working segments were also determined.

3.2.1 Energy Calibration

The energy calibration was performed by using a ^{152}Eu γ-source which provides γ-rays up to 1.4 MeV. A linear calibration was assumed and extrapolated to 4 MeV. Although the extrapolation is not a safe procedure, all the γ lines studied in this work correspond to the de-excitation of low-lying states with energies up to 1 MeV, where the linear calibration is well under control.

3.2.2 Energy resolution and efficiency

The MINIBALL array was characterized by studying its energy resolution and efficiency. Concerning the energy resolution, only the ^{152}Eu source was used and the FWHM of the peaks was studied as a function of the energy. The energy resolution, defined by $R(E_\gamma) = \text{FWHM}/E_\gamma$ [65], was determined using the relation

$$R(E_\gamma) = A + \frac{B}{E_\gamma} \tag{3.6}$$

where E_γ is in keV. The fit of the experimental points gives as a result A = $8.37 \cdot 10^{-4}$(2) and B = 1.91(4). The data and the fit are shown in Fig. 3.7. These results refer to γ-rays emitted at rest and provide an intrinsic energy resolution of $\approx$0.3 $\%$ at 1 MeV. On the other hand, the γ-rays produced in the reactions studied in this work are emitted in flight. Hence, the FWHM of the peaks is systematically larger due to the Doppler broadening effect.

This is caused by the uncertainty in the determination of the detector angle used for Doppler correction. In particular, the uncertainty on the width of the peaks due to this effect is given by [65]

$$\Delta\text{FWHM} = 2E_\gamma\beta\sin(\Delta\vartheta)\sin\vartheta \tag{3.7}$$

where E_γ is the real energy of the γ-ray, β=v/c and $\Delta\vartheta$ is the angular opening of the detector whose position θ is used for Doppler correction.

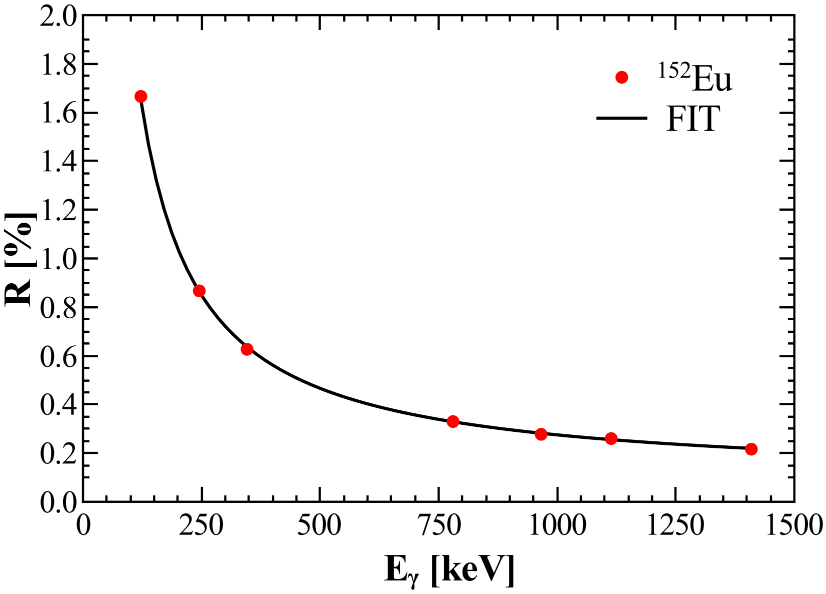

Figure 3.7: Energy resolution of the MINIBALL array as a function of γ-ray energy. The data are taken using a ^{152}Eu source.

The efficiency of the MINIBALL array was studied using three different γ-sources: ^{152}Eu, ^{133}Ba and ^{60}Co. In particular, ^{152}Eu and ^{133}Ba were used to determine the intrinsic efficiency, i.e. the fotopeak probability as a function of energy. The absolute efficiency, which takes into account also the geometrical one, was determined by normalizing the data to those obtained with the ^{60}Co γ-source, determined through the sum-peak method[1] [66].

---

[1] The sum-peak method allows to determine the absolute detection efficiency when the activity of the source is not know. In the case of a ^{60}Co source, it is based on the fact that the 1170 keV and 1330 keV γ-rays are emitted in coincidence. By relating the counts in the single peaks with those in the sum-peak at 2500 keV, the activity of the source is cancelled in the efficiency calculation.

The experimental efficiency data were fitted by the function [67]

$$\epsilon(E_\gamma) = exp\left[a + b\ln\left(\frac{E_\gamma}{200}\right) + c\ln\left(\frac{E_\gamma}{200}\right)^2 + d\ln\left(\frac{E_\gamma}{200}\right)^3 + e\ln\left(\frac{E_\gamma}{200}\right)^4\right] \tag{3.8}$$

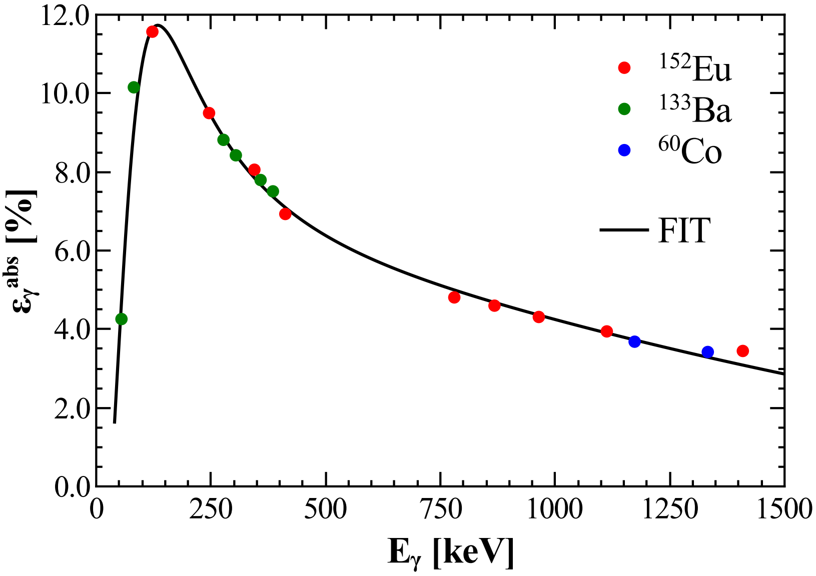

Figure 3.8: Efficiency of the MINIBALL array obtained using ^{152}Eu, ^{133}Ba and ^{60}Co sources. The absolute efficiency was obtained rescaling the curve to ^{60}Co data obtained with the sum peak method, as explained in the footnote of the previous page.

where E_γ is in keV. The result of the fit is shown in Fig. 3.8. The values a = -2.25(1), b = -0.47(3), c = -0.27(3), d = 0.30(2) and e = -0.10(2) were obtained. In this experiment, the efficiency of MINIBALL is ≈ 4.4 % at 1 MeV .

3.2.3 MINIBALL angles

The angles of the MINIBALL array are extremely important for the Doppler correction. The high granularity of the Ge setup allows to reduce the Doppler broadening which affects the FWHM of the γ-peaks, if the position of the Ge segments are known precisely. The position of each crystal was determined experimentally at the beginning of the campaign, by studying the well know γ-spectrum of ^{23}Ne produced in the reaction ^{22}Ne(d,n)^{23}Ne [68]. From the Doppler-shifted spectra, the ϑ-angle of each detector was obtained by fitting the angle that better gives the real energy of ^{23}Ne γ-lines, using Eq.

3.9. The MINIBALL ϑ-angles are listed in Tab. 3.2 and they are referred with respect to the beam direction.

3.2.4 Doppler correction

When a nucleus de-excites emitting γ-rays in flight, the detected energy E_{det} is different from the real one E_{real} due to the Doppler effect. The former can be corrected (E_{DC}) to reconstruct E_{real} (E_{DC} = E_{real}) by

$$E_{\mathrm{DC}} = E_{\mathrm{det}} \frac{1 - \beta \cos \vartheta}{\sqrt{1 - \beta^2}} \tag{3.9}$$

where β = v/c and ϑ is the angle between the γ-ray and the direction of the velocity v or the recoil nucleus. The detected γ energies must be Doppler corrected by using Eq. 3.9. As a consequence of the very inverse kinematics of the reaction studied in this work, the projectile-like scattered nuclei travel downstream in a forward-peaked cone with a narrow angular opening of about 3°. Therefore, their direction can be assumed, with a good approximation, parallel to the beam axis and the ϑ angles needed for the Doppler correction reduce to the MINIBALL angles only, reported in Tab. 3.2. This is an advantage of using such a reaction technique, which doesn't require, to a first approximation, the detection of the recoil nucleus to perform an accurate Doppler correction.

In spite of this, the present data were Doppler corrected on an event-by-event basis, by reconstructing the velocity of the recoil nucleus through the energy of the detected charged particle and assuming an average mass M=100, through the equation

$$\beta_{\mathrm{recoil}} \approx \sqrt{\frac{E_{\mathrm{beam}} - E_{\mathrm{particle}}}{Mc^2}} \tag{3.10}$$

Fig. 3.9 shows the recoil v/c distribution in coincidence with the particle detected in the CD detector. As it can be seen, β values range from about 6.5% for recoils in coincidence with ^{7}Li, to 7.2% for nuclei in coincidence with protons. Such an approach provides a better Doppler correction than using an average v/c. Furthermore, in the inset of the same figure, the dependence on the mass of the recoil nucleus is shown, for the case of coincidences with α particles. It can be clearly seen that a small variation of the mass

Cluster	**Crystal**	ϑ **[deg]**
0	0	108.22
	1	107.19
	2	123.91
1	0	78.78
	1	74.58
	2	61.08
2	0	81.04
	1	65.71
	2	63.52
3	0	109.38
	1	106.99
	2	124.26
4	0	-
	1	-
	2	-
5	0	81.32
	1	75.05
	2	61.95
6	0	104.81
	1	119.29
	2	119.41
7	0	63.31
	1	81.66
	2	70.66

Table 3.2: Polar angles ϑ of MINIBALL detectors determined as explained in the text. Cluster number 4 was not working in the present experiment.

doesn't affect the β distribution, justifying the assumption of an average mass. However, it must be said that some analysis were also done assuming an average β=0.07, especially when particle coincidences were not required.

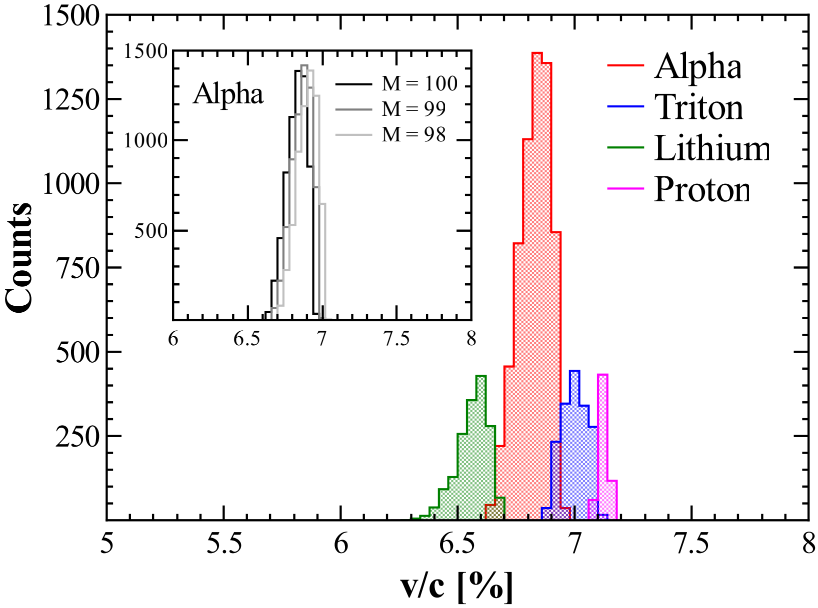

Figure 3.9: v/c recoil distributions in coincidence with α particles (red), tritons (blue), ^{7}Li (green) and protons (purple) reconstructed following Eq. 3.10. Inset: dependence on the mass of the recoil nucleus of the β distribution for coincidences with α particles.

The Doppler correction procedure here described is optimal for prompt γ decays, while it may cause a deterioration of the reconstructed γ-ray energies for isomeric decays. In fact, in this case, γ-rays de-exciting long-living states are emitted few centimetres beyond the target position. As a result, the energies detected are Doppler shifted according to different angles with respect to those used for the correction. This affects the quality of the γ-line shapes as it is in the case of ^{98}Sr, one of the nuclei produced in coincidence with α particles, whose 144 keV transition depopulates the 4 ns 2_1^+ state. Assuming that, on average, ^{98}Sr decays after 4 ns (although this value is the 2_1^+ lifetime and an exponential distribution should be considered), γ-rays are emitted roughly at 8 cm from the target position. Assuming MINIBALL as a perfect spherical detector, such that an average distance from the target and the detectors can be assigned, the real angles ϑ_{real}

are related to the detectors angles ϑ_{det}, reported in Tab. 3.2, by

$$\vartheta_{\text{real}}(\vartheta_{\text{det}}) = \vartheta_{\text{det}} + \arcsin\left(\frac{a \sin\vartheta_{\text{det}}}{\sqrt{a^2 + d^2 - 2ad\cos\vartheta_{\text{det}}}}\right) \tag{3.11}$$

where a ≈ 8 cm is the distance from the target position and d ≈ 14 cm is the distance of the detectors. The real energy E_{real} is therefore detected Doppler shifted according to ϑ_{real} but then it is Doppler corrected (see Eq. 3.9) according to ϑ_{det}. The Doppler corrected energy will have the form

$$E_{DC} = E_{real}\frac{1 - \beta\cos\vartheta_{det}}{1 - \beta\cos\vartheta_{real}} \tag{3.12}$$

Fig. 3.10 shows the effect of such a Doppler correction, resulting in a shift of the reconstructed energy towards smaller energies with respect the real one. This happens both for forward and backward detectors. This shift is clear in Fig. 3.11, where the 144 keV γ-line exhibits a small bump at lower energies.

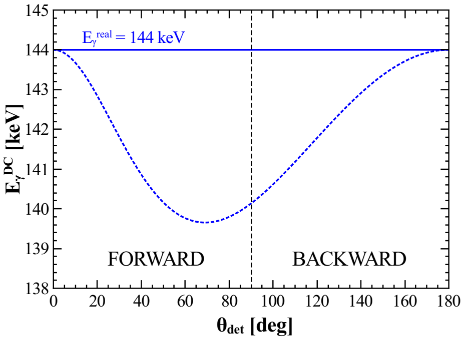

Figure 3.10: Doppler correction for the 144 keV transition (dashed line) depopulating the 4 ns 2_1^+ state in ^{98}Sr which is emitted at ≈ 8 cm from the target position, as reported in Eq. 3.12.

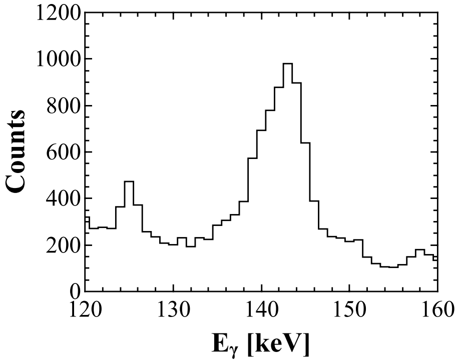

Figure 3.11: 144 keV transition depopulating the 4 ns 2_1^+ state in ^{98}Sr, as measured in the present experiment, showing a small bump at lower energies (see Eq. 3.12 and Fig. 3.10).

3.2.5 γ spectra

The γ spectra detected in MINIBALL were firstly analysed without requiring particle coincidences. In this case, the spectra contain all γ-rays coming from the reactions as well as the background radiation. The second is the dominant one and comes from the β-decay of ^{98}Rb and ^{98}Sr implanted in the scattering chamber. A scheme of the radioisotopes decay is shown in Fig. 3.13. Since ^{98}Rb and ^{98}Sr are far way from the valley of stability, their decay follows a rather long path before ending in the stable ^{96,97,98}Mo nuclei [55]. The presence of such a high background hides completely the γ-rays coming from the reactions. Nevertheless, the γ-rays from β-decay are emitted at rest and Doppler correcting the full spectrum for an average β=0.07 makes them vanish, especially at high energy, as it can be seen in Fig. 3.12.

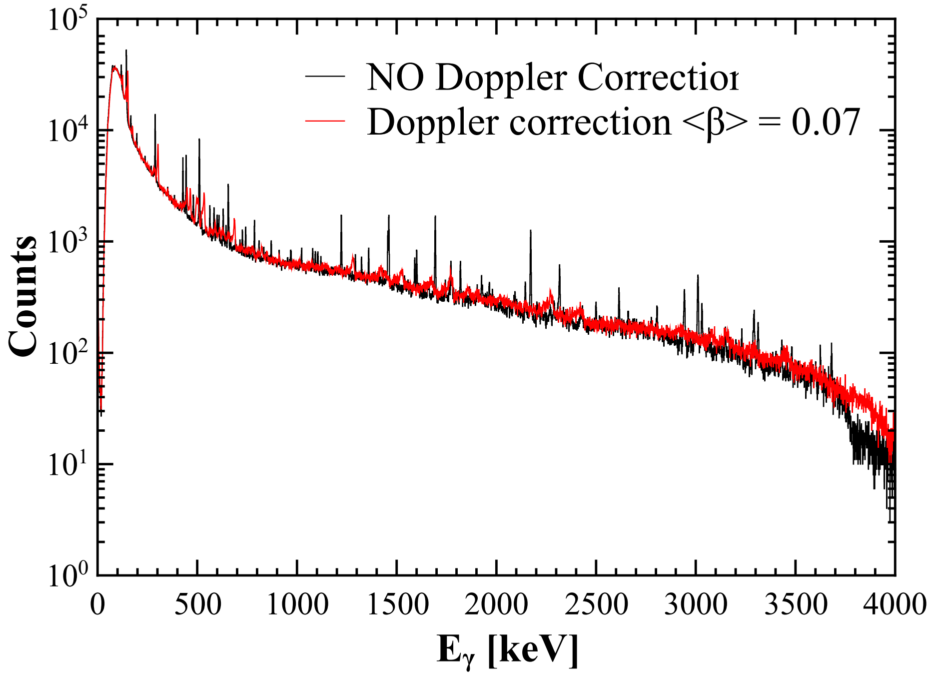

Figure 3.12: Full γ spectrum as detected by MINIBALL during ON-beam windows. The red(black) spectrum is with (without) Doppler Correction.

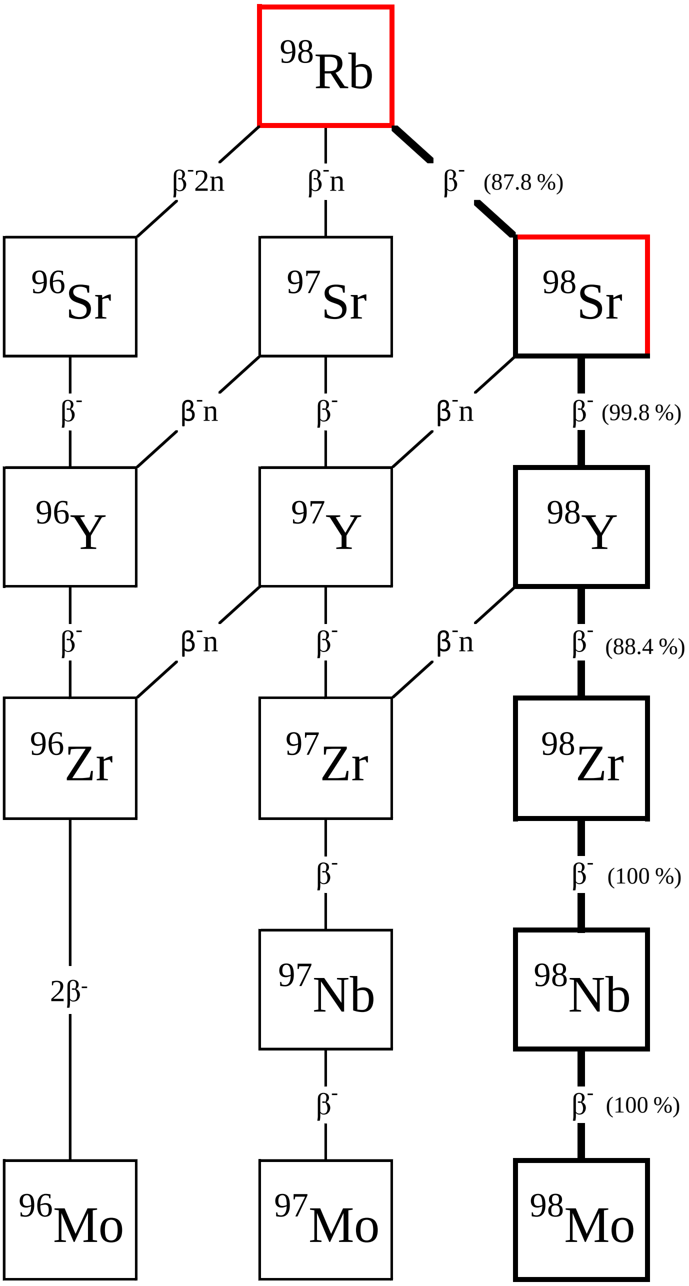

Figure 3.13: β-decay of ^{98}Rb (red) which mainly feeds ^{98}Sr (black). Part of the decay chain following ^{98}Sr is due to the direct decay of ^{98}Sr (red) as a beam component. The decay chain ends with the stable ^{98,97,98}Mo nuclei [55].

A further evidence of the presence of a strong background radiation can be seen comparing ON-beam and OFF-beam spectra, as shown in Fig. 3.14, where the two spectra were normalized to each other. It can be clearly seen that both spectra show the same peaks (see inset (a) of Fig. 3.14), being the background radiation dominant over the γ rays coming from reactions. The difference in the very low energy region (see inset (b) of Fig. 3.14) is given by the x-rays emitted by the last accelerator cavity [30].

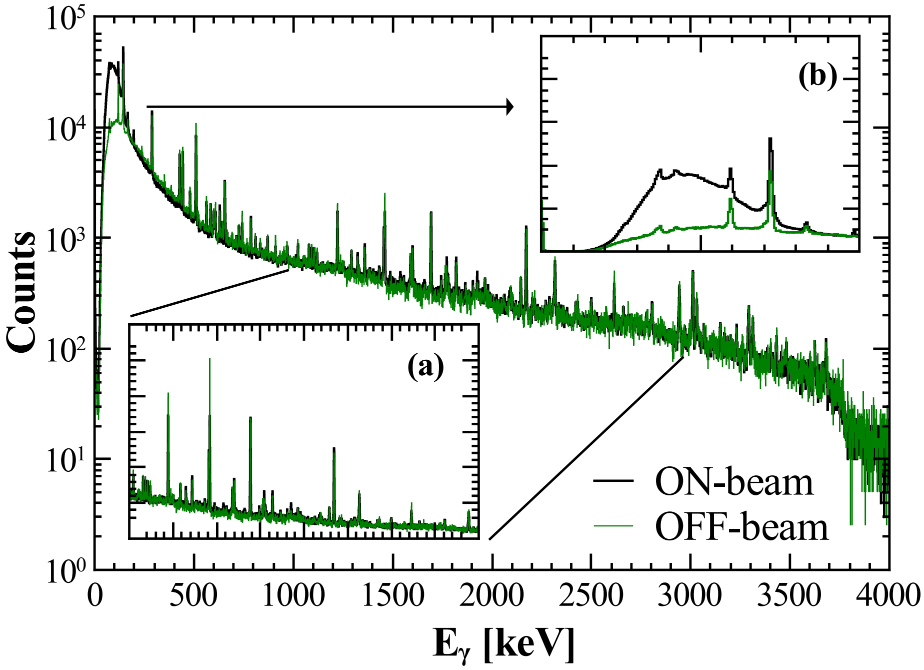

Figure 3.14: Full γ spectrum as measured in the ON-beam time windows (black) and OFF-beam time windows (green). Inset (a): zoom between 1000 keV and 3000 keV showing the overlap between the two spectra. Inset (b): x-rays contribution in the ON-beam spectrum emitted by the last accelerator cavity.

3.2.6 γ-γ coincidences

In order to study reaction channels not associated to the emission of charged particle, such as fusion-evaporation, γ-γ coincidence spectra were built, without requiring particle coincidences. The two-dimensional γ-γ matrix, before the background subtraction, is shown in in Fig. 3.15. In order to remove random γ-γ coincidences a two dimensional gate was used in the E_γ vs time spectrum shown in the inset of Fig. 3.15. As it can be seen in the spectrum, detected γ-rays are correlated within a time window $\approx$ 200 ns wide with time signal of low energy γ-rays slower then for high energy γ-rays (time-walk effect). The requirement of γ fold at least equal to 2 helps to further reduce the background. Nevertheless, it is found that the resulting background subtracted matrix still contains coincidences coming from β decay radiation. The gated projection of such a matrix will be discussed in Chap. 4 in connection with fusion-evaporation reaction channels.

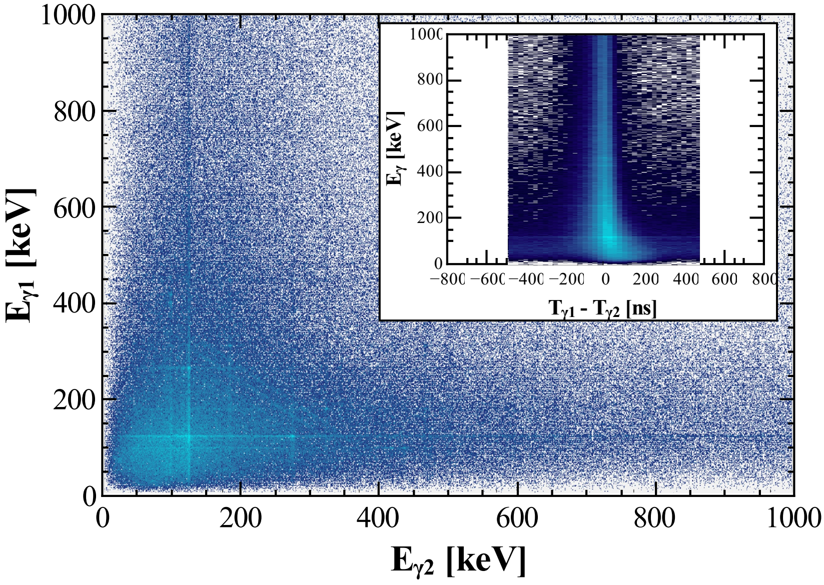

Figure 3.15: γ-γ matrix built without requiring coincidences with particles. Inset: γ energy as a function of two γ-rays time difference, showing the prompt peak as well as the time-walk effect at low energies.

3.3 Particle-γ coincidences

The coincidences between particles and γ-rays are the main and more interesting part of this work, in particular to study the cluster-transfer channels. The requirement of particle coincidences creates a very clean trigger on the channel of interest, removing almost all the background coming from β-decay radiation. Before studying in details the coincidences with each kind of particle, a general particle-γ coincidence spectrum was investigated. As in the case of γ-γ coincidences (discussed in Sec. 3.2.6), the time differences between γ-rays and particles were studied in order to define a prompt coincidence window and a region of random coincidences. The γ energy vs time difference spectrum is shown in Fig. 3.16. Prompt coincidences were generally taken within $\approx$ 200 ns except for the low energy region (<200 keV) where a wider time window was considered, to take into account the time-walk effect. As it can be seen, random coincidences are in this case much less than in the case of γ-γ correlations only, since the particles required in the coincidence conditions, are emitted in the reactions only . The spectrum shown in Fig. 3.16 takes into account all particles, including the non identified ones (i.e. those lying on the diagonal of the CD silicon detector spectrum discussed in Sec. 3.1.5), therefore the projection on the E_γ axis shows γ-lines associated to all reaction channels that produced a charged particle.

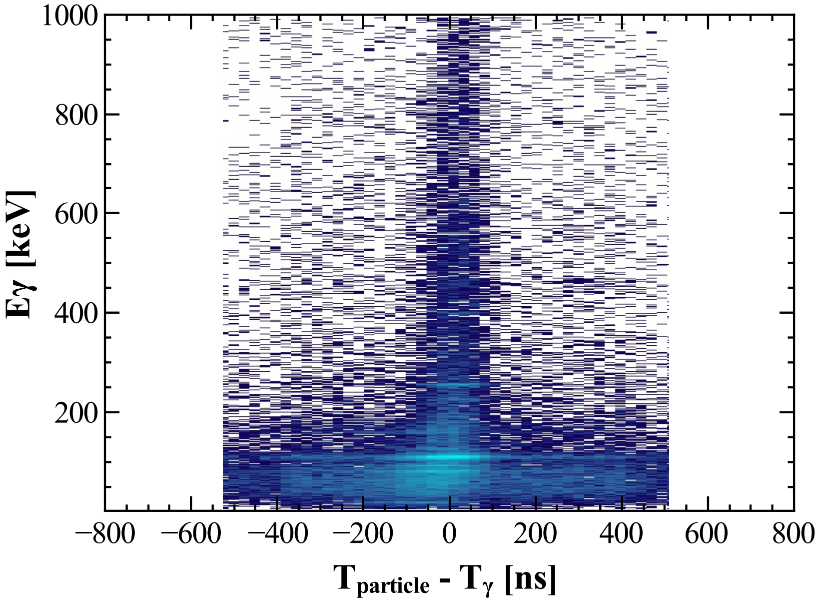

Figure 3.16: γ energy as a function of particles-γs time difference.

Fig. 3.17 shows the γ spectrum in coincidence with all detected particles. The Doppler corrected spectrum for an average β=0.07 is plotted together with the non Doppler corrected one. It can be seen that the background is drastically reduced compared with the total γ spectrum shown in Fig. 3.12 allowing to identify γ-rays coming from the reactions.

It's worth noticing that the non Doppler corrected spectrum is similar to the Doppler corrected one up to 150 keV. Beyond that energy, significant differences appear. For instance, the peak around 197.1 keV disappears completely in the Doppler corrected spectrum. This γ is the $5/2^+ \rightarrow 1/2^+$ transition in ^{19}F, present in the LiF target used in this experiment, which is stopped in the ΔE detector and decays at rest. Furthermore, the 289 keV transition shows the Doppler shifted components at backward and forward angles in the Doppler shifted spectrum, while after the correction the peak can be clearly seen.

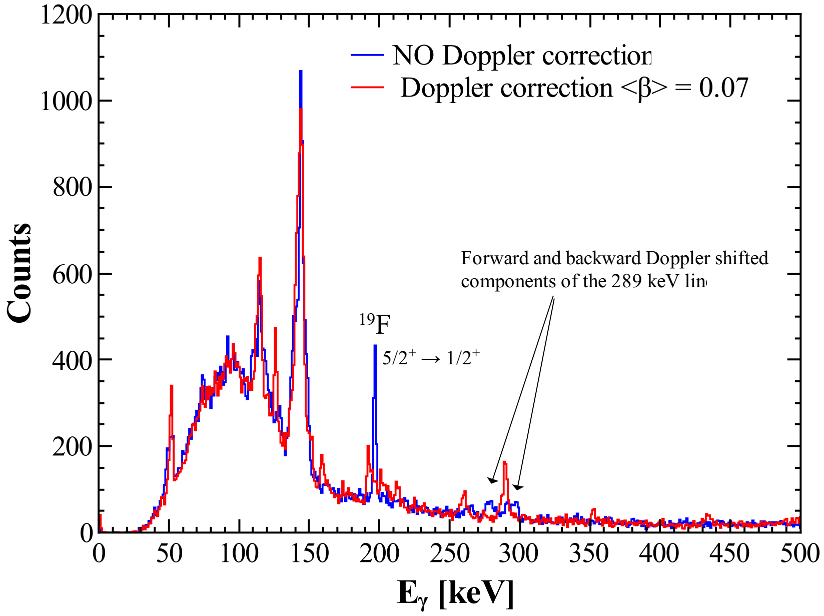

Figure 3.17: γ spectrum as measured in coincidence with all detected particles , including the non identified ones (lying on the diagonal of Fig. 3.5). The blue spectrum is without Doppler correction while the red one assumes an average β=0.07.

A detailed description of particles-γ coincidences considering each detected particle (see Fig. 3.5) will be discussed in Chap. 4. In particular, special attention will be given to coincidences with α particles and tritons which correspond to triton- and α-transfer channels, respectively.

CHAPTER 4

Results and discussion

In this chapter, the results of study of the heavy-ion reaction ^{98}Rb+^{7}Li at 244 MeV will be presented. Due to the composition of the beam (40% ^{98}Rb and 60% ^{98}Sr), reactions took place also on ^{98}Sr, therefore the results will be discussed in parallel.
As it typically happens in heavy-ion collisions close to the Coulomb barrier, several reaction channels are observed, the intensities of which depend on a number of parameters such as relative energy, mass, charge and Q-value [50]. In the present experiment, fast direct mechanisms are observed to compete with slow fusion-evaporation reactions processes, removing flux from the elastic channel.
In the present chapter, all reaction channels measured in this experiment will be discussed and the analysis of particle-γ and γ-γ coincidences will be presented along with the interpretation of the data in terms of γ spectroscopy and reaction dynamics.
In particular, data about elastic and inelastic channels, one-nucleon transfer, break-up and fusion-evaporation will be analysed in details. Special attention will be given to cluster-transfer reactions, the main subject of this work, and to the results achieved in this first test experiment with a radioactive beam.

4.1 Elastic scattering

In the reaction ^{98}Rb + ^{7}Li, discussed in this work, most of the flux measured in the exit channels corresponds to the elastic scattering of ^{98}Rb on ^{7}Li. These events were identified through the detection of ^{7}Li ions in the $\Delta E - E$ Silicon detector, as it can be seen in Fig. 3.5. Due to the double component of the beam ($\approx$40 % ^{98}Rb and $\approx$ 60 % ^{98}Sr discussed in Sec. 4.6.2), part of the data refers to the elastic scattering of ^{98}Sr on ^{7}Li. Nevertheless, the reaction dynamics in the two cases is almost the same, being ^{98}Sr only one proton and one neutron away from ^{98}Rb.

The elastic cross section was studied in terms of angular distribution and experimental data were compared with theoretical calculations, performed with the FRESCO code [34], using a simple optical model (see Sec. 1.3.2). This analysis allowed to extract information on the interference between the Coulomb and the nuclear potentials at this energy, in the angular range covered by the silicon detector. It also served as a test of the optical potential to be used for the calculation of other reaction channels. Furthermore, a normalization coefficient to study cross sections on absolute scale was determined, as well as an average estimate of the beam intensity.

Calculations were performed using global optical parameters of a Woods-Saxon potential (cf. Eq. 1.17), deduced by Cook [69], obtained by fitting several elastic scattering data of ^{7}Li on different targets (A = 24-208) and at different energies (E_{Li}=28-88 MeV). The values used for the various parameters are reported in Tab. 4.1.

V [MeV]	r_V [fm]	a_V [fm]	W [MeV]	r_W [fm]	a_W [fm]
114.2	1.286	0.853	$40.13 - 0.341 \cdot A + 0.00093 \cdot A^2$	1.739	0.809

Table 4.1: Global optical parameters of a Woods-Saxon potential for ^{7}Li elastic scattering on different targets (A=24-208) and at different energies (E_{Li}=28-88 MeV) [69]. V, r_V and a_V are the real depth, radius and diffuseness while W, r_W and a_W are the imaginary depth, radius and diffuseness. A is the mass of the target.

For the radius of the Coulomb potential, it was used

$$R_C = 1.3 \cdot A^{1/3} \tag{4.1}$$

where A is the mass of the heavy nucleus.

It's worth noticing that the energy used for the calculations is the one at mid-target, i.e. 244 MeV, which corresponds to ≈ 17 MeV for a ^{7}Li-induced reaction. Such an energy is outside the range of the experimental data fitted to provide the above mentioned optical parameters. Nevertheless, they turned out to be appropriate also for this case, as it will be shown later.

Because of the impossibility to distinguish ^{98}Rb from ^{98}Sr, the elastic data were considered as one unique set. However, in order to investigate any possible uncertainty due to the beam composition, elastic scattering calculations using both nuclei were done and the comparison is shown in Fig. 4.1, together with the corresponding Rutherford scattering.

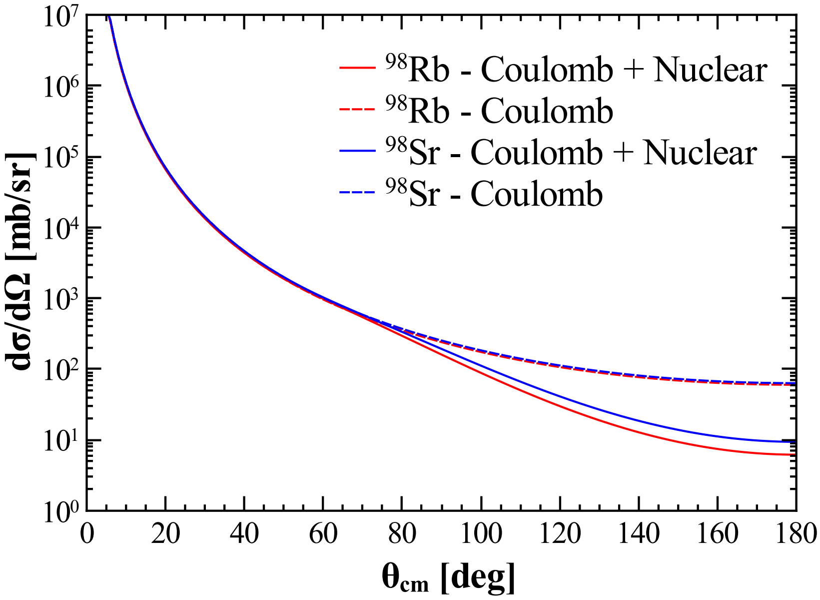

Figure 4.1: Angular distribution of ^{98}Rb elastic scattering (Coulomb + Nuclear) on ^{7}Li (solid red line) and pure Rutherford scattering (dashed red line), plotted together with angular distributions of ^{98}Sr elastic scattering (Coulomb + Nuclear) on ^{7}Li (solid blue line) and pure Rutherford scattering (dashed blue line).

As it can be seen in the plot, ^{98}Rb and ^{98}Sr angular distributions coincide up to 70° and they are essentially Rutherford scattering. The contribution of the nuclear potential starts to be seen at larger angles, making the elastic distributions deviate from the Rutherford ones. Even in this angular region, ^{98}Rb and ^{98}Sr elastic differential cross sections almost coincide.

The very small difference is due to the ^{98}Rb and ^{98}Sr masses because the real value (97.941 and 97.929 u, respectively) were used in the calculations. Nevertheless, this difference can be considered negligible.

The experimental angular distribution for the elastic scattering was determined by looking at the number of counts in the different rings of the CD Silicon detector, taking into account the detection efficiency (and without requiring coincidences with γ-rays). Unfortunately, only few rings could be used, hence few angles, since part of the elastic scattered ^{7}Li ions was fully stopped in the ΔE layer and part of it was out of the range of the detectors. In Fig. 4.2, the experimental points are plotted as a ratio with the Rutherford cross section and in comparison with the calculation performed with the FRESCO code [34], as previously discussed (see Fig. 4.1).

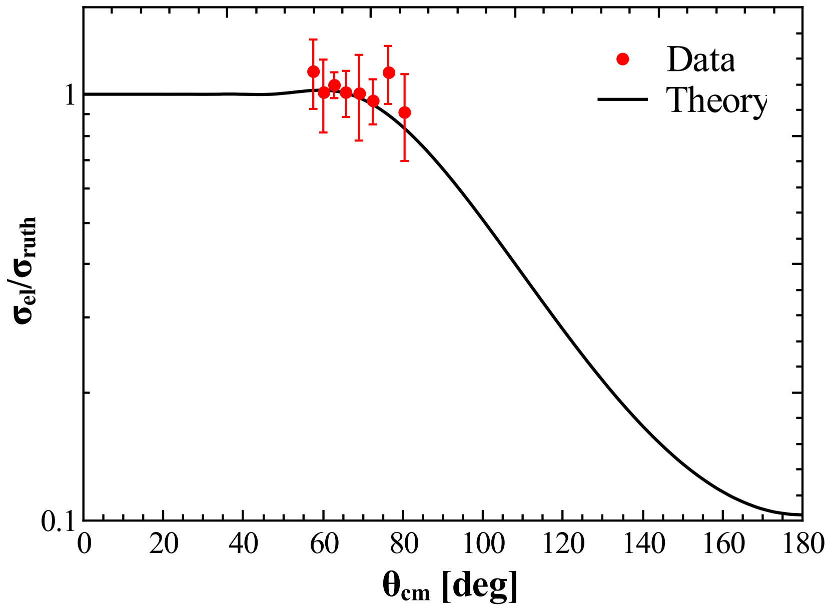

Figure 4.2: Elastic cross section over the Rutherford cross section compared to theoretical predictions as calculated with the FRESCO code [34] assuming an optical model (see Tab. 4.1). The data are normalized considering the average value of the experimental points up to $\vartheta_{cm} = 62°$.

The theoretical calculation predicts a typical Fresnel pattern, for which there is almost no interference between the Coulomb and the nuclear fields at small angles, as it may be expected being the reaction performed around the Coulomb barrier. The drop at larger angles is, on the contrary, the effect of the nuclear potential that makes the cross section deviate from the Rutherford scattering, as it could be also seen in Fig. 4.1.

Experimental points are limited around the maximum of the distribution and they were normalized to the theoretical curve considering the average value of the experimental points up to ϑ_{cm} = 62°. This results in a good agreement with the theoretical prediction. It is important to notice that the normalization factor was determined by normalizing the data to the flat region of the differential cross section, where Rutherford scattering dominates. It is therefore model independent, since it is not affected by parametrization of the nuclear part of the scattering potential. This factor is of key importance for the following analysis, since it provides a conversion coefficient to study cross sections on absolute scale (see Sec. 4.1.1).

It must be said that, among the particles identified as ^{7}Li, there are few events that correspond to ^{6}Li, produced in the one-neutron transfer process and that will be discussed later. Such events can not be separated from ^{7}Li. Nevertheless, the cross section for this process is negligible (few mb) compared to the elastic scattering process (of the order of 200 mb in the angular range covered by the Si detector).

4.1.1 Normalization coefficient

The number of counts C in a ring of the Si detector per unit of solid angle in the centre-of-mass frame of reference was obtained experimentally by

$$C = \frac{N_{\mathrm{D}} J}{\Delta\Omega} \tag{4.2}$$

where N_D is the number of particles detected in the ring of the Si detector and corrected for the detection efficiency, J is the Jacobian linking cross sections in the laboratory system to those in the center of mass system (see App. A) and $\Delta\Omega$ is the solid angle covered by the ring. The differential cross section is instead defined by

$$\frac{d\sigma}{d\Omega} = \frac{N_{\mathrm{D}} J}{N_0 n \Delta\Omega} \tag{4.3}$$

where N_0 is the number of incident particles and n is the surface density of the target. If the number of counts C are normalized to a theoretical cross section $d\sigma/d\Omega$, the ratio S between them

$$S = N_0 n \tag{4.4}$$

provides a scaling factor which allows to study experimental cross section on absolute scale, since it is the normalization coefficient between data and theory that takes into account the duration of the experiment and the density of the target. In this experiment, it was found

$$S = 221(10) \quad \mathrm{mb}^{-1} \tag{4.5}$$

4.1.2 Beam intensity

From the scaling factor S it is possible to determine the average beam intensity I_0. In fact

$$I_0 := \frac{N_0}{\Delta t} = \frac{S}{n \Delta t} \tag{4.6}$$

being Δt the duration of the experiment. Using $\Delta t \approx$ 80 h and n=1.5 mg/cm^2, the average beam intensity during the experiment was

$$I_0 = 2.16 \cdot 10^4 (15) \quad \text{pps} \tag{4.7}$$

It should be noticed that the beam intensity is referred to the total beam, hence including both ^{98}Rb and ^{98}Sr components. According to the estimated composition (see Sec. 4.6.2), the two nuclei had an average intensity of $\approx$ 9·10^3 pps and $\approx$ 1.3·10^4 pps, respectively. This will be reflected in the total γ-rate for each specific reaction channel.

4.2 Inelastic scattering

Among ^{7}Li identified nuclei, there are few events that correspond to the inelastic excitation of both ^{98}Rb and ^{98}Sr and that were measured in coincidence with γ-rays. It is important to notice that at this energy and according to the angles of particle detection, the inelastic excitation is far from being in the regime of pure Coulomb excitation (referred as ”safe Coulex”)[1] [70]. As a consequence, both the Coulomb and the Nuclear fields contribute to the excitation. However, the relative strength can not be investigated, because the poor statistics prevents the possibility to study differential cross sections for the inelastic scattering channel. Since during inelastic excitation part of the kinetic energy is transferred to the internal states of the recoil, the average energy of the inelastic scattered ^{7}Li nuclei is less than the elastic one.

---

[1] A safe Coulex is defined by the Cline's safe ”energy” criterion [70] which states that if the distance between the nuclear surfaces is greater than 5 fm, the nuclear interaction is negligible. This means that the bombarding energy E_b

$$E_\mathrm{b}(\vartheta_\mathrm{cm}) = 0.72 \frac{Z_\mathrm{p} Z_\mathrm{t}}{d_\mathrm{min}} \frac{A_\mathrm{p} A_\mathrm{t}}{A_\mathrm{t}} \left[1 + \frac{1}{\sin\left(\frac{\vartheta_\mathrm{cm}}{2}\right)} \right] \tag{4.8}$$

must be such that the distance of closest approach d_min satisfies

$$d_\mathrm{min} > 1.25(A_\mathrm{p}^{1/3} + A_\mathrm{t}^{1/3}) + 5 \tag{4.9}$$

for all the scattering angles ϑ_cm. Z_p, A_p, Z_t and A_t are the charge and mass of projectile and target.

As a result, most of inelastic scattered ^{7}Li particles didn't punch through the ΔE detector and in Fig. 3.5 they lie on the diagonal. Although they can not be identified, the γ events can be recovered considering also the coincidences with unidentified particles along the diagonal.

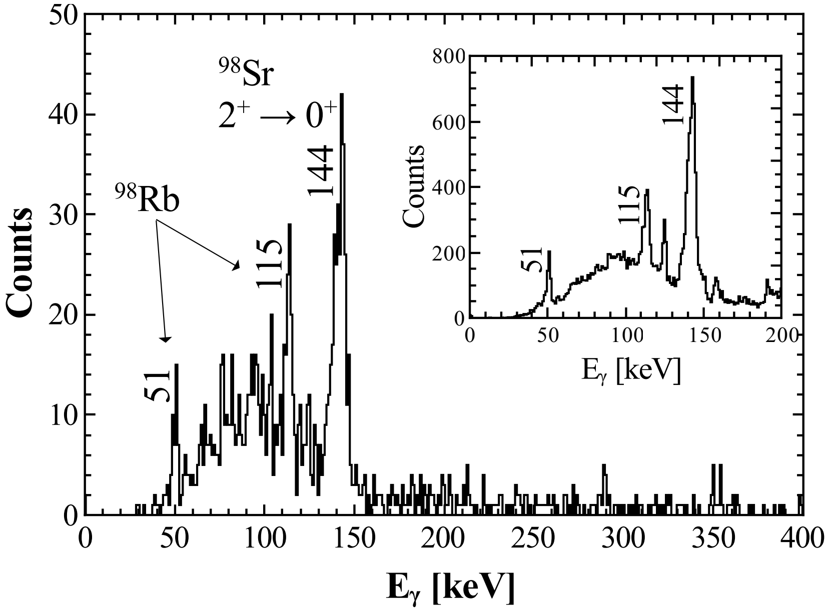

Figure 4.3: γ-rays in coincidence with identified ^{7}Li ions showing inelastic excitation of both ^{98}Rb and ^{98}Sr beam components. While the 144 keV line is the $2^+ \rightarrow 0^+$ transition of ^{98}Sr, the 51 keV and 115 keV lines probably belong to ^{98}Rb (see discussion in the text). Inset: γ-rays in coincidence with all detected particles, showing the enhancement of the inelastic channel. This effect is due to the inclusion of ^{7}Li and ^{19}F ions which didn't punch through the ΔE detector.

Among the recovered events, there are many ^{19}F ions, present in the target, which also inelastic scattered with a cross section higher then in the ^{7}Li case (mainly due to the Coulomb field). Therefore, the total measured γ spectrum contains a mixture of different inelastic processes. Despite the fact that these channels can not be studied in terms of reaction dynamics, because of the impossibility to distinguish between the different contributions, they provide information about the structure of the beam components, especially in the case of ^{98}Rb which is almost unknown.

In Fig. 4.3 the γ spectrum measured in coincidence with identified ^{7}Li ions and Doppler corrected event by event is shown. As it can be seen, the $2^+ \rightarrow 0^+$ transition at 144 keV

in ^{98}Sr is clearly visible, confirming the presence of ^{98}Sr as a beam component. Besides this, two strong γ lines at 51 keV and 115 keV show up. Since they don't belong to ^{98}Sr (they should be transitions connecting low-lying states in this nucleus whose structure is very well known), they are likely to belong to ^{98}Rb, whose known level scheme is limited to the ground state and to the 139 ms isomer at 270 keV, as shown in Fig. 2.6. It is in fact reasonable that also ^{98}Rb is excited in this reaction. Such γ lines are enhanced by requiring the coincidence with all particles, including the diagonal, where the unidentified scattered particles lie (see discussion above), as shown in the inset of the same figure.
By looking at γ-γ coincidences, it is also clear that, despite the rather high intensity in the spectrum in single, the two possible γ-lines of ^{98}Rb don't seem to be in coincidence with each other, as shown in Fig. 4.4 and Fig. 4.5.

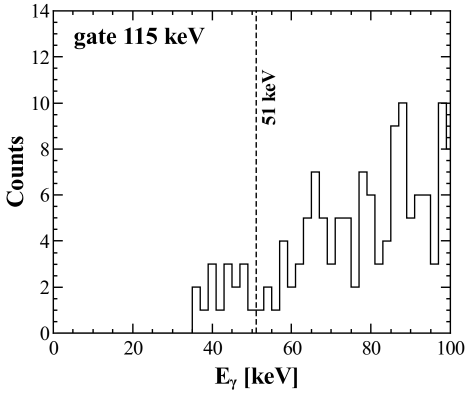

Figure 4.4: Projection of the particle-γ-γ matrix gated on the 115 keV transition showing the absence of the coincidence with the 51 keV γ-line.

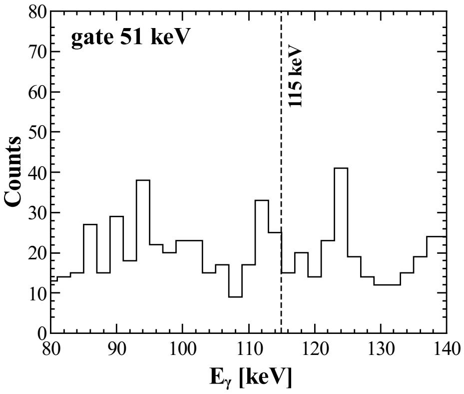

Figure 4.5: Projection of the particle-γ-γ matrix gated on the 51 keV transition showing the absence of the coincidence with the 115 keV γ-line.

This result suggests that they might be either two cross over transitions depopulating two different states built on the ground state, or two γ-rays one feeding the ground state and one the 270 keV isomer. In the latter case, the decay from the isomer would be also expected. Nevertheless, the 138 ms lifetime of the isomeric state does not allow to observe its decay in the present experiment where only prompt coincidences were detected.

Moreover, due to the lack of statistics it was not possible to correlate the ^{98}Rb excitation energy with the γ decay, which would have provided further information on the location of the 51 and 115 keV transitions. Also including the recovered particles, it would be impossible to reconstruct their kinematics since ^{7}Li and ^{19}F ions could not be distinguished.
It is interesting to notice that the same γ-lines with the same intensity ratio were observed in a recent Coulomb excitation experiment, also performed at ISOLDE, using a ^{98}Sr beam contaminated by ^{98}Rb [71]. Finally, other weaker γ-lines can be seen in the spectrum shown in Fig. 4.3, but the poor statistics doesn't allow to determine their nature.

4.3 One-proton and one-neutron transfer

One-nucleon transfer was also observed in this experiment. Tab. 4.2 shows the products of one-neutron and one-proton stripping (i - iii) and pick-up (ii - iv) on both the ^{98}Rb and ^{98}Sr beam components. The terms "stripping" and "pick-up" are referred to the target nuclei.

Beam	**n-stripping**	**n-pick-up**	**p-stripping**	**p-pick-up**
^{98}**Rb**	^{99}Rb - ^{6}Li	^{97}Rb - ^{8}Li	^{99}Sr - ^{6}He	^{97}Kr - ^{8}Be
^{98}**Sr**	^{99}Sr - ^{6}Li	^{97}Sr - ^{8}Li	^{99}Y - ^{6}He	^{97}Rb - ^{8}Be

Table 4.2: Products of one-proton and one-neutron pick-up and stripping on both the ^{98}Rb and ^{98}Sr beam components.

In particular, one-proton stripping and one-neutron stripping leading to the target-like nuclei ^{6}He and ^{6}Li, respectively, were measured. Due to the little statistics, these channels could only be used to give an indication on the feasibility of one-nucleon transfer reactions between heavy-ion with radioactive beams. In the following, a brief description of each reaction channel is given.

i) *One-neutron stripping*: the one-neutron stripping channel is associated to the emission of ^{6}Li. Due to the rather negative Q-value Q_{gg}=-2.6 MeV for ^{98}Rb and Q_{gg}=-3.7 MeV for ^{98}Sr, the population of excited states is an inhibited process (see Sec. 1.3.9). Moreover, the known discrete levels in ^{6}Li are above 2 MeV and they were probably not populated.

On the other hand, ^{6}Li in the ground state can not be separated from ^{7}Li in the $\Delta E - E$ matrix. An attempt was done by searching for γ-coincidences with transitions in the projectile-like ^{99}Rb and ^{99}Sr nuclei. In the first case, no γ-lines are known while in the second no γ-rays were recognised in the spectrum. However, it is important to note that ^{6}Li has a prominent cluster structure and it breaks-up into $\alpha - d$ at 1.47 MeV [18]. In fact, deutrons were observed in the $\Delta E - E$ matrix, which might be an indication that one-neutron stripping was actually observed and the very few counts indicate that the cross section for this process is very small. It should be said that deutrons may also come from one-neutron pick-up by the protons present in the target.

ii) *One-neutron pick-up*: one-neutron pick-up would be associated with the detection of ^{8}Li, which may not be distinguished from ^{7}Li in the $\Delta E - E$ matrix. Moreover, the system ^{7}Li+n is unbound at 2 MeV and, in this case, the detected nuclei would be again ^{7}Li particles. In this case, the Q-values are Q_{gg}=-1.9 MeV for reaction on ^{98}Rb and Q_{gg}=-3.8 MeV for reaction on ^{98}Sr. Also in this reaction channel, no γ-rays of projectile-like ^{97}Rb and ^{97}Sr were measured in coincidence with ^{8}Li ions.

iii) *One-proton stripping*: the one-proton stripping channel was studied by tagging on the ^{6}He ions detected in the Silicon detector, as shown in Fig. 3.5. This process leads to the projectile-like nuclei ^{99}Sr and ^{99}Y for reactions on the ^{98}Rb and ^{98}Sr beam components, respectively. The reaction has a Q-value Q_{gg}=5.1 MeV in the case of ^{98}Rb and Q_{gg}=0.8 MeV for ^{98}Sr. The estimated optimum Q-value according to Eq. 1.62 is $Q_{opt} \approx$ -5 MeV, which implies that the expected excitation energy is $\approx$ 10 MeV for ^{99}Sr and and $\approx$ 5 MeV for ^{99}Y. Despite the high excitation energy, the very low statistics prevented the possibility to study γ-rays in coincidence with ^{6}He. On the other hand, it was possible to extract the experimental angular distribution, even though for very few angles, which provides the order of magnitude of the cross section for this process. Also in this case, no distinctions were made between ^{98}Rb and ^{98}Sr beam components. The angular distribution is shown in Fig. 4.6. The integrated cross section in the measured angular range is σ = 2.1(1) mb.

iv) *One-proton pick-up*: to conclude the discussion on one-nucleon transfer channels, it's worth mentioning the one-proton pick-up reaction which is usually quite a strong channel observed in experiments performed in direct kinematics with stable beams.

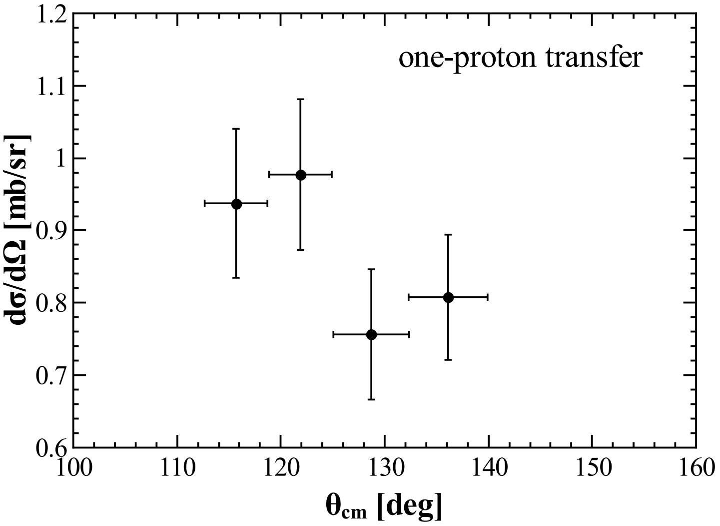

Figure 4.6: ^{6}He angular distribution corresponding to the one-proton stripping reaction ^{98}Rb(^{7}Li,^{6}He)^{99}Sr. The absolute cross section was obtained by scaling the experimental data according to the normalization factor S of Eq. 4.5.

This transfer process leads to unbound ^{8}Be target-like nuclei that decay emitting two α particles. In a recent ^{7}Li+^{208}Pb experiment performed at sub-barrier energies, the measured Q-value for the different reaction channels shown in Fig. 4.7 clearly shows a dominant contribution coming from ^{8}Be beak-up into two α particles [72]. Nevertheless, no evidences of this channel were seen in the present experiment. If the channel were opened, $\alpha - \gamma$ coincidences would show γ- transitions of ^{97}Kr and ^{97}Rb projectile-like systems with a strength comparable or even larger than other channels. It might be speculated that the absence of this channel may be a consequence of the evolution of the reaction dynamics when exotic nuclei are involved.

In fact, in the case of the work of Luong et al. [72], such a channel is particularly favoured being Q_{gg}=9.2 MeV and $Q_{opt} \approx$ 8.7 MeV, which is where the Q-value distribution is peaked. This can be seen in Fig. 4.7, which shows the ground state and the first excited states in the target like nucleus ^{207}Tl between 5 and 10 MeV (green Q-value distribution). Going towards the neutron drip-line, the situation changes since Q_{gg} associated to one-proton pick-up decreases, as it is shown in Fig. 4.8 for the Rb isotopic chain, while Q_{opt} remains constant. As a consequence, for the ^{97}Kr and ^{97}Rb nuclei studied in this work, the cross section is hindered by optimum Q-value considerations. This may justify the unmeasured ^{8}Be channel in the present experiment.

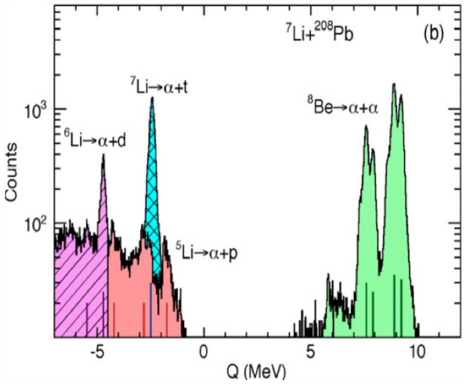

Figure 4.7: Measured Q-value spectrum for the reaction ^{7}Li+^{208}Pb at 29 MeV from the work of ref. [72]. The contribution from one-proton transfer channel is associated to the emission of ^{8}Be. In the spectrum, the ground state and the first excited states in ^{207}Tl can be seen (green areas).

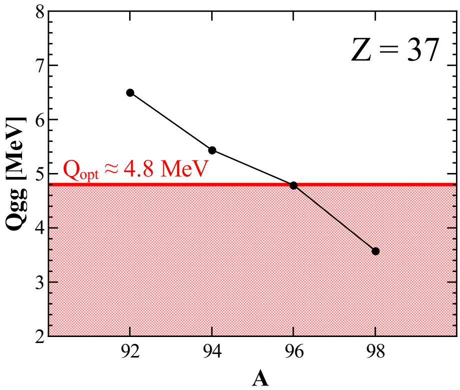

Figure 4.8: Q_{gg} as a function of mass number for Rb (Z=37) isotopic chain for the reaction ^{A}Rb(^{7}Li,^{8}Be)$^{A-1}$Kr. The solid red line shows the expected optimum Q-value and the shaded coloured area represents the region where the cross section is hindered by optimum Q-value considerations.

4.4 ^{7}Li breakup

In nuclear reactions involving weakly bound nuclei with a cluster structure, such as ^{7}Li (with a t-α separation energy $S_{(t-\alpha)}$ = 2.5 MeV), break-up has to be taken into account as a possible reaction channel removing flux from the initial beam [33]. Two different processes may occur. The first one is called elastic break-up, when the ^{7}Li nucleus breaks-up into the two fragments without any excitation of the other nucleus. In the second case, the other nucleus is excited and the channel is characterised by the emission of γ-rays. The latter is usually called inelastic break-up.

Both channels were investigated in the present experiment. Elastic break-up corresponds to the emission of tritons and α-particles not in coincidences with γ-rays. Due to electronics problems, triton-α coincidences couldn't be measured. Hence, the elastic break-up channel was studied by looking at tritons and α particles separately, comparing events not in coincidences with γ-rays. It was found, in both cases, that particles coming from elastic break-up are less than 20 % of the total detected particles. The so found values are anyway affected by large uncertainties due to the fact that the efficiency of γ detection may influence particle γ-rays coincidences.

On the contrary, inelastic break-up should be measured in coincidences with γ-rays of beam nuclei, i.e. ^{98}Rb and ^{98}Sr. The γ spectrum is therefore supposed to be similar to the one discussed in Sec. 4.2 in connection with the inelastic excitation of the beam. Since these γ-lines don't show up in the spectrum with a tagging on the α or triton particles, as it will be discussed in the next section, it is possible to conclude that the inelastic break-up can be considered negligible.

4.5 Cluster-transfer: general considerations

The main subject of this work is the study of cluster-transfer channels, namely the transfer of either tritons or α particles from the ^{7}Li target to the beam nuclei. These channels were investigated by particle-γ coincidences, by detecting the emitted complementary charged cluster. For the first time, this process was tested with a radioactive beam in inverse kinematics at energies around the Coulomb barrier, as a possible tool for spectroscopic studies of neutron-rich nuclei. In fact, so far, only direct reactions with ^{7}Li beam on stable target were performed.

Cluster-transfer is observed when a weakly bound nucleus with a prominent cluster structure, such as ^{7}Li in this experiment, is involved in the reaction. In fact, due to a binding energy energy of 2.5 MeV, ^{7}Li easily breaks-up into triton- and α-clusters and one of the two fragments has a sizeable probability to be captured. This process is favoured at energies around the Coulomb barrier and below a critical value of angular momentum of the relative motion, such that the final system can survive against fission [13, 44]. These reactions are characterized by a very high and positive Q-value, while the expected optimum Q-value is rather negative (see Eq. 1.62). This results in a rather high excitation energy, therefore such a mechanism can be used as a tool to perform γ spectroscopy studies. Owing to the high excitation energy of the final systems above the neutron threshold, γ-emission is preceded by few neutrons evaporation. This means that more than one nucleus can be studied at the same time following cluster capture. Besides the excitation energy, the transfer of a massive cluster also carries large angular momentum (tens of $\hbar$). Hence, high-spin yrast states can be populated as well as off-yrast levels at medium-high angular momentum.

It is important to note that the detection of α-particles and tritons results in a very clean trigger on cluster-transfer channels. As discussed in the previous section, γ-rays measured in coincidence with α particles and tritons are uniquely associated to this process, the inelastic break-up being negligible. This means that the combination of particles detection with γ-rays detection is a powerful tool to investigate such a reaction channel. The possibility of exploiting this experimental technique in connection with γ spectroscopy of neutron-rich nuclei produced in cluster-transfer reactions performed with radioactive beams at low intensities is clearly fundamental to overcome the limitations coming from the low cross section of the process. In fact, the study of these reaction channels would be impossible in experiments using stand-alone γ detectors.

In this work, triton- and α-transfer were studied in details. A full in-beam γ spectroscopy was performed to test the potentiality of this mechanism. Furthermore, an accurate analysis of the distributions of the residues was done, by studying the neutron evaporation as a function of excitation energy and spin distributions. Information on the reaction mechanism were deduced by comparing differential cross sections as a function of excitation energy and scattering angles with theoretical predictions within the framework of a direct transfer of a cluster-like particle, assuming a 1-step DWBA approximation (see Sec. 1.3.5).

It must be said that the limitations imposed by the low beam intensity, the short beam time, the beam impurity and the low γ efficiency largely affected the collected statistics, limiting the possibility to perform an exhaustive analysis, especially in connection with γ spectroscopy. Nevertheless, the achieved results clearly demonstrate the validity of the experimental technique, serving as a benchmark for future experiments.

4.6 Cluster-transfer: spectroscopy studies

Tritons and α-particles detected in the CD Silicon detector (see Fig. 3.5) correspond mainly to α- and triton- transfer channels, respectively. The coincidences with γ-rays allowed to extract information on the populated nuclei as well as on their energy and spin. Particle-γ coincidences were built within a 200 ns coincidence time window, as it is shown in Fig. 4.9 and in Fig. 4.10. In this case, the background subtraction did not played a crucial role, since the coincidences with particles were required. It is found that the majority of the background comes from random γ-rays emitted by the β-decay of implanted nuclei, without being in coincidence with any particle.

Since reactions occurred on both beam components, i.e. ^{98}Rb and ^{98}Sr, a wide number of isotopes was populated. The expected channels are schematically shown in Fig. 4.11.

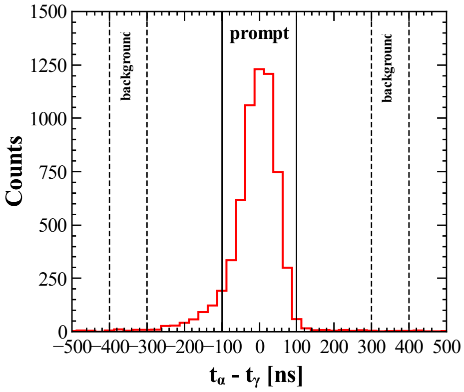

Figure 4.9: Time difference distribution between α-particles and γ-rays corresponding to the triton-transfer channel. Vertical lines show the prompt peak and the background regions.

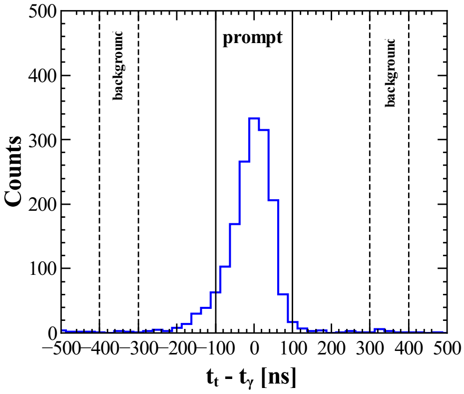

Figure 4.10: Time difference distribution between tritons and γ-rays corresponding to the α-transfer channel. Vertical lines show the prompt peak and the background regions.

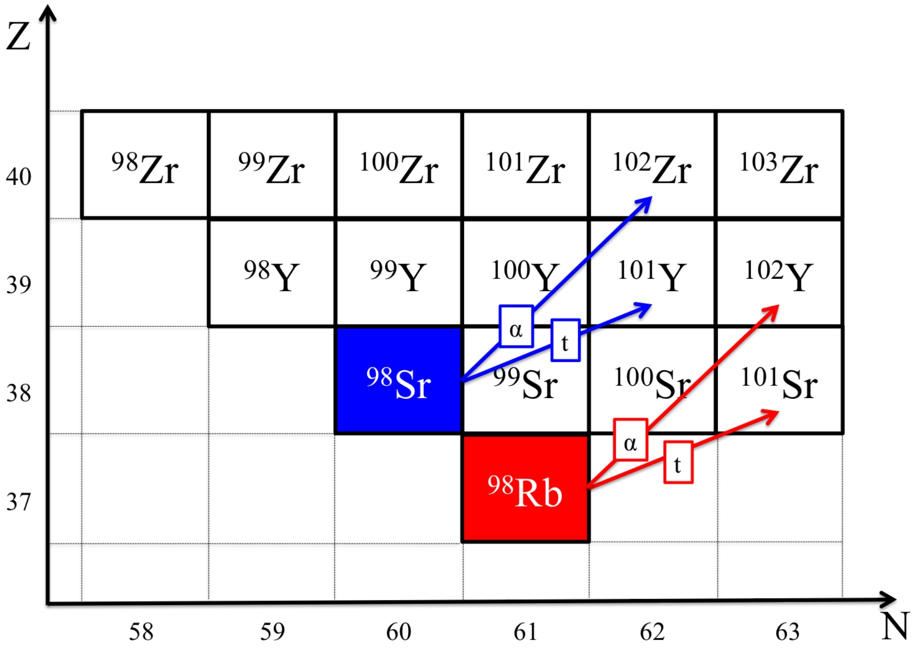

Figure 4.11: Nuclei populated by a direct transfer of either tritons or α particles to the ^{98}Rb and ^{98}Sr beam components.

It can be seen that triton-transfer on ^{98}Rb leads to ^{101}Sr while α-transfer populates ^{102}Y. On the other hand, reactions on ^{98}Sr populated ^{101}Y and ^{102}Zr in the triton- and α-transfer channels, respectively. As discussed in Sec. 4.5, cluster-transfer is followed by few neutrons evaporation, hence the final residues will be distributed around smaller masses than the nuclei populated directly.

The prompt Doppler corrected α-γ spectrum, corresponding to the triton-tranfer channel, is shown in Fig. 4.12 and the level schemes, built on the basis of the detected γ-rays, are presented in Fig. 4.13. In the case of α-transfer, the prompt Doppler corrected triton-γ spectrum is shown in Fig. 4.14 and the corresponding level schemes in Fig. 4.15. In the case of triton-transfer spin up to 6 $\hbar$ were observed while for α-transfer levels up to 4 $\hbar$ were measured. In both cases, only states below 1 MeV were observed. This happens both for reactions on ^{98}Rb and ^{98}Sr beam components.

It is important to say that all transitions measured in the cluster-transfer channels are known. In fact, it was not expected to detect new γ-rays since the level schemes of the final products are very well known [55], also off-yrast, and the experiment was very short. On the other hand, this mass region served as a testing ground to study such a technique, and the knowledge of the structure of the populated nuclei helped in the description of the process.

It is important to notice that for reactions on ^{98}Rb both 3- and 2-neutrons evaporation channels were observed, while for ^{98}Sr only the 2n channel could be seen. This feature will be discussed in Sec. 4.6.1.

In Tab. 4.3 and Tab. 4.4, a summary of the nuclei produced in triton- and α-transfer, respectively, is reported together with the measured γ-rays. Relative intensities, as measured in this experiment, are also given. They were calculated taking into account both the detection efficiency ε (see Fig. 3.8) and the internal conversion coefficients α as reported in the literature [55].

The number of counts C in each γ peak were converted into intensities by the relation

$$I_\gamma = \frac{\alpha + 1}{\varepsilon} C \tag{4.10}$$

where the γ intensities were determined relatively to the ground state transitions which collect all the measured decay flux.

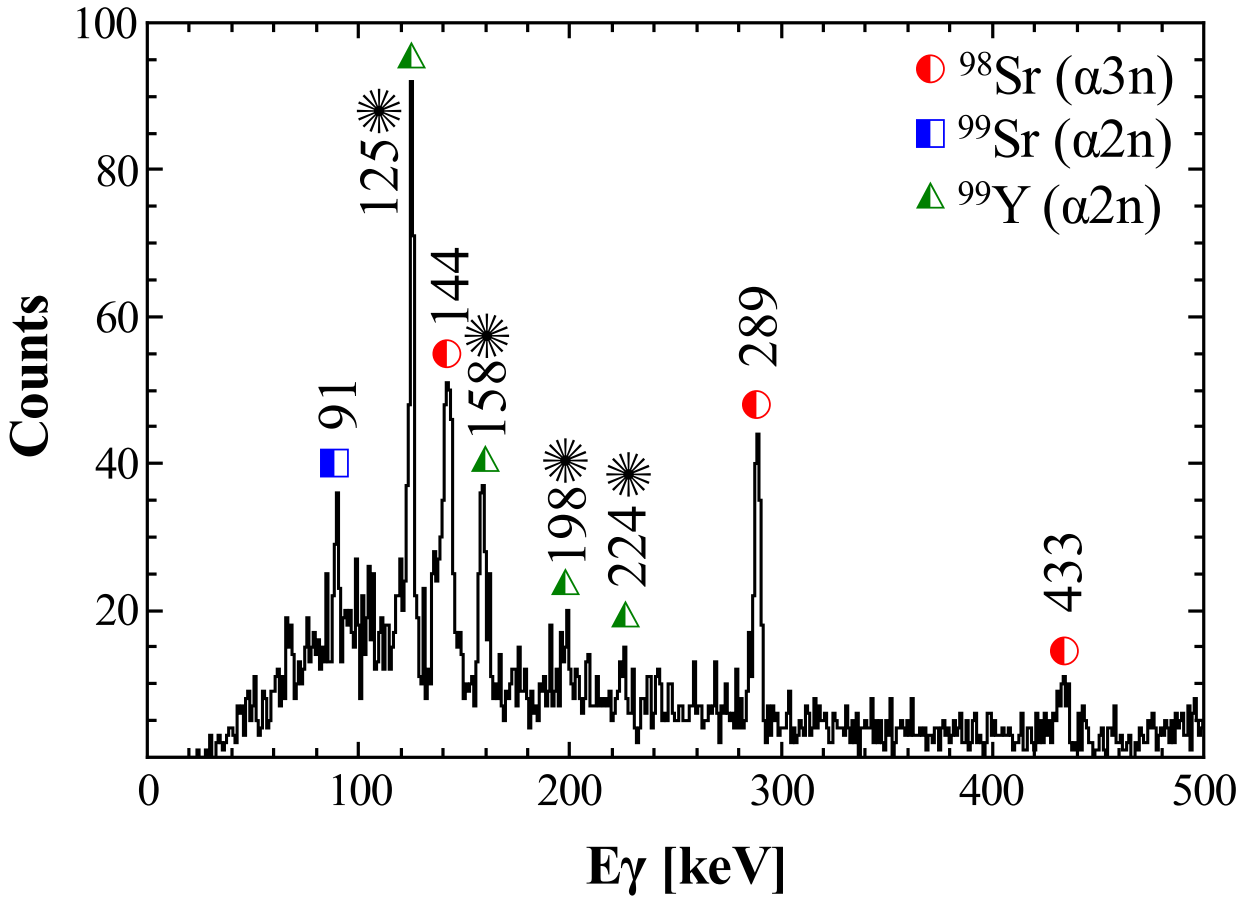

Figure 4.12: α-γ coincidences corresponding to the *triton*-transfer channel. For reactions on the ^{98}Rb beam component, the 3n channel (^{98}Sr) is indicated by circles while the 2n channel (^{99}Sr) is indicated by squares. γ lines corresponding to reactions on the ^{98}Sr beam component are labelled with a star and the 2n channel (^{99}Y) is indicated by triangles.

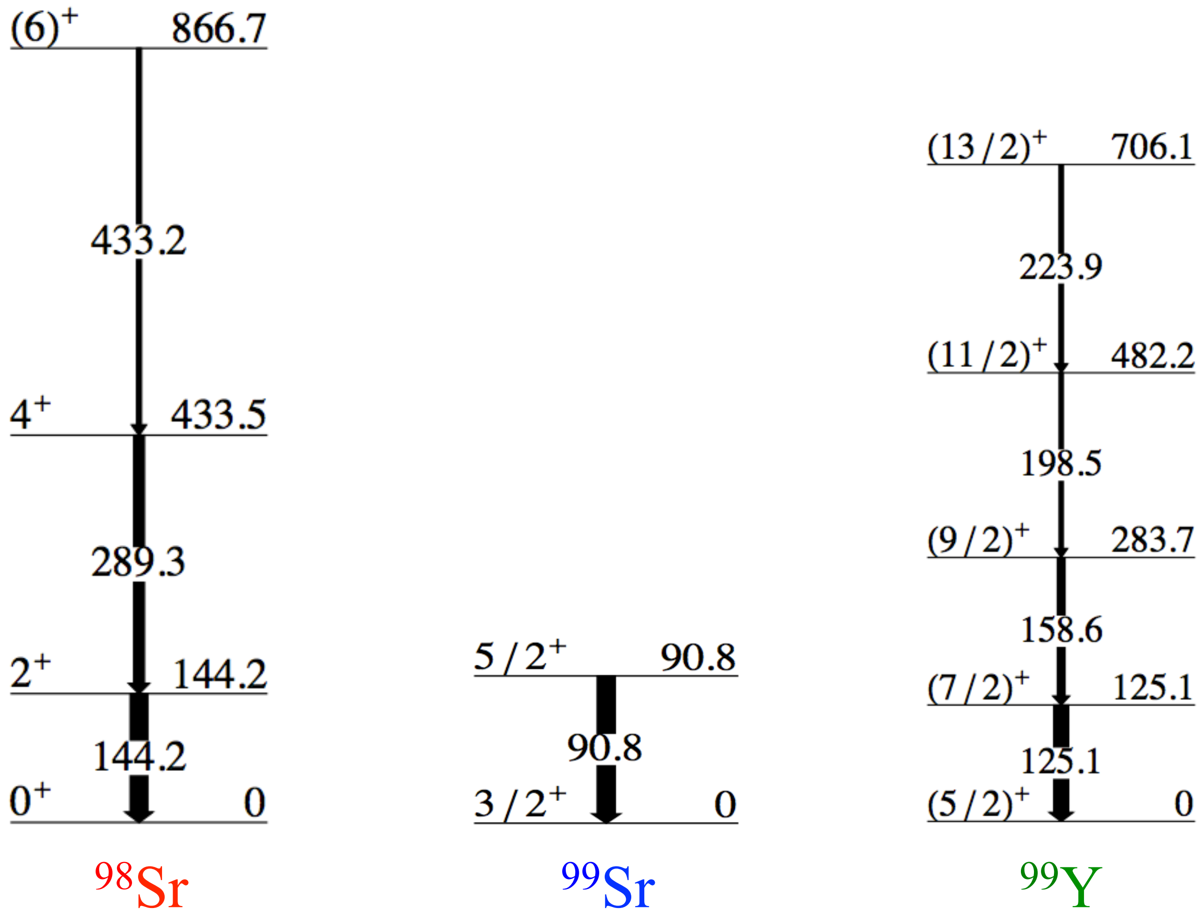

Figure 4.13: Level schemes built on the basis of the γ detected in the α-γ spectra corresponding to the triton-transfer channel (cf. Fig. 4.12).

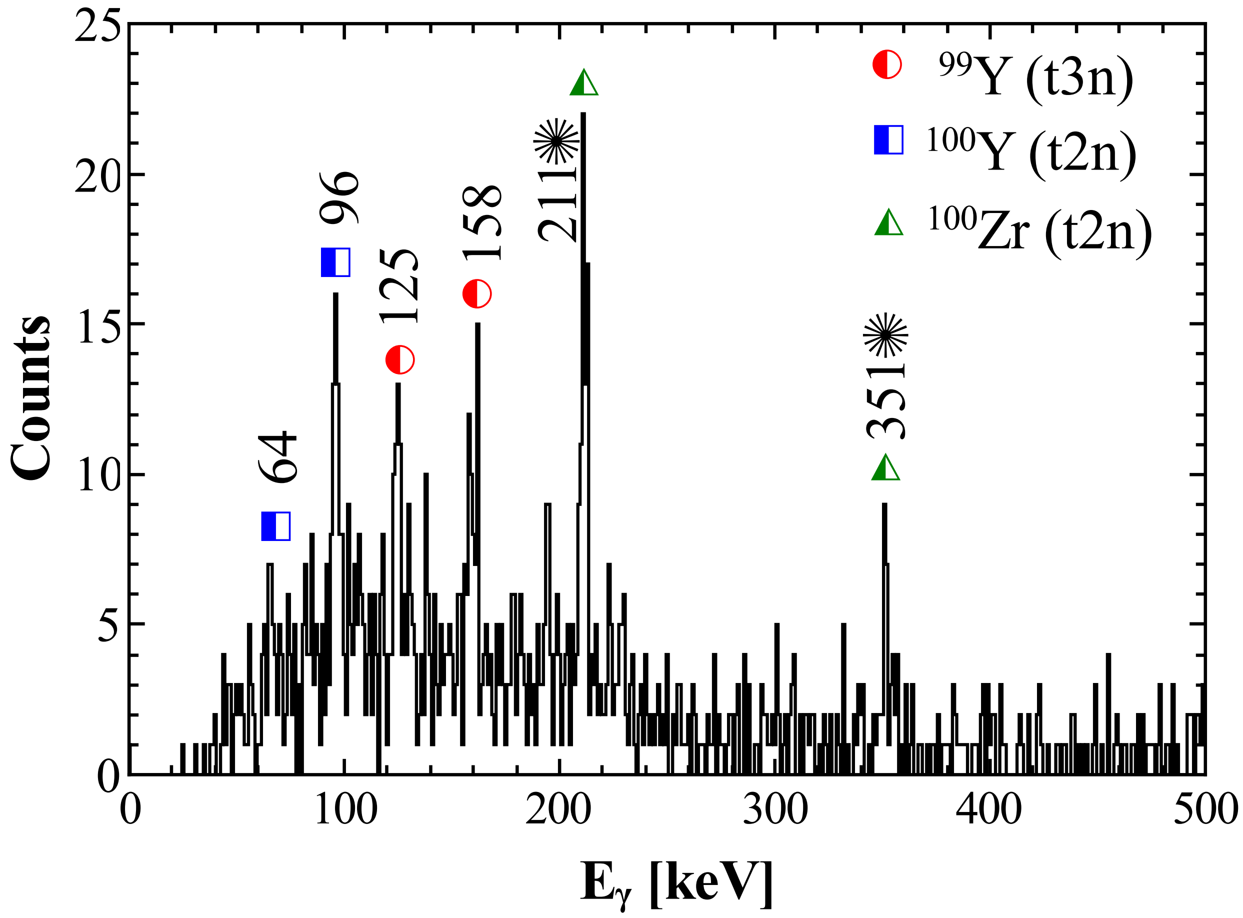

Figure 4.14: *triton*-γ coincidences corresponding to the α-transfer channel. For reactions on the ^{98}Rb beam component, the 3n channel (^{99}Y) is indicated by circles while the 2n channel (^{100}Y) is indicated by squares. γ lines corresponding to reactions on the ^{98}Sr beam component are labelled with a star and the 2n channel (^{100}Zr) is indicated by triangles.

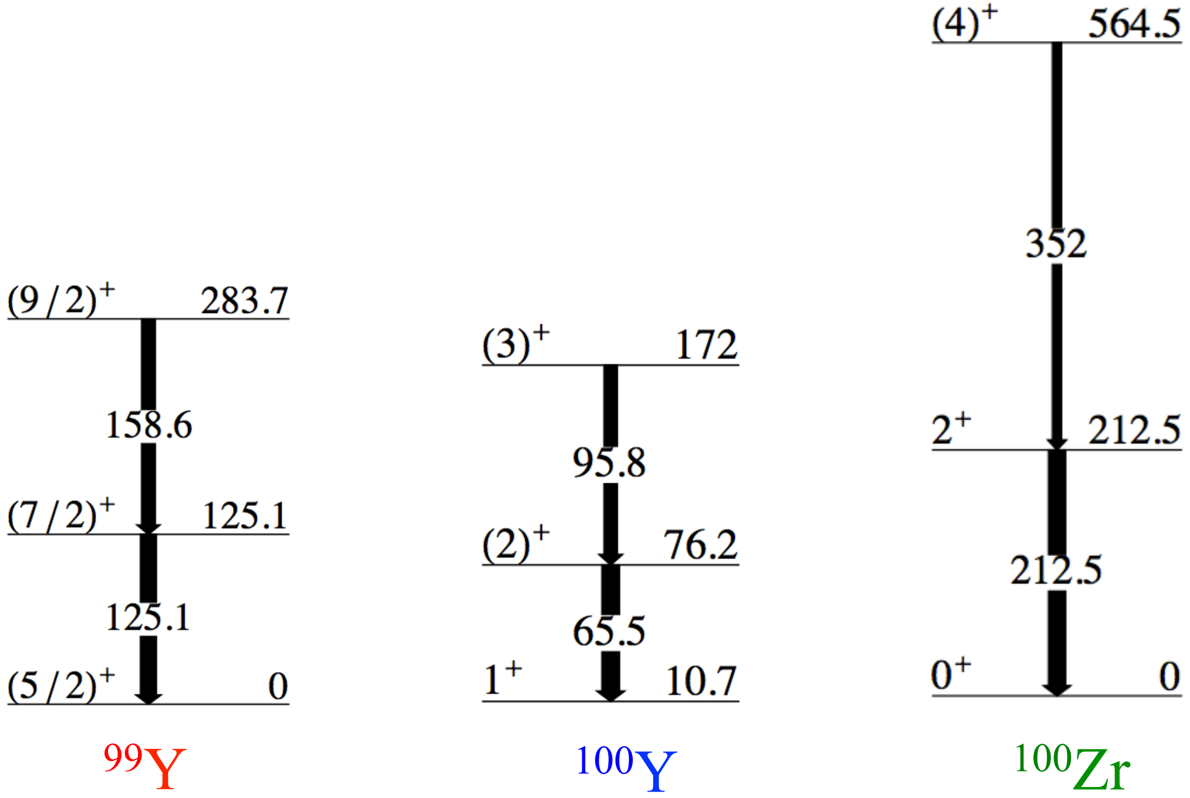

Figure 4.15: Level schemes built on the basis of the γ detected in the triton-γ spectra corresponding to the α-transfer channel (cf. Fig. 4.14) .

Beam	**Product**	**n-evap.**	$\mathbf{I}_i^\pi \rightarrow \mathbf{I}_f^\pi$	**E$_\gamma$ [keV]**	α	**I$_\gamma$ [%]**
^{98}Rb	^{98}Sr	3	$2^+ \rightarrow 0^+$	144.2	0.268	100 (17)
			$4^+ \rightarrow 2^+$	289.3	0.022	60.3 (18)
			$6^+ \rightarrow 4^+$	433.2	0.006	24.3 (73)
	^{99}Sr	2	$(5/2^+) \rightarrow 3/2^+$	90.8	0.248	100 (25)
^{98}Sr	^{99}Y	2	$(7/2^+) \rightarrow (5/2^+)$	125.1	0.180	100 (10)
			$(9/2^+) \rightarrow (7/2^+)$	158.6	0.052	51.3 (50)
			$(11/2^+) \rightarrow (9/2^+)$	198.5	0.088	26.6 (36)
			$(13/2^+) \rightarrow (11/2^+)$	223.9	0.021	24.7 (25)

Table 4.3: Nuclei produced in triton-transfer reactions and identified according to their known γ transitions. Relative intensities of the γ transitions, normalized to the ground state transition, are reported as measured in this experiment. Spins, parities and conversion coefficients are taken from the literature [55].

Beam	**Product**	**n-evap.**	$\mathbf{I}_i^\pi \rightarrow \mathbf{I}_f^\pi$	**E$_\gamma$ [keV]**	α	**I$_\gamma$ [%]**
^{98}Rb	^{99}Y	3	$(7/2^+) \rightarrow (5/2^+)$	125.1	0.180	100 (15)
			$(9/2^+) \rightarrow (7/2^+)$	158.6	0.052	86.1 (32)
	^{100}Y	2	$(2^+) \rightarrow 1^+$	65.5	0.62	100 (40)
			$(3^+) \rightarrow (2^+)$	95.8		74.5 (55)
^{98}Sr	^{100}Zr	2	$2^+ \rightarrow 0^+$	212.5	0.072	100 (17)
			$(4^+) \rightarrow 2^+$	352	0.052	51.8 (20)

Table 4.4: Nuclei produced in α-transfer reactions and identified according to their known γ transitions. Relative intensities of the γ transitions, normalized to the ground state transition, are reported as measured in this experiment. Spins, parities and conversion coefficients are taken from the literature [55].

Measured γ transitions, reported in Tab. 4.3 and Tab. 4.4, are strictly related to the decay path of the nuclei after the transfer. As it will be discussed in Sec. 4.6.1, cluster-transfer took place at high excitation energy, in different regions of the energy-spin phase space, above the neutron threshold. Therefore, the final products firstly decay by neutron emission and then by γ cascades. Such a decay is governed by the level density above the neutron separation energy, the neutron separation energies and the discrete structure of the residues. The neutron separation energies of the nuclei after the transfer are reported in Tab. 4.5.

Although the population of non-yrast high energy states was one of the main goal of this experiment, the final, poor, statistics didn't allow to observe them, mainly due to the fragmentation of the γ decay at high excitation energy. It may be also speculated that the non observation of low-lying off-yrast states could indicate that the decay path reaches the yrast band at medium-high energies.

Beam	**t-transfer**	**α-transfer**
^{98}**Rb**	$S_n(^{101}Sr)$ = 3.259 MeV	$S_n(^{102}Y)$ = 5.051 MeV
	$S_{2n}(^{101}Sr)$ = 9.433 MeV	$S_{2n}(^{102}Y)$ = 10.740 MeV
	$S_{3n}(^{101}Sr)$ = 13.292 MeV	$S_{3n}(^{102}Y)$ = 15.903 MeV
^{98}**Sr**	$S_n(^{101}Y)$ = 5.685 MeV	$S_n(^{102}Zr)$ = 6.356 MeV
	$S_{2n}(^{101}Y)$ = 10.853 MeV	$S_{2n}(^{102}Zr)$ = 11.280 MeV
	$S_{3n}(^{101}Y)$ = 16.674 MeV	$S_{3n}(^{102}Zr)$ = 18.186 MeV

Table 4.5: Neutron separation energies of the nuclei produced in the triton-transfer process on ^{98}Rb (^{101}Sr) and ^{98}Sr (^{101}Y) and in the α-transfer process on ^{98}Rb (^{102}Y) and ^{98}Sr (^{102}Zr).

4.6.1 Neutron evaporation

In the previous section, it was mentioned that different distribution of the residues were measured for reactions on ^{98}Rb and ^{98}Sr beam components and for triton- and α transfer. In this section, the neutron evaporation as a function of i) excitation energy of the projectile-like system and ii) spin distribution will be discussed.

i) *Dependence on excitation energy*: the excitation energy of the final system was determined by reconstructing the two-body kinematics through detected tritons and α-particles (see App. A for details). Due to the poor statistics collected in the α-transfer channel, only the triton-transfer will be discussed.
The energies of the detected α-particles correspond to an excitation energy of the recoil system between $\approx$ 16 MeV and $\approx$ 22 MeV for the reaction on ^{98}Rb and between $\approx$ 13 MeV and $\approx$ 19 MeV in the case of ^{98}Sr beam component. Fig. 4.16 shows α energies as a function of the scattering angle, as measured in this experiment. In the same plot, three different kinematic lines corresponding to different excitation energies, are also shown.

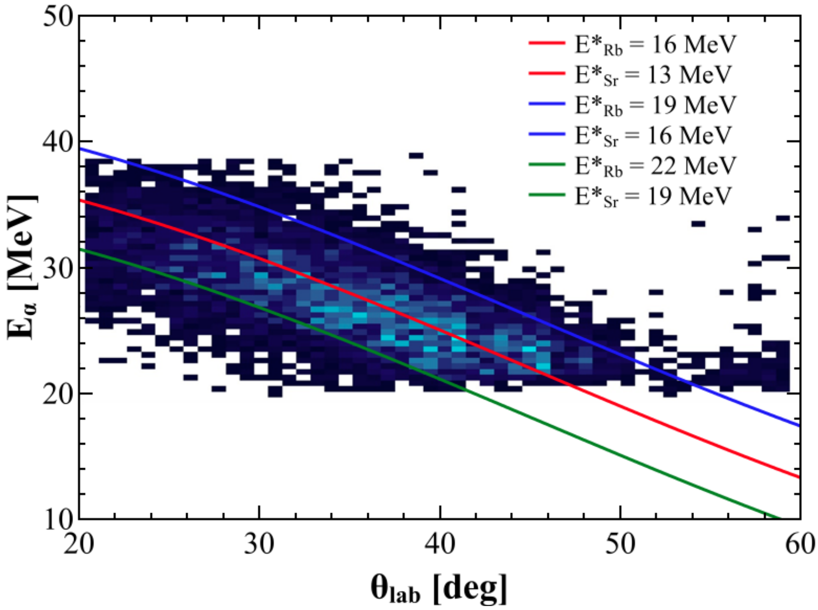

Figure 4.16: α energy as a function of the scattering angle, as measured in this experiment, corresponding to the triton-transfer channel. Three kinematic line are shown, corresponding to three different excitation energies (16, 19 and 22 MeV in the case of reaction on ^{98}Rb and 13, 16 and 19 MeV in the case of the ^{98}Sr beam component.

First of all, by comparing the excitation energies of the projectile-like systems after the transfer with the neutron separation energies of Tab: 4.5, the difference between reactions on ^{98}Rb and ^{98}Sr beam components in terms of final residues can be understood. If fact, in the case of ^{98}Rb, the average excitation energy of the final system (^{101}Sr) is 19 MeV which explains that the evaporation up to 3 neutrons was observed, being $S_{3n}(^{101}\text{Sr})$ = 13.292 MeV. On the contrary, for ^{98}Sr, the average excitation energy of ^{101}Y is 16 MeV while $S_{3n}(^{101}\text{Sr})$ = 16.674 MeV. This may justify the absence of the 3n channel in this case.

The γ spectra measured in coincidence with the previous kinematic lines allowed to extract information about neutron evaporation as a function of the excitation energies of the projectile-like nuclei. By studying the evolution of the γ yield corresponding to different isotopes, associated to a different number of evaporated neutrons, it was possible to test the selectivity on the residues with the excitation energy of the system. The γ spectra are presented in Fig. 4.17 where the counts were normalized to take into account the different areas of the cuts around the kinematic lines shown in Fig. 4.16.

In the case of the ^{98}Rb beam, the percentage of 2-neutron evaporation decreases as the excitation energy increases, as it can be seen in Fig. 4.17 by looking at the 90.8 keV γ-line corresponding to ^{99}Sr. The flux is moved towards the 3-neutron channel, whose strength increases along with the excitation energy, as indicated by the 144.2 keV transition in the same figure corresponding to ^{98}Sr . On the other hand, in the case of the ^{98}Sr beam it can be noticed that the only the 2-neutron evaporation channel is observed with a maximum yield for intermediate energies, as shown by the 125.1 keV transition of ^{99}Y in Fig. 4.17. The 3-neutron channel is expected to be present also in this case at the highest excitation energy. Nevertheless, the final nucleus would be ^{98}Y which has a 0.9 μs isomer at 170 keV which collects most of the decay flux, preventing the detection of prompt γ-rays. A summary of the total normalized strength is presented in Fig. 4.18 for reactions on ^{98}Rb and in Fig. 4.19 in the case of the ^{98}Sr beam. Similar results can be obtained in the case of α-transfer although the poorer statistics didn't allow to perform a reliable analysis. In particular, it is possible to observe also in this case a dependence on the gamma yield as a function of the excitation energy although no values were deduced due to limited statistics.

This analysis provides a useful tool to investigate the final products of the reaction, according to the yield of detected γ-rays as a function of excitation energy. This result may help in future experiments where new γ transitions have to be assigned to different isotopes populated within the same cluster-transfer channel.

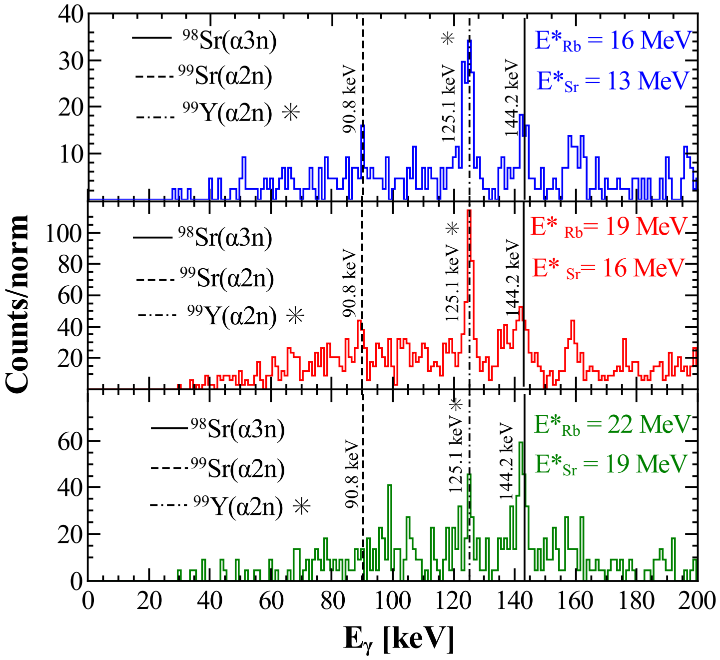

Figure 4.17: γ spectra in coincidence with α-particles and corresponding to different recoil excitation energies. The spectra are normalized according to the different areas of the applied kinematic cuts (see Fig. 4.16 and text for details). Top panel: E*= 16 MeV for reaction on ^{98}Rb and E*= 13 MeV for ^{98}Sr case. Central panel: E*= 19 MeV for reaction on ^{98}Rb and E*= 16 MeV for the ^{98}Sr case. Bottom panel: E*= 22 MeV for reaction on ^{98}Rb and E*= 19 MeV for ^{98}Sr case.

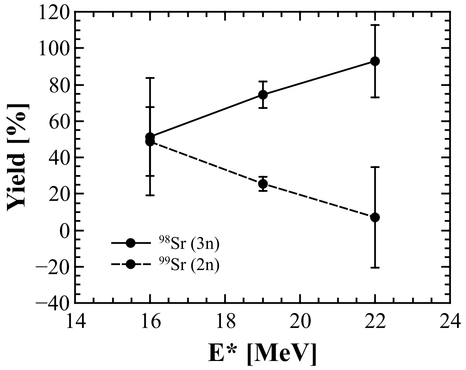

Figure 4.18: γ yield, normalized to the total yield for each E*, for triton-transfer reactions on the ^{98}Rb beam, as a function of excitation energy of the final system.

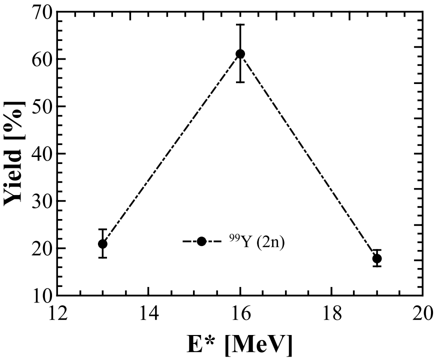

Figure 4.19: γ yield, normalized to the total yield, for triton-transfer reactions on the ^{98}Sr beam, as a function of excitation energy of final system.

ii) *Dependence on the spin distribution*: a further analysis was performed by studying the measured yields as a function of different spin distributions, for both triton and α- transfer, via a comparison with simulations. In this case, the relative percentage of evaporated neutrons was investigated for recoil excitation energies corresponding to the maximum of the experimental energy distribution only. In the case of triton transfer, this corresponds to the red line in Fig. 4.16 (E^*= 19 MeV for reactions on ^{98}Rb and E^*= 16 MeV in the ^{98}Sr case). For α-transfer, E^* = 18 MeV was considered for reaction on ^{98}Rb while 15 MeV was assumed for ^{98}Sr reaction, as shown in Fig. 4.20.

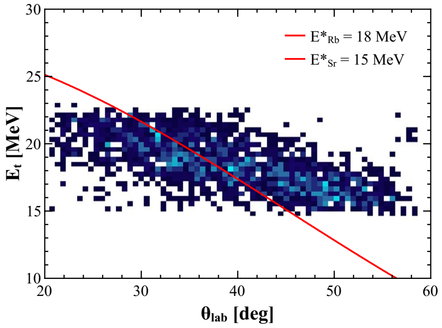

Figure 4.20: Triton energy as a function of the scattering angle, as measured in this experiment, corresponding to the α-transfer channel. The red line corresponds to E^* = 18 MeV for reaction on ^{98}Rb and E^* = 16 MeV for the ^{98}Sr beam.

Experimental data, shown by symbols in Fig. 4.21, were compared with theoretical predictions calculated with the CASCADE code [73]. For this purpose, the particle decay of nuclei produced after the cluster-transfer was simulated as a function of different spin distributions. As a starting point, the excitation energies measured in the experiment were assumed. For the level density, the back-shifted Fermi gas model with a standard level density parameter a_0 = A/8 MeV^{-1} was used, being A the mass of the nucleus. Details of the model can be found in App. C. Although such a model should be carefully used in connection with neutron-rich nuclei, because of the uncertainties on masses and level densities, it turned out to be rather successful in describing the experimental results.

Three different spin distributions were considered, centred in 15, 20 and 25 $\hbar$, and the results are shown by lines in Fig. 4.21. First of all, it should be noticed that only neutrons are predicted to evaporate, as one could expect in exotic neutron-rich nuclei. Furthermore, as it can be seen in the picture, triton-transfer data are well reproduced by a spin distribution centred in 20 $\hbar$ for both reactions on ^{98}Rb and ^{98}Sr beam components. On the contrary, the α-transfer data seem to be better reproduced by a spin distribution centred in 15 $\hbar$, even though the quality of the data is poorer due to the lack of statistics.

These results point out that spins around 15-20 $\hbar$ are actually expected in the final products of cluster-transfer reactions. This fact, together with the measured excitation energies, confirms that cluster-transfer reactions are a possible mechanism to populate states in neutron-rich nuclei at medium-high energy and spin.

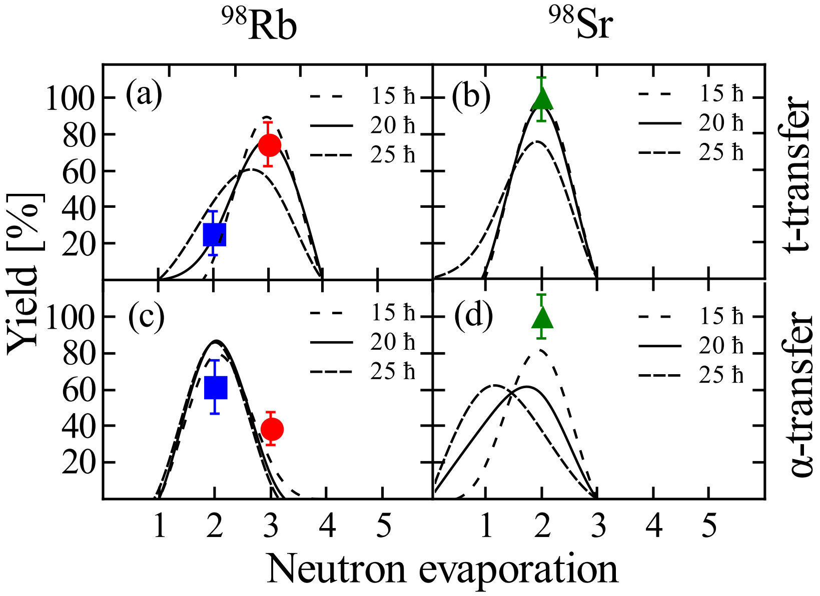

Figure 4.21: Experimental yield of neutron evaporation for both triton- and α- transfer on both ^{98}Rb and ^{98}Sr beam component compared with CASCADE predictions as a function of different spin distributions. Panels (a) and (b) show the experimental data corresponding to triton-transfer while panels (c) and (d) show that the best fit for α-transfer channels (see text for details).

It must be noticed that residues distributions measured in this experiment is strongly influenced by the neutron binding energies of this exotic neutron-rich systems. As a matter of fact, while Q_{gg} keeps almost constant (high and positive) along a given isotopic chain, ensuring high excitation energy in the cluster-transfer process, neutron binding energies change as a function of N/Z, modifying the distribution of the residues. This means that going towards the valley of stability, the number of neutrons evaporated decreases and discrete states can be directly populated by cluster-transfer. Therefore, the picture of cluster-transfer reactions in connection with γ-spectroscopy may change as the system changes.

4.6.2 Beam composition estimation using cluster-transfer channels

Cluster-transfer reactions were also used to estimate the beam composition. The identification of γ-rays detected in coincidence with tritons and α-particles allowed to determine the relative percentage of ^{98}Rb and ^{98}Sr beam components in the beam, by comparing the yields of the channels observed in the two cases, assuming that the cross sections are the same.

The total γ-strength was deduced by looking at the counts in the ground state transitions, which collect all the measured decay flux, properly corrected for detection efficiency and internal conversion. In particular, in the case of trition transfer, the 144.2 keV (^{98}Sr) and 90.8 keV (^{99}Sr) transitions (^{98}Rb beam) and the 125.1 keV γ-line in ^{99}Y (^{98}Sr beam) were used. In the case of α-transfer, by the reference transitions were the 125.1 keV (^{99}Y) and the 65.5 keV (^{100}Y) lines (^{98}Rb beam) and the 212.5 keV transition in ^{100}Zr (^{98}Sr beam). The results are summarized in Tab. 4.6. As it can be argued, this corresponds to an average ratio ^{98}Rb/^{98}Sr = 2/3.

Beam	**t-transfer**	**α-transfer**
^{98}Rb	40(7)	42(8)
^{98}Sr	60(7)	58(8)

Table 4.6: Percentage of ^{98}Rb and ^{98}Sr beam components deduced by comparing the yields of the cluster-transfer channels observed in the two cases, assuming that the cross sections are the same (see text for details).

4.7 Cluster-transfer: cross sections experimental results

Cluster-transfer cross sections were qualitatively studied, experimentally, in terms of i) excitation energy of the final system and ii) angular distribution. Due to the similar reaction dynamics, also in this case ^{98}Rb and ^{98}Sr data were considered as a unique set (see Sec. 4.1) and the analysis was performed assuming ^{98}Rb only as a beam. The results were then interpreted within a model of a direct transfer of a cluster-like particle using a DWBA approximation and two different approaches to describe the wave function of the final states. Such a comparison will be presented in the following section.

i) *Excitation energy*: the excitation energy distribution of projectile-like nuclei, produced in both the triton- and α-transfer processes, were determined by reconstructing the two-body kinematics using energies and angles of the complementary emitted charged particle (α and trition, respectively) measured in the CD Si detector. Details of the used equations can be found in App. B. The results are shown in Fig. 4.22 and Fig. 4.23 for the triton- and α-transfer case, respectively.

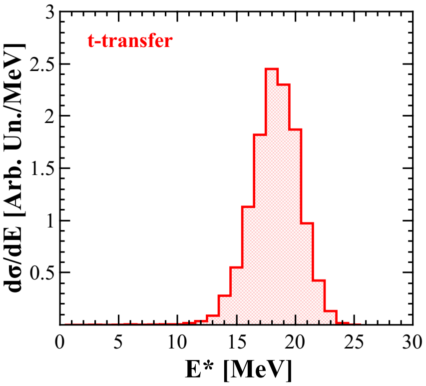

Figure 4.22: Experimental differential cross section as a function of excitation energy for the triton-transfer channel.

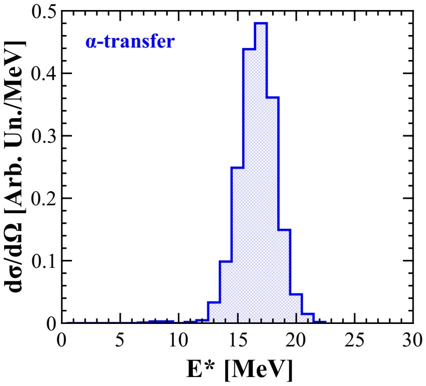

Figure 4.23: Experimental differential cross section as a function of excitation energy for the α-transfer channel.

As shown in the pictures, in the case of both triton- and α-transfer the distributions exhibit a well defined peak at 18 MeV in the first case and at 17 MeV in the second one, indicating that most of the cross section is concentrated in a narrow energy window ($\approx$ 5 MeV) at high excitation energy. The width of the distributions is much larger than the intrinsic energy resolution of the Si detector ($\approx$ 50 keV measured with the α source and $\approx$ 1.5 MeV typically measured in beam [74]) and takes into account the large number of states available in the final system. In particular, the latter lie in the continuum with respect to the core-cluster separation energy and the contributions of each of them can not be separated. In Tab. 4.7 measured excitation energy and the ^{98}Rb-core-cluster separation energies $S_{\text{core-cluster}}$ are reported.

ii) *Angular distribution*: the annular segmentation of the Si detector allowed to extract differential cross sections of the particles emitted in the cluster-transfer reaction channels. Despite that 16 rings were available in the setup, only few rings could be used.

	^{98}**Rb-t**	^{98}**Rb-α**
E* [MeV]	12 - 24	12 - 21
$S_{\text{core-cluster}}$ [MeV]	16	10

Table 4.7: Excitation energies measured in this experiment and core-cluster separation energies for ^{98}Rb-core+t and ^{98}Rb-core+α systems (triton- and α- transfer, respectively).

In fact, those particle scattered at angles corresponding to the outermost rings, having lower energies, didn't punch through the first layer of the detector and they could not be identified. In the case of α-transfer, tritons were emitted with smaller energies than α particles, as it can be seen in Fig. 4.16, Fig. 4.20 and Fig. 3.5 but, thanks to the smaller Z, more rings at larger angles could be used to identify tritons. The experimental angular distributions corrected for the detection efficiency and normalized according to the S scaling factor (see Sec. 4.1.1) are presented in Fig. 4.24.

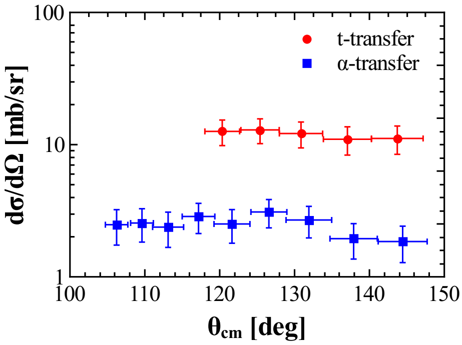

Figure 4.24: Experimental differential cross sections for triton- and α-transfer (red dots and blue squares).

Integrated cross sections were determined by considering the same angles in both tritionand α-transfer. It was found, in the angular range $120° < \theta_{\text{cm}} < 146°$,

$$\sigma_{\text{t-transfer}} = 26.6(7) \quad \text{mb} \tag{4.11}$$

$$\sigma_{\alpha\text{-transfer}} = 5.3(2) \quad \text{mb} \tag{4.12}$$

therefore $\sigma_t/\sigma_\alpha \approx 5$. This value is consistent with experiments performed in direct kinematics [13]. It's worth noticing that one of the reasons of the smaller cross section for the α-transfer case with respect to the triton-transfer reactions is partially a consequence of the Coulomb barrier, which is larger in the former case.

4.8 Cluster-transfer: cross sections theoretical interpretation

Triton- and α-transfer cross sections were qualitatively interpreted within the framework of a direct transfer of a cluster-like particle, using a 1-step DWBA approximation. A detailed description of the theory behind the calculations is discussed in Chap. 1.

The aim of this cross section analysis is not to provide absolute cross sections for the cluster-transfer process, but to supply a qualitative description of the reaction mechanism in terms of excitation energy distributions and relative cross sections.

The direct transfer of a cluster-like particle is not the only approach that can be used for the description of the reactions involving weakly-bound systems. In fact, they are often called incomplete-fusions or breakup-fusions reactions. In this picture, the process is described within a three-body classical dynamical model, assuming the combination of a fast direct process, such as the break-up of the weakly bound nucleus with the cluster structure, followed by the fusion of one of the two fragments, a slow process compared with the previous one and treated statistically [75,76].

In this work, the direct transfer approach was preferred to the break-up fusion, in order to be consistent with the two-body description of the reaction mechanism, which is the assumption used in the analysis of the data.

The calculations were performed with the FRESCO code [34], after providing the scattering potentials, a form factor evaluation based on a description of the wave functions of the initial and final states and a representation of the interaction.

The ^{7}Li ground state wave function was determined by using a cluster model, as described in Sec. 1.3.7. Shell model quantum numbers for the ground state configuration were translated into cluster model quantum numbers using Eq. 1.49, considering an α-core+t system. According to the shell model structure, the ground state configuration of ^{7}Li (with respect to an α-core - see Fig. 4.25 left) is given by

$$J^{\pi} = [(\pi \mathrm{p}_{3/2}) \otimes (\nu \mathrm{p}_{3/2})^{2}] = 3/2^{-} \tag{4.13}$$

The number of nodes N and the orbital angular momentum of the state L for the cluster model wave function are related by (see Eq. 1.49)

$$2N + L = 5 \tag{4.14}$$

Assuming a 0^{+} α-core and taking into account the intrinsic $1/2^{+}$ spin of the triton and $J^{\pi} = 3/2^{-}$ of the ^{7}Li ground state, the possible L- values are restricted to the odd ones because of the parity.

Therefore, by taking as a ground state the lowest possible angular momentum, i.e. $L = 1$, the number of nodes becomes $N = 2$.
A schematic representation of the shell structure and of the cluster model for ^{7}Li ground state is presented in Fig. 4.25.

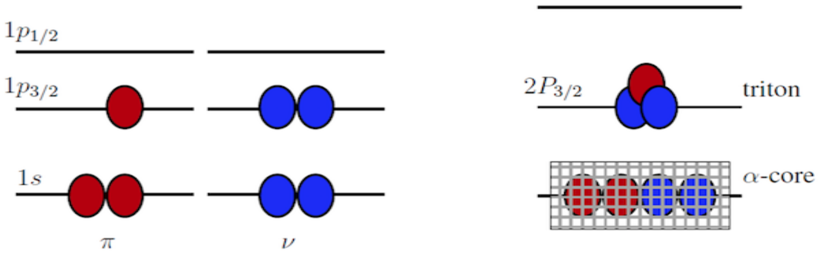

Figure 4.25: Left: shell structure of the ^{7}Li ground state. Right: cluster structure of ^{7}Li ground state assuming an α-core+t system. Cluster model quantum numbers are related to shell model ones as explained in the text.

A Gaussian interaction was used as a mean field nuclear potential binding the α-core+t system which well describes ^{7}Li cluster structure. On top of the Volume term, also a Spin Orbit term was considered [77]

$$V^{\rm nucl}_{\alpha-{\rm t}}(r) = -V_0 e^{-\left(\frac{r-r_0}{a_0}\right)^2} - \frac{1}{r}\frac{\rm d}{{\rm d}r}\left(-V_{\rm so} e^{-\left(\frac{r-r_{\rm so}}{a_{\rm so}}\right)^2}\right) \vec{\rm L}\cdot\vec{\rm S} \tag{4.15}$$

Parameters used in Eq. 4.15 are reported in Tab. 4.8

V_0 **[MeV]**	**r$_0$ [fm]**	**a$_0$ [fm]**	**V$_{so}$ [MeV]**	**r$_{so}$ [fm]**	**a$_{so}$ [fm]**
83.78	0	2.520	2.006	0	2.520

Table 4.8: Parameters used in Eq. 4.15 to describe the Gaussian α-core+t binding potential of ^{7}Li, including a Volume and a Spin Orbit term [77].

The Coulomb radius is defined by

$$R_{\rm C} = r_{0\rm C} A_{\alpha}^{1/3} \tag{4.16}$$

being $\mathrm{r}_{0\mathrm{C}}$ = 1.950 fm and A_α = 4. The same description was used for both triton- and α-transfer.

The description of the exit channel is more complicated. The wave functions of the final states has to take into account the high excitation energy of the final system, as measured in this experiment (see Sec. 4.7). Both systems ^{98}Rb-core+t and ^{98}Rb-core+α (triton- and α- transfer respectively) have final states lying above the core-cluster separation energies (see Tab. 4.7). In order to take this aspect into account, two different approaches were used. In the first case, a weakly bound approximation was exploited and the results will be presented in Sec. 4.8.1. In the second case, a proper description of the continuum was given. The results will be described in Sec. 4.8.2. In both cases, the states were described assuming a Wood-Saxon mean field potential. It is important to note that in this model, the final states of the core-cluster systems were described assuming an inert core in the ground state. Finally, a cluster spectroscopic factor $S_F^{cluster} = 1$ was considered, both for the initial and final states. This is a reasonable assumption in a qualitative description of the cluster-transfer process.

To properly describe the scattering in the entrance and exit channels, as well as the interaction responsible of the transfer, different potentials were used. A sketch of the reaction in the case of triton-transfer is shown in Fig. 4.26.

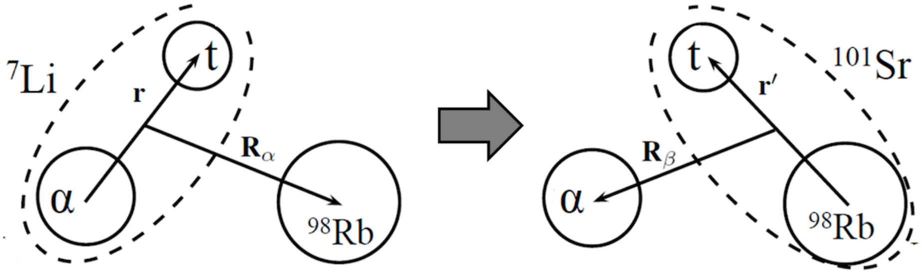

Figure 4.26: Sketch of the reaction ^{98}Rb+^{7}Li = ^{101}Sr + α corresponding to the triton-transfer channel.

The nuclear part of the scattering optical potentials, both in the entrance and exit channels, were assumed to be of Woods-Saxon shape with volume terms only (see Sec: 1.3.2. For the entrance channel, the optical potential tested in the elastic case was used (see Sec. 4.1. For the exit channels, the parameters presented in Tab. 4.9 were fitted on experimental data of this work, to better reproduce angular distributions and excitation energies.

Channel	V(MeV)	r_V(fm)	a_V(fm)	W(MeV)	r_W(fm)	a_W(fm)	R_C(fm)
α + ^{101}**Sr**	140.0	1.200	1.200	10.0	1.200	1.200	6.054
t + ^{102}**Y**	80.0	1.250	1.500	10.0	1.250	1.500	6.074

Table 4.9: Wood-Saxon optical parameters for outgoing *triton*- and α- transfer channels (α + ^{101}Sr and triton + ^{102}Y), obtained by fitting the experimental data of this work. V, r_V and a_V are the real depth, radius and diffuseness while W, r_W and a_W are the imaginary depth, radius and diffuseness. R_C is the Coulomb radius.

For the interaction potential, both the *prior* and *post* representations were initially considered (see Chap. 1), although the calculations were eventually performed by using the *post* representation only . As an example, the following interactions are reported in the case of triton-transfer as presented in Fig. 4.26.

$$V_{\text{int}}^{\text{prior}} = V_{\text{Rb}-\text{t}} + [U_{\text{Rb}-\alpha} - U_{\text{Rb}-\text{Li}}] \tag{4.17}$$

$$V_{\text{int}}^{\text{post}} = V_{\alpha-\text{t}} + [U_{\text{Rb}-\alpha} - U_{\text{Sr}-\alpha}] \tag{4.18}$$

As it can be seen in the previous expressions, the *post* interaction contains the well known α-triton potential (Eq. 4.15) and the difference of the remnant terms is basically zero. In the case of the *prior* interaction, the main term is the potential between ^{98}Rb and triton, whose expression is not known precisely. Furthermore, the difference of the remnant terms is far from being zero. For these reasons, the post representation was finally assumed, without considering the contributions of the remnants terms

$$V_{\text{int}}^{\text{post}} \approx V_{\alpha-\text{t}} \tag{4.19}$$

Such an assumption also allowed to use the same interaction in the α-transfer channel, where the post representation reduces to the same expression. Finally, this choice is also consistent with the DWBA approximation used in the calculations, since $V_{\alpha-\text{t}}$ is rather small compared to the elastic potential, and it can be treated as a perturbation. This effect can be seen in Fig. 4.27, where the volume terms of the elastic potential U_{elastic} (see Tab. 4.1) and the interaction potential V_{int} (see Tab. 4.8) are shown. It can be noticed that $V_{\text{int}} \ll U_{\text{elastic}}$ at the surface, where V_{int} plays a role, being the transfer a peripheral process.

In the following sections the two different approaches for the description of the wave functions of the final states will be presented. In Sec: 4.8.1 the weakly-bound approximation will be illustrated while in Sec. 4.8.2 a proper representation of the states in the continuum will be discussed.

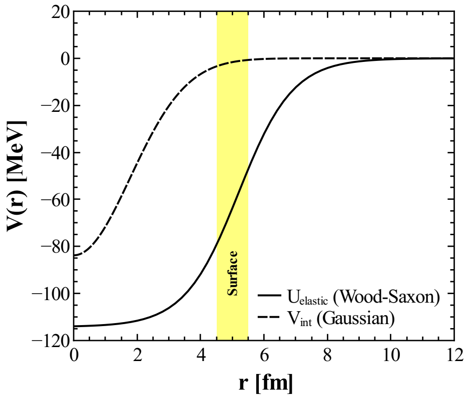

Figure 4.27: Volume terms of the elastic potential $U_{elastic}$ (see Tab. 4.1) and the interaction potential V_{int} (see Tab. 4.8). The yellow shaded area shows the region around the surface where the transfer takes place.

4.8.1 Weakly bound approximation

In the first model, a weakly bound approximation of the final states was used to compute the cross sections. In order to provide a representation of the space, several states with different angular momenta were chosen in a wide energy window, from zero to energies where the cross section becomes negligible above the core-cluster separation energy. The wave functions of the states were treated as if they were all discrete states. In particular, those states above the core-cluster separation energy were assumed to have an energy higher than the separation energy but the core-cluster system was forced to have a positive small binding energy ($\approx$ 0.01 MeV) . In such a way, the radial wave functions still decay to zero for large r, as in the case of discrete states. As anticipated in Sec. 4.8, a Wood-Saxon mean field potential was used as a binding potential. The radial wave functions were determined by solving the Schrödinger equation iteratively changing the potential parameters, until the desired binding energy was achieved. The result of such an approach is to compress the system in terms of density $\rho(\mathrm{r}) = |u(\mathrm{r})|^2$, being $u(\mathrm{r})$ the radial part of the structure wave function. This approximation does not reflect the real core-cluster configuration and it can not provide absolute cross sections.

A set of states with orbital angular momenta between L = 0 and L = 5 at energies from E* = 0 MeV to E* = 25 MeV at steps of 0.5 MeV were considered in the case of triton-transfer. For α-transfer, states up to L = 7 were assumed in the same energy interval.

Firstly, theoretical cross sections were studied as a function of the angular momentum of the final states. The calculations are presented in Fig. 4.28 and Fig. 4.29 for triton- and α-transfer, respectively.

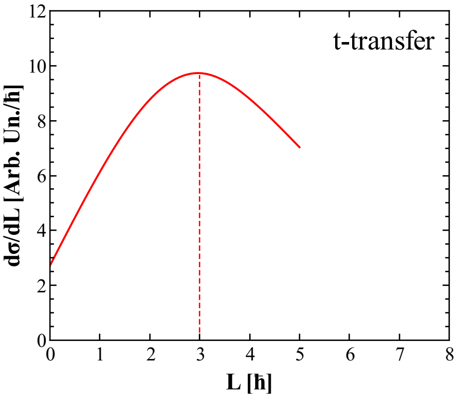

Figure 4.28: Differential cross section as a function of the angular momentum of the final states for the triton-transfer channel, showing a maximum at L=3.

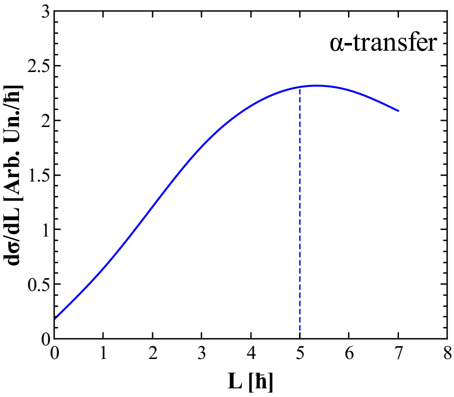

Figure 4.29: Differential cross section as a function of the angular momentum of the final states for the α-transfer channel, showing a maximum at L=5.

As it can be seen, both calculations show a bell-shaped distribution peaked in L = 3 for the triton-transfer and in L=5 in the α-transfer case. In order to compare the two results, the final calculations were performed taking states up to half of the maximum of the two distributions, assuming that they are symmetric around the maximum, as it can be inferred from the pictures. Larger angular momenta were not considered for computational reasons.

It is important to note that, although the strength of the cross section depends on the transferred angular momentum L, the shape of the angular distribution and of the excitation energy does not change with L. This reflects the fact that, in general, multi-nucleon transfer reactions, such as cluster-transfers, are not particular selective in terms of the angular momenta of the initial and final states. This can be seen in Fig. 4.30 and Fig. 4.31, where triton-transfer angular distributions, for a state at 18 MeV, and excitation energies for different values of L are show.

The partial waves used in the calculations were carefully studied in order to ensure the convergence. Partial waves up to ℓ = 40 were finally considered, which resulted to be enough to stop the calculations. Fig. 4.32 shows the absolute value of the S-matrix $|S_\ell|$, as a function of the partial waves in the case of triton-transfer and for states with L = 2. It can be seen that at ℓ = 20 the calculation converges, resulting in $|S_\ell| \rightarrow 1$.

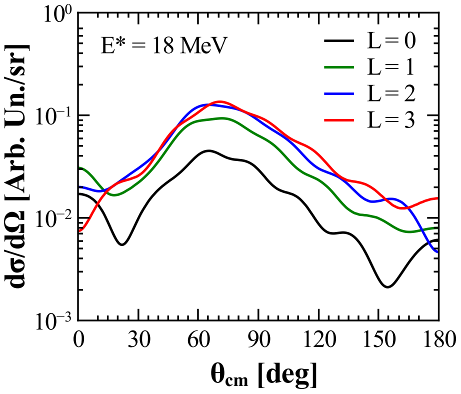

Figure 4.30: Triton-transfer angular distributions for different values of L.

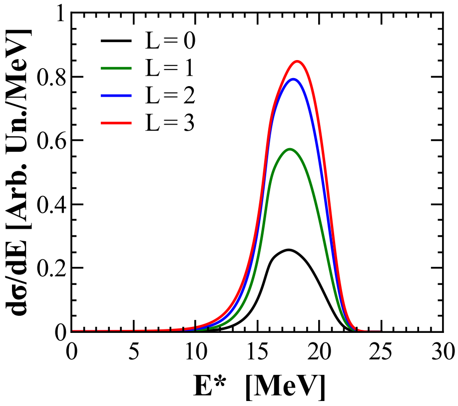

Figure 4.31: Triton-transfer excitation energy distributions for different values of L.

A further check was done considering the absorption cross section σ_{abs} as a function of partial waves, as it is presented in Fig. 4.33, for the trition-transfer channel and for a state with L = 2.

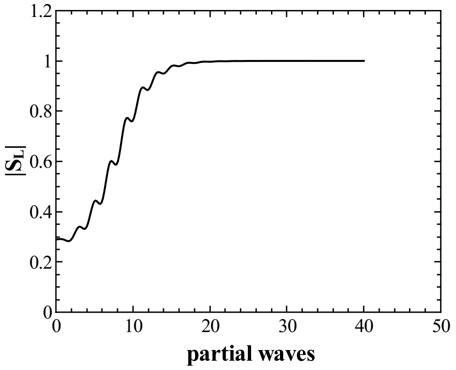

Figure 4.32: Absolute value of the S-matrix as a function of partial waves included in the calculation, in the case of triton-transfer to a L = 2 state.

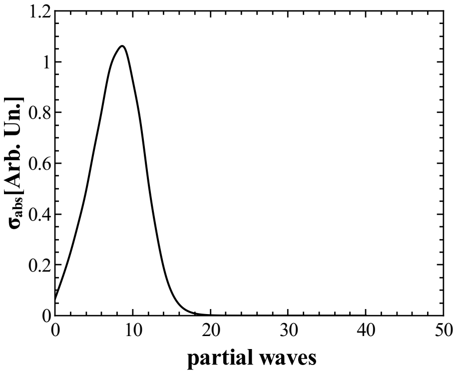

Figure 4.33: Absorption cross section as a function of partial waves included in the calculation, in the case of triton-transfer to a L = 2 state.

Full calculations for triton- and α-transfer were finally performed and the cross sections as a function of the excitation energy of the system after transfer were studied. The results are presented in Fig. 4.34. The experimental distributions were used to tune the parameters of the optical potential in the exit channels, presented in Tab. 4.9. It is important to note that in this case cross sections are given in arbitrary units and therefore the plots show only a qualitative comparison between data and theory.

It can be seen that the experimental energy distributions are well reproduced by the theoretical predictions, in both cases, although in the case of α-transfer, the theoretical calculation at low energy are worse. This effect may be related to the energy difference between the core-cluster separation energy and the maximum of the distribution, which is significantly larger than in the triton-transfer case (8 MeV compared to 2 MeV). As a result, the weakly bound approximation is less justified in the case of α-transfer. In Fig. 4.34, the expected optimum excitation energy according to the optimum Q-value of the reactions, calculated at the leading order (see Eq. 1.62) , is also shown. It can be seen that the semi-classical approach predicts reasonably well the centroid of the distributions. In Tab. 4.10, Q_{gg} and Q_{opt}, calculated according to Eq. 1.62, are reported together with the deduced E^*_{opt} for both the triton- and α-transfer channels.

	t-transfer	**α-transfer**
Q_{gg} [MeV]	13.6	7.6
Q_{opt} [MeV]	-5.1	-10.4
E^*_{opt} [MeV]	18.7	18

Table 4.10: Q-value for the transfer to the ground state Q_{gg}, Q_{opt}, calculated according to Eq. 1.62 and the deduced E^*_{opt} for both the triton- and α-transfer channels.

Angular distributions were also studied to investigate the relative cross sections between triton- and α-transfer. The different contributions to the cross sections originated from states with different angular momentum and with energy corresponding to the maximum of the distributions shown in Fig. 4.34 were considered. It was noticed that the ratio between cross sections was rather sensitive to the ratio between the number of nodes of the wave function in the final mass partition for triton- (N_t) and α-transfer (N_α). To properly reproduce the experimental data, it was found that $N_\alpha=2N_t$ was needed. The results are presented in Fig. 4.35. Theoretical predictions were rescaled (using the same value for both triton- and α transfer) to the experimental data, for which the absolute value was determined according to the S scaling factor (see Eq. 4.5). It can be seen that such a ratio is well reproduced by the theoretical calculations.

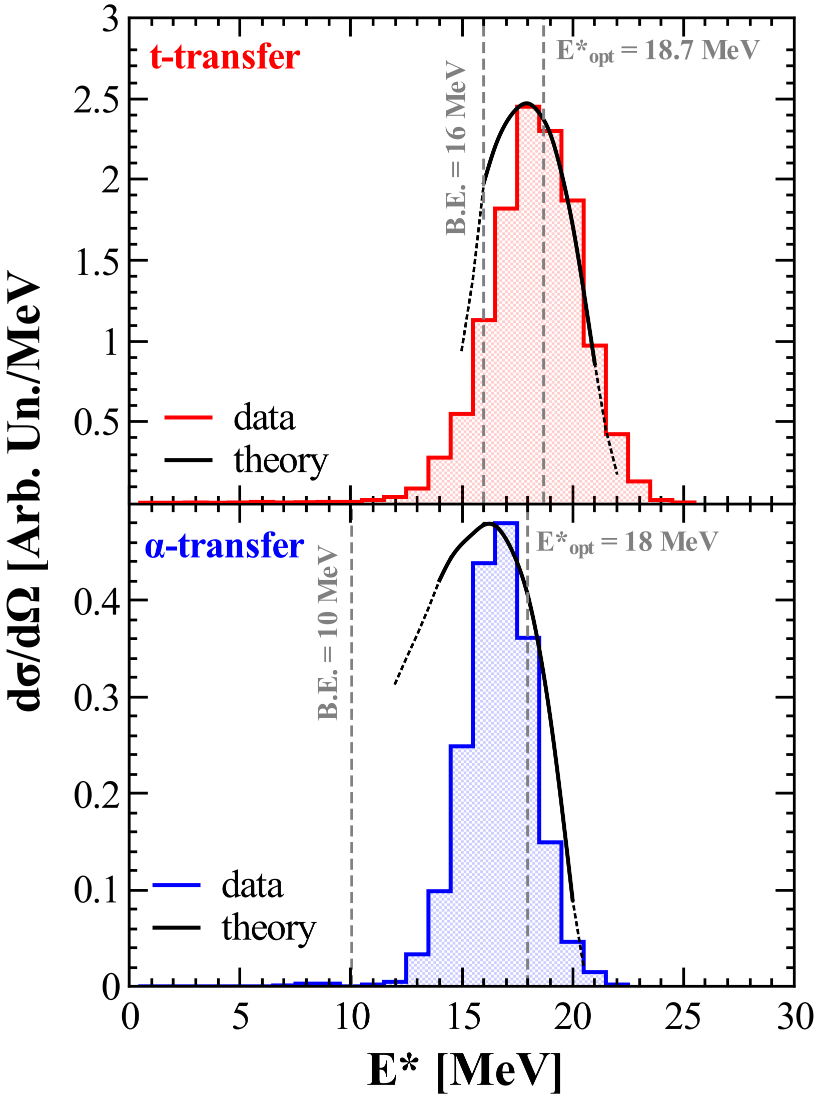

Figure 4.34: Top panel: differential cross section as a function of excitation energy for the *triton*-tranfer channel on ^{98}Rb. The colored area corresponds to the experimental distribution while theoretical calculations are shown as a solid line (see text for details). The triton separation energy is also indicated (S_t= 16 MeV) as well as the expected maximum of excitation energy (E^*_{opt} = 18.7 MeV) deduced from the optimum Q-value. Bottom panel: differential cross section as a function of excitation energy for the α-tranfer channel ^{98}Rb. The colored area corresponds to the experimental distribution while theoretical calculations are shown as a solid line (see text for details). The α separation energy is also indicated (S_α= 10 MeV) as well as the expected maximum of excitation energy (E^*_{opt} = 18 MeV) deduced from optimum Q-value.

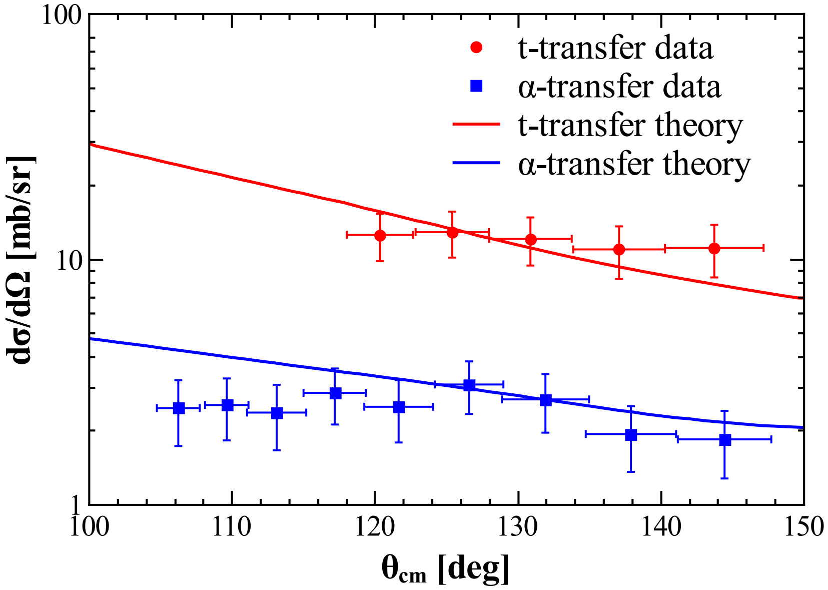

Figure 4.35: Differential cross sections for triton (red)- and α (blue)-transfer. The points correspond to experimental data while solid lines are the calculations performed within the weakly bound approximation model.

The results show that triton- and α-transfer cross sections are qualitatively well described in terms of excitation energy distributions and relative cross sections by the theory, suggesting that such processes might be interpreted within the framework of a direct transfer of a cluster-like particle using a weakly bound approximation for the final states.

4.8.2 Transfer to the continuum

An exploratory approach considering a proper representation of the final states in the continuum with respect to the core-cluster system was also attempted. In order to be consistent with the weakly-bound model, all the parameters involved in the calculations were not changed, except for the description of the wave functions of the final states. The continuum was discretized according to the model presented in Sec. 1.3.8.

In this specific case, for both triton- and α transfer 10 states with angular momenta up to L=5 were considered in an energy window 10 MeV wide above the core-cluster separation energy. Each state was placed in a box with a width Γ_{bins} depending on the energy and was divided into 100 resonant bins. A schematic representation of such a discretization is shown in Fig. 4.36.

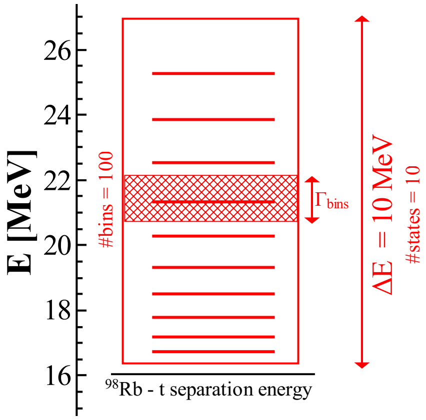

Figure 4.36: Scheme of the discretization of the continuum in the case of triton-transfer. A energy window of 10 MeV above the core-cluster separation energy is assumed and 10 states are considered, each placed in a box with a width depending on the energy and divided into 100 bins each.

The angular momenta of the states and the number of bins were chosen such that the calculation converged. To define the discretization, the cross section as a function of the number of bins and of angular momentum were studied. The results for the triton-transfer case are presented in Fig. 4.37 and Fig. 4.38. It is seen that the cross section converges for a number of bins greater than 60 and keeps constant within a variation of 2.5 %. The number of bins was therefore chosen in correspondence of the average value within such a variation, i.e. 100. Regarding angular momenta, it can be noticed that the total cross section converges as the number of included states increases. In particular, at L = 5 it looks almost flat therefore no further states were included. Similar considerations can be done for the case of α-transfer. Also in this case the convergence of the calculations was checked as a function of the partial waves and similar results were obtained. It was found that L = 40 could be used also in this model, as it can be argued from Fig. 4.39 and Fig. 4.40. The cross section was studied also in this case as a function of excitation energy and the results are presented in Fig. 4.41. First of all, it is important to note that this approach gives discrepancy between experimental data and theoretical calculations (solid lines). In fact, the predicted distributions are shifted about 2.5 MeV to higher energies in the case of triton-transfer while the matching is much better in the α-transfer case. The reason of this discrepancy may be related to the description of the states in the continuum, for which no unique prescription exists.

On the other hand, theoretical angular distributions turn out to reproduce rather well the experimental data. In particular, the number of states included in the calculations seems to be enough to well reproduce the ratio between triton- and α-transfer cross sections, as it can be seen in Fig. 4.42. Also in this case, theoretical cross sections were rescaled on experimental data.

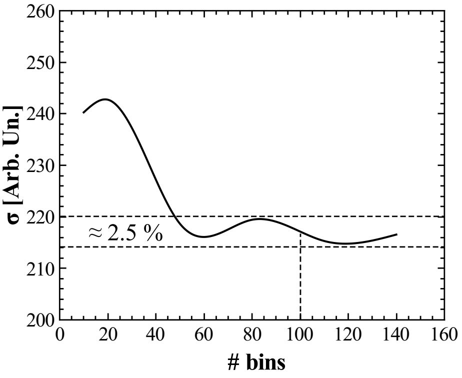

Figure 4.37: Cross section as a function of the number of bins, showing a small variation within 2.5 % after 60 bins, in the case of triton-transfer.

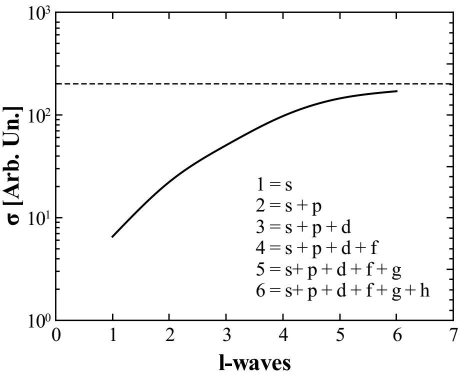

Figure 4.38: Cross section as function the angular momentum of the states included in the calculations showing the convergence at L = 5, in the case of triton-transfer.

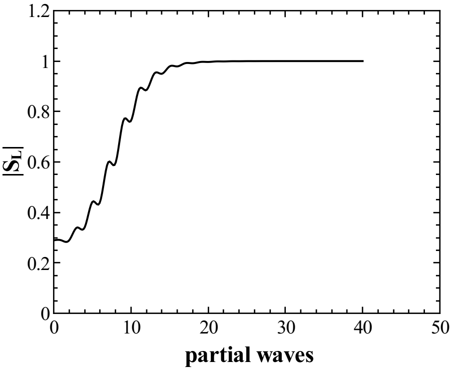

Figure 4.39: Absolute value of the S-matrix as a function of partial waves included in the the calculation, in the case of triton-transfer.

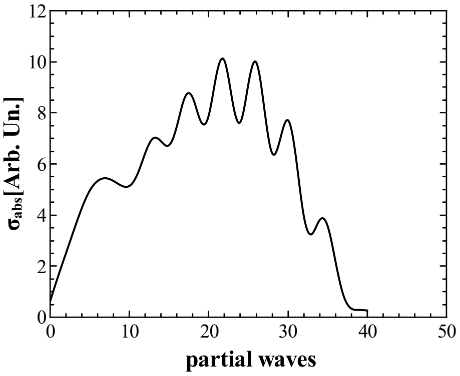

Figure 4.40: Absorption cross section as a function of partial waves included in the calculation, in the case of triton-transfer.

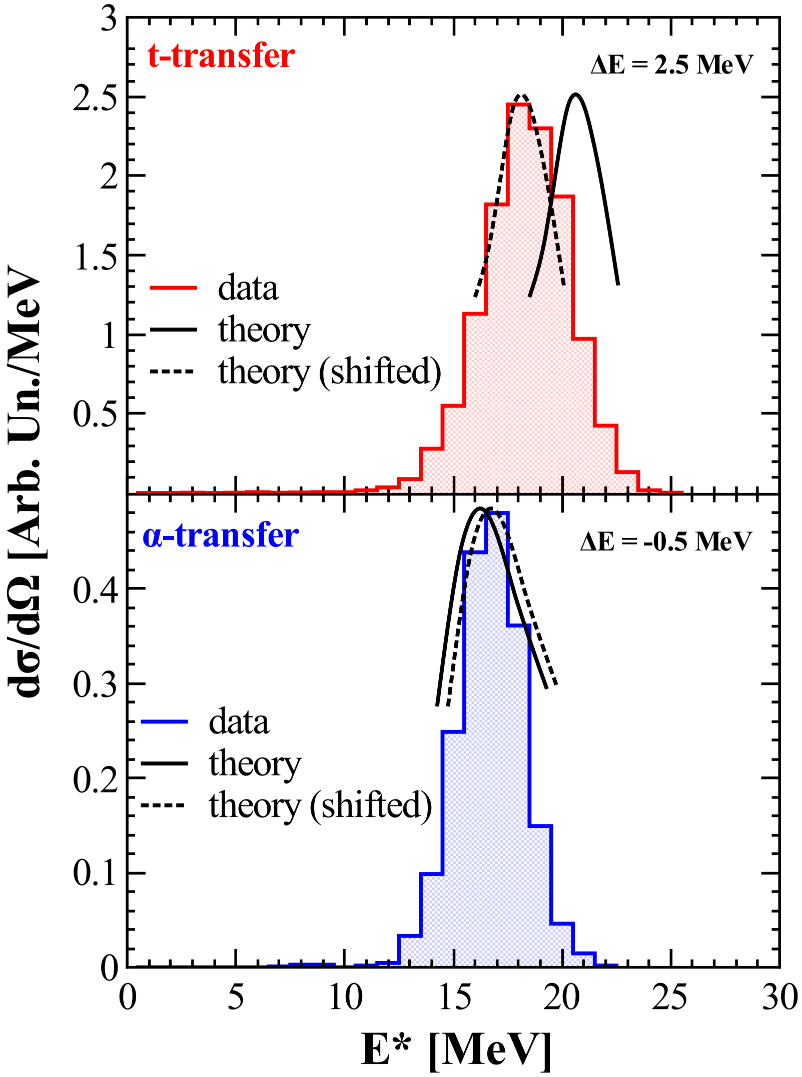

Figure 4.41: Top panel: differential cross section as a function of excitation energy for the triton-tranfer channel on ^{98}Rb. The colored area corresponds to the experimental distribution while theoretical calculations are shown as a solid line (see text for details). The dotted line shows the theoretical prediction shifted by ΔE = 2.5 MeV to match the maximum of the experimental distribution. Bottom: differential cross section as a function of excitation energy for the α-tranfer channel on ^{98}Rb. The colored area corresponds to the experimental distribution while theoretical calculations are shown as a solid line (see text for details). The dotted line shows the theoretical prediction shifted by ΔE = 0.5 MeV to match the maximum of the experimental distribution.

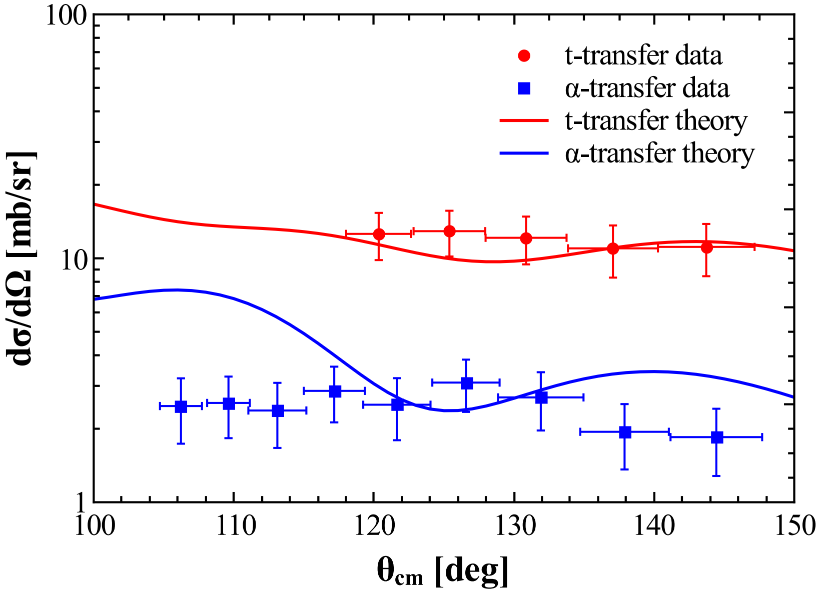

Figure 4.42: Differential cross sections for triton (red)- and α (blue)-transfer. The points correspond to experimental data while solid lines are the calculations performed considering the final states in the continuum.

It should be mentioned that, in this case, the absolute values of the theoretical distribution is much closer to the experimental ones than in the previous approach (see Sec. 4.8.1. In fact, while in the weakly bound model a large scaling factor was used (≈ 200) , in this case only a factor of 3 was needed. This results points out that a proper description of the states in the continuum might be a better approach to determined absolute cross sections, although further studies are needed to clarify the role of the different parameters involved in the calculations, as well as to find out the reasons of the discrepancy observed in the excitation energy spectrum.

4.9 Fusion-evaporation channel

Besides direct reaction channels, fusion-evaporation reactions are also expected to occur with a rather large cross section. Fusion-evaporation reactions induced by neutron-rich radioactive beams are usually difficult to be measured, for two reasons. On one hand, it is not possible to rely on the detection of charged particles. In fact, the decay of exotic neutron-rich nuclei produced in fusion reactions mainly take place via neutron evaporation. On the other hand, the large β background prevents a clear identification of the associated γ-rays.

In this experiment, γ-γ coincidences and a proper Doppler correction made the study of the fusion evaporation channel possible. Fig. 4.43 presents the total projection of the prompt ($\approx$ 200 ns) γ-γ matrix (see Fig. 3.15).

In the case of reaction on the ^{98}Rb beam component, the compound nucleus ^{105}Zr* is produced at $\approx$ 40 MeV of excitation energy with a cross section of the order of 250 mb, as predicted by the CASCADE code [73]. The main residues is ^{100}Zr and it corresponds to the 5n-evaporation channel. According to the calculations, it is populated with about 80% of probability. Other weaker residues (associated to 3 and 4 neutron evaporation) are also expected with probability of the order of 10 % each, although they could not be resolved in this experiment. The red spectrum of Fig. 4.43 shows the non Doppler corrected events, while the black one corresponds to a Doppler correction using the average valueβ = 0.07. It can be noticed that by Doppler correcting the events, the $2^+ \rightarrow 0^+$ transition at 212 keV in ^{100}Zr can be clearly seen and isolated from the β-background which is distributed along the spectrum. In coincidence with the 212 keV γ-ray, the yrast band in ^{100}Zr can be seen up to 8 $\hbar$, as shown in the inset of the figure, where the 625 keV γ-line corresponding to the decay of the 8^+ states at 1687 keV is clearly visible.

Since the reaction occurred with an energy around the Coulomb barrier for Rb (Z=37), the cross section for fusion on ^{98}Sr (Z=38) is slightly lower than in the case of ^{98}Rb ($\approx$ 100 mb). The expected residue ^{101}Nb (4n channel from the compound ^{105}Nb), which is supposed to collect most of the decay flux (92 %) according to CASCADE, can be barely seen in Fig. 4.43 in correspondence with the Doppler corrected γ line at 119 keV (($7/2^+$) $\rightarrow$ ($5/2^+$) decay). Due to the large background at these energies, it is partially hidden and its γ coincidences can not be clearly studied.

Similar considerations may be made concerning fusion on ^{19}F, the other nucleus in the target. In this case, fusions on both ^{98}Rb and ^{98}Sr beam components are strongly below the Coulomb barrier and they can not be studied in this experiment.

These results demonstrate the possibility to study fusion-evaporation reactions also with radioactive beams at low intensities, although an extra tagging, such as neutrons detection, would be of great help to improve the selectivity of weakest channels.

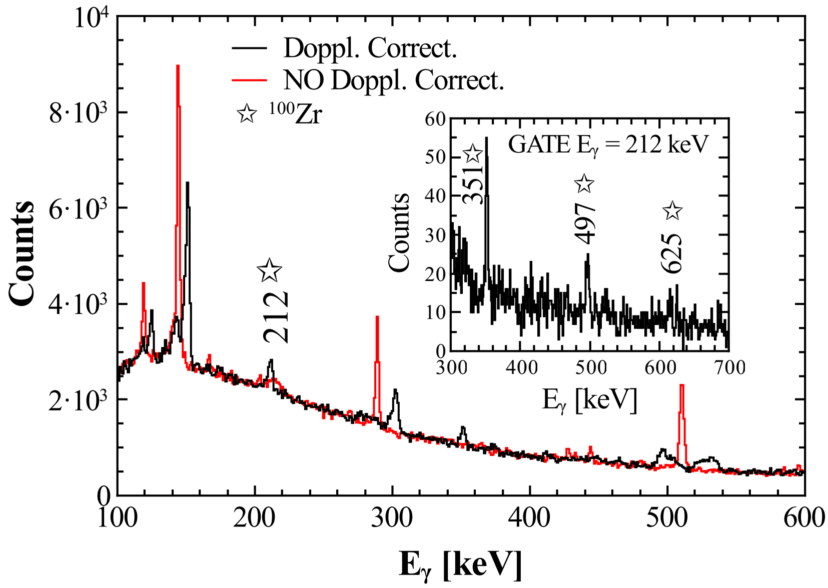

Figure 4.43: Projection of the prompt (≈ 200 ns) γ-γ coincidence matrix with and without Doppler correction (black and red lines, respectively). In the Doppler corrected spectrum, the $2^+ \rightarrow 0^+$ transition of ^{100}Zr, at 212 keV, can be seen, corresponding to the 5n residue of the fusion-evaporation reaction channel. Inset: projection of the γ-γ coincidence matrix gated on the 212 keV line, showing the relevant coincidences between yrast transitions of ^{100}Zr (labeled by stars). The last observed γ-ray at 625 keV corresponds to the $8^+ \rightarrow 6^+$ decay.

Conclusions and outlook

In this work, the reaction ^{98}Rb+^{7}Li, performed at ISOLDE [29, 53], was studied at the Coulomb barrier (i.e. ≈ 3 MeV/A) to investigate cluster-transfer reaction channels (triton- and α-transfer) in the neutron-rich mass region A $\approx$ 100. For the first time, cluster-transfer reactions in inverse kinematics were employed with neutron-rich radioactive beams, as a possible tool to perform γ spectroscopy studies in exotic neutron-rich nuclei. The experimental technique relied on particle-γ coincidence measurements, using the MINIBALL-T-REX setup [30–32]. The emitted complementary charged particle was detected in the Si telescopes detection system T-REX, in coincidence with the γ-cascade of the residue, detected in the Ge array MINIBALL. Cluster-transfers channels were studied in terms of both γ-spectroscopy and reaction dynamics.

The reactions channels of interest were selected by tagging on either α particles or tritons (triton- and α-transfer, respectively), resulting in a very clean trigger on the final reaction products. In fact, it was shown that the measured γ spectra gated on either α particles or tritons were uniquely associated to cluster-transfer channels, confirming the selectivity based on this experimental technique. Moreover, due to the very inverse kinematics, the reaction products are forward focused within a very narrow cone ($\approx 3°$), implying that an average Doppler correction can be applied to the γ decay of interest.

The measured γ spectra showed that states in the residual nucleus up to 6 $\hbar$ for triton transfer and 4 $\hbar$ for alpha transfer were observed. The γ spectroscopy performed in this work was limited by the short beam time ($\approx$ 80 h), the low beam intensity ($\approx 2{\cdot}10^4$ pps) and the beam impurity (a strong ^{98}Sr component was observed in the beam) which fragmented the total intensity on different reaction channels.

The residue distributions following the neutron evaporation were studied as a function of the excitation energy and different spin distributions of the nucleus produced in the transfer. The excitation energy was reconstructed assuming a two-body process and following the two-body kinematics. γ spectra were analysed in coincidence with different excitation energies, showing a clear dependence of the yield of evaporated neutrons on the excitation energy of the final systems. In particular, it was shown that the final residues can be selected according to the measured γ-yields, providing a powerful tool to separate different isotopes populated within the same cluster-transfer channel.

The experimental results were also compared with theoretical predictions performed with the CASCADE code [73]. The neutron evaporation was studied considering an excitation energy of the final system, as measured in this experiment, and as a function of different spin distributions. It was shown that the best fit of the data can be obtained considering a spin distribution centred in 20 $\hbar$, in the case of triton-transfer, and around 15 $\hbar$ in the case of α-transfer. This fact, together with the measured high excitation energy of the final products, confirms that cluster-transfer reactions are a suitable mechanism to populate states at medium-high energy and spin.

Cluster-transfer cross sections were studied qualitatively in terms of excitation energy and angular distributions, for both the triton- and α-transfer case. A direct transfer of a cluster-like particle was assumed and the calculations were performed by the FRESCO code [34], using a 1-step DWBA approximation [33]. In order to take into account the high excitation energy of the final systems, above the core-cluster separation energy, two different approaches were considered to describe the wave function of the final states lying in the continuum. In the first case, a weakly-bound approximation was considered so that the final states were forced to be bound with a very weak binding energy. In the second case, a proper discretization of the continuum was performed. Both approaches showed that the excitation energy distribution can be well reproduced, especially in the first case. Moreover, the relative cross section between triton- and α-transfer is well predicted. These results indicate that cluster-transfer reactions can be qualitatively described in terms of a direct process, although further studies are needed to be able to predict cross sections on absolute scale.

The results presented in this thesis show that cluster-transfer reactions can be used to populate neutron-rich nuclei at medium-high energy and spin and the analysis performed demonstrate the validity of the experimental technique.

This work can serve as a benchmark for future experiments, where cluster-transfer reactions may be used to explore different exotic regions of the chart of nuclides.

Three possible cases which can take advantages from such a reaction mechanism and from the same experimental technique, as discussed in this work, are here presented. Their aim is to study the structure of neutron-rich i) ^{96}Y, ii) ^{106}Nb and iii) ^{133}Sb nuclei, using radioactive beams produced at facilitates of new generation such as SPES [78], CARIBU [79] and HIE-ISOLDE [80]. Fig. 4.44 shows the three regions of interest.

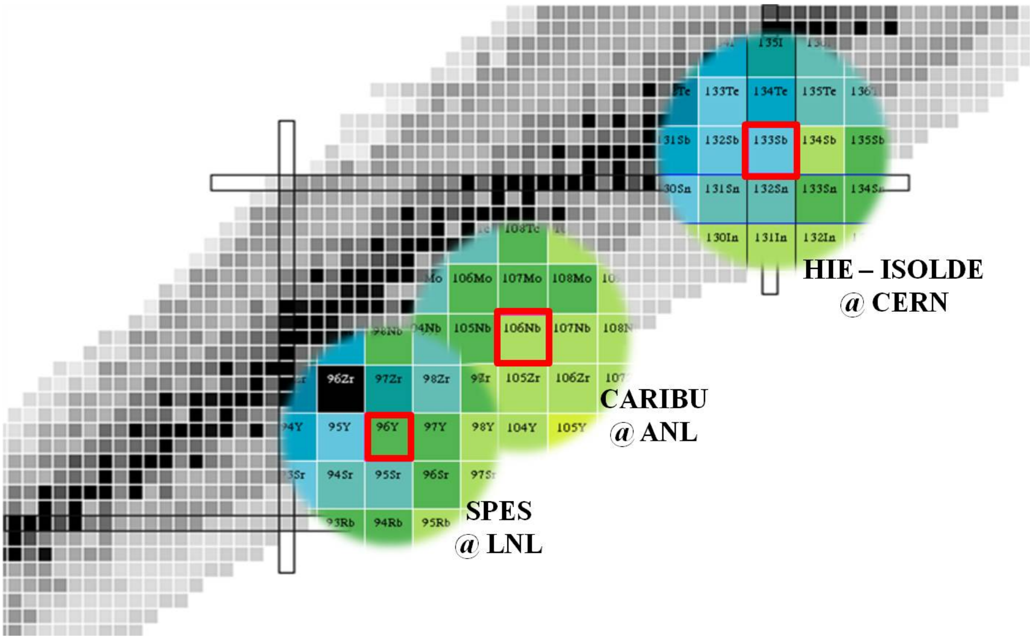

Figure 4.44: Mass regions around ^{96}Y, ^{106}Nb and ^{133}Sb nuclei that may be studied by cluster-transfer reactions at new facilities such as SPES [78], CARIBU [79] and HIE-ISOLDE [80].

i) *Oblate deformations in* ^{96}*Y:*

The aim of this experiment is to identify in the ^{96}Y nucleus the gamma-ray cascades feeding the spherical 0^+ ground state and the β-decaying oblate-deformed 8^+ isomer. ^{96}Y can be produced by using cluster transfer reactions (triton-transfer) of ^{95}Sr on ^{7}Li. The ^{98}Y products will evaporate mostly 2 neutrons leading to ^{96}Y.

^{96}Y is placed in a mass region where a transition from a partial sub-shell closure at N=56 and a stable deformation at N=60 is expected to take place [46]. The ground state of ^{96}Y displays a rather spherical shape while the isomeric 8^+ state is oblate deformed [81]. By studying the γ cascades one will be able to establish the distributions of the entry states, from which γ-rays feeding the two very different structures, originate. In particular, the collective structure based on the oblate shape should be a very unique example of rotational oblate deformed near-yrast structure. Moreover, quasi-continuum γ-ray spectra associated with the paths towards the ground state and deformed isomeric state will be obtained and used to investigate the robustness of the deformation with angular momentum and excitation energy.

This experiment could be performed using the ^{95}Sr beams, that will be produced at the ISOL SPES facility of Laboratori Nazionali di Legnaro of INFN (Italy) [78]. The detection system could be given by the Ge array GALILEO [82] or AGATA [83, 84] to detect the γ-rays coupled to the TRACE [85] Si detectors to detect charged particles. In addition, an high-efficiency scintillator spectrometer, such as HECTOR+ [86] or PARIS [87], can be used to perform multiplicity measurements and γ spectroscopy in the continuum.

ii) *Shape-coexistences in the neutron-rich* ^{106}*Nb:*

The aim of this experiment is to identify states above the 0.84 μs isomer at 205 keV in ^{106}Nb and, in addition, to extend information on excited bands in ^{105}Nb beyond the few yrast states known so far, by using the cluster-transfer reaction (triton-transfer) of ^{104}Zr on ^{7}Li. The ^{107}Nb product will evaporate 1 or 2 neutrons leading to ^{106}Nb or ^{105}Nb, respectively, at medium-high energy and spin.

^{106}Nb lies at the border of the region where prolate-oblate shape transitions are expected [88]. Potential energy surface calculations for a single-neutron-single-proton configurations predict a prolate ground state with a small triaxial deformation. Moreover, the same calculations indicate that an oblate minimum at around 1 MeV is also expected [89,90]. If these minimum exists, collective structures built on it may be expected, and if the minimum is deep enough, it may give rise to isomeric states. The observation of any of these structures would be very important for validating the theoretical model.

This experiment could be performed at the CARIBU facility of Argonne National Laboratory (ANL) [79], where radioactive nuclei are produced by the spontaneous fission of ^{252}Cf and then accelerated by the ATLAS linear accelerator [91]. ^{104}Zr beams are unique of the CARIBU facility since Zr cannot be extracted from an ISOL-type target. The reaction can be studied by using the Ge array GAMMASPHERE [92] or GRETINA [93] to detect the γ-rays, coupled to the Washington University Phoswich Wall [94] to detect charged particles.

iii) *Particle-vibration coupling around the doubly-magic ^{132}Sn:*

The aim of this experiment is to investigate the one-valence-proton ^{133}Sb nucleus by using the cluster-transfer reaction of ^{132}Sn on ^{7}Li. The nucleus of interest will be populated by transfer of a triton into ^{132}Sn, forming the excited ^{135}Sb nucleus, followed by the emission of an α particle. The ^{135}Sb product will evaporate 2 neutrons (with the highest probability) leading to ^{133}Sb.

Aim of the experiment is to locate states arising from the coupling of the valence proton of ^{133}Sb to the collective low-lying phonon excitations of the doubly-magic ^{132}Sn (in particular the 3^-) [35]. According to calculations in the weak-coupling approach [95], these states lie at excitation energies, above yrast, 4 MeV and higher, in the spin interval 1/2 - 19/2 $\hbar$, within the region populated by the cluster transfer reaction. The results will be used to perform an advanced test of different types of nuclear interactions which are usually employed in the description of particle-phonon excitations. States arising from couplings of proton with simpler core excitations, involving few nucleons only, will also be accessible, providing a very specific test of effective shell model interactions across the shell gaps.

This experiment is approved and it will be performed in 2016 at HIE-ISOLDE at CERN [80], using the same MINIBALL-T-REX setup [30–32] employed in the present work.

APPENDIX A

Non-relativistic two-body kinematics

In this Appendix, the non-relativistic two-body kinematics of nuclear binary reactions will be discussed. Particular attention will be given to the relation between the centre-of-mass coordinates and the laboratory coordinates and the transformation of scattering angles and cross sections from one frame-of-reference to the other. The main equations used to perform the analysis presented in this work will be illustrated [33,48–50].

A.1 Non-relativistic binary reactions

Binary reactions are a two-body process, namely only two nuclei are involved both in the entrance and exit channels. In general, it is written as

$$a + A = b + B \tag{A.1.1}$$

where a and A are the projectile and the target, respectively, and b and B are the exit reaction products.

In binary direct reaction, the reaction products are very similar to the projectile and target nuclei, and they are usually called projectile-like and target-like particles.

In a system where the target nucleus is at rest, the reaction can be assumed non-relativistic if the incident projectile velocity v_a is such that

$$\beta = \frac{v_\mathrm{a}}{c} \ll 1 \tag{A.1.2}$$

Typically, low-energy reactions are performed with $\beta < 0.1$

A.2 Q-value

Mass and energy are among those quantities which are conserved in a nuclear reaction. In a system where the target nucleus is at rest, the conservation of the total energy implies

$$m_a c^2 + T_a + m_A c^2 = m_b c^2 + T_b + E_b^{\text{ex}} + m_B c^2 + T_B + E_B^{\text{ex}} \tag{A.2.1}$$

where m denotes the mass, T the kinetic energy and E^{ex} the excitation energy. An important parameter to characterize the reaction is the Q-value defined as

$$Q := T_f - T_i \tag{A.2.2}$$

where T_i and T_f are the total kinetic energy before and after the reaction. According to Eq. A.2.1, it can be written as

$$Q = (m_a + m_A - m_b - m_B)c^2 - (E_b^{\text{ex}} + E_B^{\text{ex}}) = Q_0 - E_{\text{tot}}^{\text{ex}} \tag{A.2.3}$$

where Q_0 is the mass difference and $E_{\text{tot}}^{\text{ex}}$ is the total excitation energy of the system after the reaction. The Q-value can be either positive or negative according to the reaction channel. In the elastic scattering, Q = 0, since both the mass difference and the final excitation energies are zero. Inelastic scattering is always characterized by $Q < 0$, since masses don't change but $E_{\text{tot}}^{\text{ex}} > 0$. Transfer reactions can have both positive and negative Q-values.

A.3 Laboratory and center-of-mass frames of reference

In the laboratory (fixed) frame of reference, the projectile a with incident momentum $\mathbf{p}_a = m_a \mathbf{v}_a$ impinges on a target at rest ($v_A = 0$). After the collision, the nucleus b scatters at the angle ϑ_b^{lab} with momentum $\mathbf{p}_b = m_b \mathbf{v}_b$ while the recoil scatters at the angle ϑ_B^{lab} with momentum $\mathbf{p}_B = m_B \mathbf{v}_B$. The angles are determined with respect to the beam direction. In this case, the beam energy is given by

$$E_a = \frac{1}{2} m_a v_a^2 \tag{A.3.1}$$

In the center of mass system, the projectile and the target move with initial velocities

$$v_a^{\text{cm}} = \frac{m_A}{m_a + m_A} v_a \tag{A.3.2}$$

$$v_A^{\text{cm}} = -\frac{m_a}{m_a + m_A} v_a \tag{A.3.3}$$

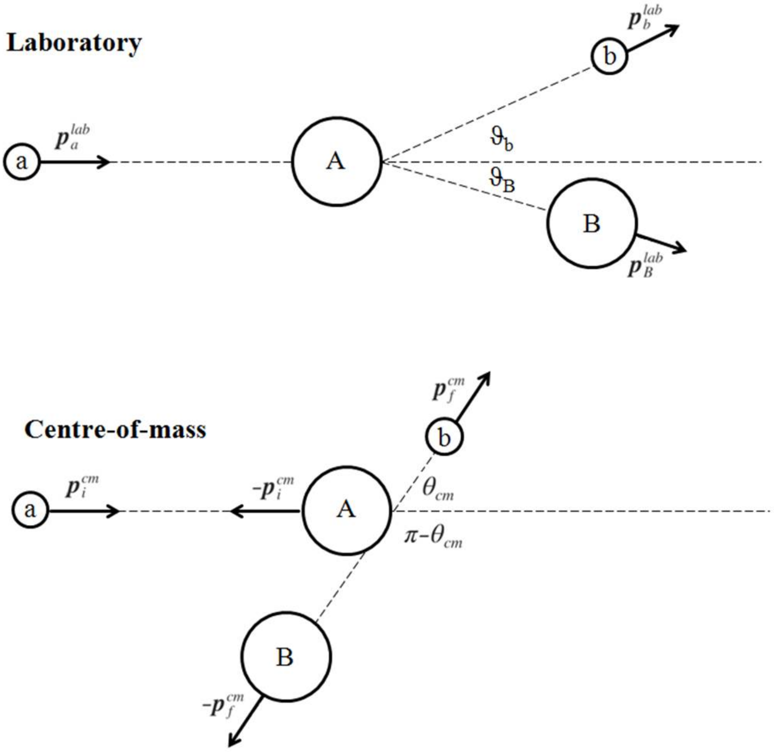

Figure A.1: Velocities and angles in the laboratory (top) and centre-of-mass (bottom) frames of reference for a binary reaction a + A = b + B, with A assumed at rest before the collision.

and relative momentum and energy

$$P_i^{\text{cm}} = \mu v_a \tag{A.3.4}$$

$$E_{\text{cm}} = \frac{1}{2}\mu v_a^2 \tag{A.3.5}$$

being μ the reduced mass

$$\mu = \frac{m_a m_A}{m_a + m_A} \tag{A.3.6}$$

The total energy of the system can be written as the sum of the energy of the relative motion (Eq. A.3.2) and the energy of the motion of the center of mass. In the case of a stationary target, the velocity of the center of mass $\tilde{v}$ is such that

$$\tilde{v} \equiv v_A^{\text{cm}} \tag{A.3.7}$$

After the collision, the two nuclei scatter with momentum $\mathbf{P}_f^{\text{cm}}$ and $-\mathbf{P}_f^{\text{cm}}$ at angles θ_{cm} and $\pi - \theta_{\text{cm}}$.

A.4 Two-body kinematics

The relations between energies after the collision and scattering angles have analytic expressions that can be derived by energy and momentum conservation. In this section, the most important equations for the light fragment b and the heavy fragment B will be reported.

It is useful to define the following quantities

$$\alpha = \frac{m_a m_B E_a}{(E_a + Q)(m_a + m_A)(m_b + m_B)} \tag{A.4.1}$$

$$\beta = \frac{m_a m_b E_a}{(E_a + Q)(m_a + m_A)(m_b + m_B)} \tag{A.4.2}$$

$$\gamma = \frac{m_A m_b}{(m_a + m_A)(m_b + m_B)} \left(1 + \frac{m_a Q}{m_A(E_a + Q)}\right) \tag{A.4.3}$$

$$\delta = \frac{m_A m_B}{(m_a + m_A)(m_b + m_B)} \left(1 + \frac{m_a Q}{m_A(E_a + Q)}\right) \tag{A.4.4}$$

Note that $\alpha + \beta + \delta + \gamma = 1$ and $\alpha\gamma = \beta\delta$.

A.4.1 Laboratory frame-of-reference

In the laboratory frame of reference, the energy E_b depends on the scattering angle ϑ_b as follows

$$E_b(\vartheta_b) = \beta(E_a + Q)\left(\cos\vartheta_b \pm \sqrt{\frac{\delta}{\beta} - \sin^2\vartheta_b}\right)^2 \tag{A.4.5}$$

where only the plus sign must be used unless $\beta > \delta$, in which case

$$\vartheta_b^{max} = \sin^{-1}\sqrt{\delta/\beta} \tag{A.4.6}$$

The energy E_B is related to the scattering angle ϑ_B by

$$E_B(\vartheta_B) = \alpha(E_a + Q)\left(\cos\vartheta_B \pm \sqrt{\frac{\gamma}{\alpha} - \sin^2\vartheta_B}\right)^2 \tag{A.4.7}$$

where only the plus sign must be used unless $\alpha > \gamma$, in which case

$$\vartheta_B^{max} = \sin^{-1}\sqrt{\gamma/\alpha} \tag{A.4.8}$$

ϑ_B and ϑ_b are related by

$$\sin\vartheta_B = \sqrt{\frac{m_b E_b}{m_B E_B}}\sin\vartheta_b \tag{A.4.9}$$

The Q-value of the reaction can be calculated by

$$Q = \frac{m_b + m_B}{m_B} E_b - \frac{m_B - m_a}{m_B} E_a - \frac{2\sqrt{m_a m_b E_a E_b}}{m_B} \cos \vartheta_b \tag{A.4.10}$$

A.4.2 Centre-of-mass frame-of-reference

In the center-of-mass frame of reference, only one angle θ_{cm} is involved. It is related to ϑ_b by

$$\sin \theta_{\text{cm}} = \frac{E_b}{\delta(E_a + Q)} \sin \vartheta_b \tag{A.4.11}$$

E_b and E_B depend on θ_{cm} as follows

$$E_b(\theta_{\text{cm}}) = (E_a + Q)(\beta + \delta + 2\sqrt{\alpha\gamma} \cos \theta_{\text{cm}}) \tag{A.4.12}$$

$$E_B(\theta_{\text{cm}}) = (E_a + Q)(\alpha + \gamma - 2\sqrt{\alpha\gamma} \cos \theta_{\text{cm}}) \tag{A.4.13}$$

A.5 Cross sections

Cross sections in the laboratory frame-of-reference differ from those in the centre-of-mass system. The transformation from one system to the other is governed by the *Jacobian*, a function of the scattering angle of the starting frame of reference. In general, to link the system 1 to the system 2, it can be used

$$\left(\frac{d\sigma}{d\Omega}(\theta_2) \right)_2 = J(\theta_1) \left(\frac{d\sigma}{d\Omega}(\theta_1) \right)_1 \tag{A.5.1}$$

To convert cross sections from the center-of-mass system to the laboratory one with respect to the final nucleus b, the *Jacobian* is

$$J(\theta_{\text{cm}}) = \frac{\sqrt{(1 + \omega_b^2 + 2\omega_b \cos \theta_{\text{cm}})^3}}{|1 + \omega_b \cos \theta_{\text{cm}}|} \tag{A.5.2}$$

where

$$\omega_b = \sqrt{\frac{m_a m_b}{m_A m_B} \frac{E_a}{E_a + Q}} \tag{A.5.3}$$

and ϑ_b can be related to θ_{cm} by

$$\tan \vartheta_b = \frac{\sin \theta_{cm}}{\cos \theta_{cm} + \omega_b} \tag{A.5.4}$$

To pass from the laboratory system with respect to the nucleus b to the center-of-mass, the *Jacobian* takes the form

$$J(\vartheta_b) = |1 - \eta_b \cos \vartheta_b| \sqrt{1 + \eta_b^2 - 2\eta_b \cos \vartheta_b} \tag{A.5.5}$$

where

$$\eta_b = \sqrt{\frac{m_a m_b}{(m_a + m_A)^2} \frac{E_a}{E_b}} \tag{A.5.6}$$

In order to convert cross sections from one frame-of-reference to the the other with respect to the recoil nucleus B, it must be used

$$\omega_B = \sqrt{\frac{m_a m_B}{m_A m_b} \frac{E_a}{E_a + Q}} \tag{A.5.7}$$

$$\eta_B = \sqrt{\frac{m_a m_B}{(m_a + m_A)^2} \frac{E_a}{E_B}} \tag{A.5.8}$$

APPENDIX B

Statistical model for particle decay

In this Appendix, the statistical model for particle decay based on the Hauser-Feshbach theory discussed in Sec. 4.6.1 will be presented [96]. Such a theory is founded on the assumption that the decaying nucleus has reached a statistical equilibrium before cooling down by particle evaporation.

B.1 Decay probability

Considering a nucleus in the initial excited state $E^{\mathrm{x}}_{\mathrm{i}}$ with spin J_{i}, the decay rate $R_p(E^{\mathrm{x}}_{\mathrm{f}})$ of emission of a particle p with kinetic energy ϵ_p, leaving the final nucleus in an excited state $E^{\mathrm{x}}_{\mathrm{f}}$ with spin J_{f}, is

$$R_p(E^{\mathrm{x}}_{\mathrm{f}})d\epsilon_p = \frac{1}{2\pi\hbar}\frac{\rho(E^{\mathrm{x}}_{\mathrm{f}}, J_{\mathrm{f}}, A_{\mathrm{f}})}{\rho(E^{\mathrm{x}}_{\mathrm{f}}, J_{\mathrm{i}}, A_{\mathrm{i}})}\sum_{S=|J_{\mathrm{f}}-s_p|}^{J_{\mathrm{f}}+s_p}\sum_{L=|J_{\mathrm{i}}-S|}^{J_{\mathrm{i}}+S} T^p_L(\epsilon_p)d\epsilon_p \tag{B.1.1}$$

where $\rho(E^{\mathrm{x}}, J, A)$ is the level density for states with excitation energy E^{x} and spin J, s_p is the spin of the emitted particle, L is the orbital angular momentum and S is the channel spin. The energies are connected by

$$E^{\mathrm{x}}_{\mathrm{i}} = E^{\mathrm{x}}_{\mathrm{f}} + \epsilon_p - B_p \tag{B.1.2}$$

where the latter term is the particle binding energy. $T^p_L(\epsilon_p)$ is the transmission coefficient for the scattering of particle p on the final nucleus.

Particle decay is therefore governed by the the transmission coefficients $T^p_L(\epsilon_p)$ and the level densities $\rho(E^{\mathrm{x}}, J, A)$. The former is usually obtained from optical potentials for neutron elastic scattering using average global parameters.

B.2 Level density

The level density for a nucleus with A particles at energy E^{x} and spin J is based on the back-shifted Fermi-gas model [97]

$$\rho(E^{\mathrm{x}}, J, A) = \frac{\sqrt{a}(2J+1)}{12\sqrt{\theta^3}(U+T)^2} e^{2\sqrt{aU}} \tag{B.2.1}$$

where a is the level density parameter, whose standard value is $8/A$ MeV^{-1}.
θ is the moment of inertia

$$\theta = \frac{2I_{\mathrm{rigid}}}{\hbar^2} \tag{B.2.2}$$

being I_{rigid} the rigid-body moment of inertia. U is the intrinsic excitation energy

$$U = E^{\mathrm{x}} - \Delta - E_{\mathrm{rot}} \tag{B.2.3}$$

where Δ is the paring energy and E_{rot} is the rotational energy

$$E_{\mathrm{rot}} = \frac{J(J+1)}{\theta'} \tag{B.2.4}$$

with

$$\theta' = \theta(1 + \delta J^2 + \delta' J^4) \tag{B.2.5}$$

the corrected moment of inertia for a deformable rotating liquid drop.
T is the nuclear temperature defined by

$$T := \left(\frac{\partial S}{\partial U}\right)^{-1} \tag{B.2.6}$$

where S is the entropy of the system

$$S := k_b \ln \rho(U) \tag{B.2.7}$$

The relation between U and T is given by

$$U = aT^2 - T \tag{B.2.8}$$

APPENDIX C

The FRESCO code

FRESCO is a coupled channels computer code written by I. J. Thompson [34]. The code can calculate any nuclear reaction which can be expressed in coupled channel form. Typically, all kind of direct reactions can be treated, such as elastic and inelastic scattering, transfer, break-up, knock-out etc. It is more suitable for low-energy reactions around the Coulomb barrier.

In this Appendix, the inputs used in this work to compute cluster-transfer cross section will be illustrated. Only the case of triton-transfer will be reported.

A typical FRESCO input for transfer reactions has usually a structure organized in input-cards as follows:

- &**FRESCO**: general parameters involved in the calculation
- &**PARTITION**: properties of the mass partitions defined
- &**STATES**: states included in each mass partitions
- &**POT**: potentials involved in the calculation
- &**OVERLAP**: overlaps of the wave functions of the states for each mass partition
- &**COUPLING**: couplings between the states in each mass partitions
- &**CFP**: spectroscopic factors for each state involved in the couplings

A finite range transfer using a 1-step DWBA approximation is performed requiring *iter = 1*, *iblock = 0* and *kind=7* in the &COUPLING.

In Sec. C.1, the input used to calculate the triton-transfer to weakly bound states with L = 3 will be illustrated. As discussed in Sec. 4.8.1, the final states above the core-cluster separation energy were forced to be bound states with a very small binding energy, which is defined in the &OVERLAP card as *be* = 0.01 MeV.

In Sec. C.2, the discretization of the continuum will be presented according to the description given in Sec. 4.8.2. The *bins* are defined in the &OVERLAP card with their number *nk* and their width *er*.

C.1 Weakly bound approximation

```
7Li(98Rb,101Sr)4He - TRITON TRANSFER - WEAKLY BOUND STATES - L=3
NAMELIST
&FRESCO hcm=0.08 rmatch=25. rintp=0.1 hnl=0.1 rnl=3.0 centre=-0.48
        jtmin=0.0 jtmax=40. absend=-0.005
        thmin=0.0 thmax=180.0 thinc=1.0 cutl=3.
        iter=1
        chans=1 smats=2 xstabl=1
        elab=244.0 /

&PARTITION namep="98Rb"  massp=97.941703   zp=37
           namet="7Li"   masst=7.016004    zt=3 qval=0.0 nex=1 /
&STATES jp=0   bandp=+1  ep=0.0   cpot=1   jt=1.5  bandt=-1  et=0.0 /
&PARTITION namep="101Sr" massp=100.940517  zp=38
           namet="4He"   masst=4.002603    zt=2 qval=13.587628 nex=51 /
&STATES jp=3.5 bandp=-1  ep=0.0   cpot=2   jt=0.0  bandt=+1  et=0.0 /
&STATES jp=3.5 bandp=-1  ep=0.5   cpot=2         copyt=1     /
&STATES jp=3.5 bandp=-1  ep=1.0   cpot=2         copyt=1     /
&STATES jp=3.5 bandp=-1  ep=1.5   cpot=2         copyt=1     /
&STATES jp=3.5 bandp=-1  ep=2.0   cpot=2         copyt=1     /
&STATES jp=3.5 bandp=-1  ep=2.5   cpot=2         copyt=1     /
&STATES jp=3.5 bandp=-1  ep=3.0   cpot=2         copyt=1     /
&STATES jp=3.5 bandp=-1  ep=3.5   cpot=2         copyt=1     /
&STATES jp=3.5 bandp=-1  ep=4.0   cpot=2         copyt=1     /
&STATES jp=3.5 bandp=-1  ep=4.5   cpot=2         copyt=1     /
&STATES jp=3.5 bandp=-1  ep=5.0   cpot=2         copyt=1     /
&STATES jp=3.5 bandp=-1  ep=5.5   cpot=2         copyt=1     /
&STATES jp=3.5 bandp=-1  ep=6.0   cpot=2         copyt=1     /
&STATES jp=3.5 bandp=-1  ep=6.5   cpot=2         copyt=1     /
&STATES jp=3.5 bandp=-1  ep=7.0   cpot=2         copyt=1     /
&STATES jp=3.5 bandp=-1  ep=7.5   cpot=2         copyt=1     /
&STATES jp=3.5 bandp=-1  ep=8.0   cpot=2         copyt=1     /
&STATES jp=3.5 bandp=-1  ep=8.5   cpot=2         copyt=1     /
&STATES jp=3.5 bandp=-1  ep=9.0   cpot=2         copyt=1     /
&STATES jp=3.5 bandp=-1  ep=9.5   cpot=2         copyt=1     /
&STATES jp=3.5 bandp=-1  ep=10.0  cpot=2         copyt=1     /
&STATES jp=3.5 bandp=-1  ep=10.5  cpot=2         copyt=1     /
```

```
&STATES jp=3.5 bandp=-1  ep=11.0  cpot=2         copyt=1     /
&STATES jp=3.5 bandp=-1  ep=11.5  cpot=2         copyt=1     /
&STATES jp=3.5 bandp=-1  ep=12.0  cpot=2         copyt=1     /
&STATES jp=3.5 bandp=-1  ep=12.5  cpot=2         copyt=1     /
&STATES jp=3.5 bandp=-1  ep=13.0  cpot=2         copyt=1     /
&STATES jp=3.5 bandp=-1  ep=13.5  cpot=2         copyt=1     /
&STATES jp=3.5 bandp=-1  ep=14.0  cpot=2         copyt=1     /
&STATES jp=3.5 bandp=-1  ep=14.5  cpot=2         copyt=1     /
&STATES jp=3.5 bandp=-1  ep=15.0  cpot=2         copyt=1     /
&STATES jp=3.5 bandp=-1  ep=15.5  cpot=2         copyt=1     /
&STATES jp=3.5 bandp=-1  ep=16.0  cpot=2         copyt=1     /
&STATES jp=3.5 bandp=-1  ep=16.5  cpot=2         copyt=1     /
&STATES jp=3.5 bandp=-1  ep=17.0  cpot=2         copyt=1     /
&STATES jp=3.5 bandp=-1  ep=17.5  cpot=2         copyt=1     /
&STATES jp=3.5 bandp=-1  ep=18.0  cpot=2         copyt=1     /
&STATES jp=3.5 bandp=-1  ep=18.5  cpot=2         copyt=1     /
&STATES jp=3.5 bandp=-1  ep=19.0  cpot=2         copyt=1     /
&STATES jp=3.5 bandp=-1  ep=19.5  cpot=2         copyt=1     /
&STATES jp=3.5 bandp=-1  ep=20.0  cpot=2         copyt=1     /
&STATES jp=3.5 bandp=-1  ep=20.5  cpot=2         copyt=1     /
&STATES jp=3.5 bandp=-1  ep=21.0  cpot=2         copyt=1     /
&STATES jp=3.5 bandp=-1  ep=21.5  cpot=2         copyt=1     /
&STATES jp=3.5 bandp=-1  ep=22.0  cpot=2         copyt=1     /
&STATES jp=3.5 bandp=-1  ep=22.5  cpot=2         copyt=1     /
&STATES jp=3.5 bandp=-1  ep=23.0  cpot=2         copyt=1     /
&STATES jp=3.5 bandp=-1  ep=23.5  cpot=2         copyt=1     /
&STATES jp=3.5 bandp=-1  ep=24.0  cpot=2         copyt=1     /
&STATES jp=3.5 bandp=-1  ep=24.5  cpot=2         copyt=1     /
&STATES jp=3.5 bandp=-1  ep=25.0  cpot=2         copyt=1     /
&partition /

&POT kp=1 ap=0.0 at=98.0 rc=1.3 /
&POT kp=1 type=1 shape=0
          p1=114.2 p2=1.286 p3=0.853 p4=15.643 p5=1.739 p6=0.809 /
&POT kp=2 ap=0.0 at=101.0 rc=1.3 /
&POT kp=2 type=1 shape=0
          p1=140.00 p2=1.2 p3=1.2 p4=10.000 p5=1.2 p6=1.2/
&POT kp=3 ap=0.0 at=4.0 rc=1.950 /
```

```
&POT kp=3 type=1 shape=2 p1=83.78 p2=0.0 p3=2.520 /
&POT kp=3 type=3 shape=2 p1=2.006 p2=0.0 p3=2.520 /
&POT kp=4 ap=0.0 at=98.0 rc=1.3 /
&POT kp=4 type=1 shape=0 p1=50.0 p2=1.25 p3=0.650 /
&pot /

&OVERLAP kn1=1   ic1=1 ic2=2 in=2 kind=0 nn=2 l=1 sn=0.5 j=1.5 kbpot=3
                 be=2.46670 isc=1  ipc=1 /
&OVERLAP kn1=2   ic1=1 ic2=2 in=1 kind=0 nn=4 l=3 sn=0.5 j=3.5 kbpot=4
                 be=16.0543 isc=1  ipc=1 /
&OVERLAP kn1=3   ic1=1 ic2=2 in=1 kind=0 nn=4 l=3 sn=0.5 j=3.5 kbpot=4
                 be=15.5543 isc=1  ipc=1 /
&OVERLAP kn1=4   ic1=1 ic2=2 in=1 kind=0 nn=4 l=3 sn=0.5 j=3.5 kbpot=4
                 be=15.0543 isc=1  ipc=1 /
&OVERLAP kn1=5   ic1=1 ic2=2 in=1 kind=0 nn=4 l=3 sn=0.5 j=3.5 kbpot=4
                 be=14.5543 isc=1  ipc=1 /
&OVERLAP kn1=6   ic1=1 ic2=2 in=1 kind=0 nn=4 l=3 sn=0.5 j=3.5 kbpot=4
                 be=14.0543 isc=1  ipc=1 /
&OVERLAP kn1=7   ic1=1 ic2=2 in=1 kind=0 nn=4 l=3 sn=0.5 j=3.5 kbpot=4
                 be=13.5543 isc=1  ipc=1 /
&OVERLAP kn1=8   ic1=1 ic2=2 in=1 kind=0 nn=4 l=3 sn=0.5 j=3.5 kbpot=4
                 be=13.0543 isc=1  ipc=1 /
&OVERLAP kn1=9   ic1=1 ic2=2 in=1 kind=0 nn=4 l=3 sn=0.5 j=3.5 kbpot=4
                 be=12.5543 isc=1  ipc=1 /
&OVERLAP kn1=10  ic1=1 ic2=2 in=1 kind=0 nn=4 l=3 sn=0.5 j=3.5 kbpot=4
                 be=12.0543 isc=1  ipc=1 /
&OVERLAP kn1=11  ic1=1 ic2=2 in=1 kind=0 nn=4 l=3 sn=0.5 j=3.5 kbpot=4
                 be=11.5543 isc=1  ipc=1 /
&OVERLAP kn1=12  ic1=1 ic2=2 in=1 kind=0 nn=4 l=3 sn=0.5 j=3.5 kbpot=4
                 be=11.0543 isc=1  ipc=1 /
&OVERLAP kn1=13  ic1=1 ic2=2 in=1 kind=0 nn=4 l=3 sn=0.5 j=3.5 kbpot=4
                 be=10.5543 isc=1  ipc=1 /
&OVERLAP kn1=14  ic1=1 ic2=2 in=1 kind=0 nn=4 l=3 sn=0.5 j=3.5 kbpot=4
                 be=10.0543 isc=1  ipc=1 /
&OVERLAP kn1=15  ic1=1 ic2=2 in=1 kind=0 nn=4 l=3 sn=0.5 j=3.5 kbpot=4
                 be=9.5543  isc=1  ipc=1 /
&OVERLAP kn1=16  ic1=1 ic2=2 in=1 kind=0 nn=4 l=3 sn=0.5 j=3.5 kbpot=4
                 be=9.0543  isc=1  ipc=1 /
```

```
&OVERLAP kn1=17  ic1=1 ic2=2 in=1 kind=0 nn=4 l=3 sn=0.5 j=3.5 kbpot=4
                 be=8.5543  isc=1  ipc=1 /
&OVERLAP kn1=18  ic1=1 ic2=2 in=1 kind=0 nn=4 l=3 sn=0.5 j=3.5 kbpot=4
                 be=8.0543  isc=1  ipc=1 /
&OVERLAP kn1=19  ic1=1 ic2=2 in=1 kind=0 nn=4 l=3 sn=0.5 j=3.5 kbpot=4
                 be=7.5543  isc=1  ipc=1 /
&OVERLAP kn1=20  ic1=1 ic2=2 in=1 kind=0 nn=4 l=3 sn=0.5 j=3.5 kbpot=4
                 be=7.0543  isc=1  ipc=1 /
&OVERLAP kn1=21  ic1=1 ic2=2 in=1 kind=0 nn=4 l=3 sn=0.5 j=3.5 kbpot=4
                 be=6.5543  isc=1  ipc=1 /
&OVERLAP kn1=22  ic1=1 ic2=2 in=1 kind=0 nn=4 l=3 sn=0.5 j=3.5 kbpot=4
                 be=6.0543  isc=1  ipc=1 /
&OVERLAP kn1=23  ic1=1 ic2=2 in=1 kind=0 nn=4 l=3 sn=0.5 j=3.5 kbpot=4
                 be=5.5543  isc=1  ipc=1 /
&OVERLAP kn1=24  ic1=1 ic2=2 in=1 kind=0 nn=4 l=3 sn=0.5 j=3.5 kbpot=4
                 be=5.0543  isc=1  ipc=1 /
&OVERLAP kn1=25  ic1=1 ic2=2 in=1 kind=0 nn=4 l=3 sn=0.5 j=3.5 kbpot=4
                 be=4.5543  isc=1  ipc=1 /
&OVERLAP kn1=26  ic1=1 ic2=2 in=1 kind=0 nn=4 l=3 sn=0.5 j=3.5 kbpot=4
                 be=4.0543  isc=1  ipc=1 /
&OVERLAP kn1=27  ic1=1 ic2=2 in=1 kind=0 nn=4 l=3 sn=0.5 j=3.5 kbpot=4
                 be=3.5543  isc=1  ipc=1 /
&OVERLAP kn1=28  ic1=1 ic2=2 in=1 kind=0 nn=4 l=3 sn=0.5 j=3.5 kbpot=4
                 be=3.0543  isc=1  ipc=1 /
&OVERLAP kn1=29  ic1=1 ic2=2 in=1 kind=0 nn=4 l=3 sn=0.5 j=3.5 kbpot=4
                 be=2.5543  isc=1  ipc=1 /
&OVERLAP kn1=30  ic1=1 ic2=2 in=1 kind=0 nn=4 l=3 sn=0.5 j=3.5 kbpot=4
                 be=2.0543  isc=1  ipc=1 /
&OVERLAP kn1=31  ic1=1 ic2=2 in=1 kind=0 nn=4 l=3 sn=0.5 j=3.5 kbpot=4
                 be=1.5543  isc=1  ipc=1 /
&OVERLAP kn1=32  ic1=1 ic2=2 in=1 kind=0 nn=4 l=3 sn=0.5 j=3.5 kbpot=4
                 be=1.0543  isc=1  ipc=1 /
&OVERLAP kn1=33  ic1=1 ic2=2 in=1 kind=0 nn=4 l=3 sn=0.5 j=3.5 kbpot=4
                 be=0.5543  isc=1  ipc=1 /
&OVERLAP kn1=34  ic1=1 ic2=2 in=1 kind=0 nn=4 l=3 sn=0.5 j=3.5 kbpot=4
                 be=0.0543  isc=1  ipc=1 /
&OVERLAP kn1=35  ic1=1 ic2=2 in=1 kind=0 nn=4 l=3 sn=0.5 j=3.5 kbpot=4
                 be=0.01    isc=1  ipc=1 /
```

```
&OVERLAP kn1=36  ic1=1 ic2=2 in=1 kind=0 nn=4 l=3 sn=0.5 j=3.5 kbpot=4
                 be=0.01  isc=1  ipc=1 /
&OVERLAP kn1=37  ic1=1 ic2=2 in=1 kind=0 nn=4 l=3 sn=0.5 j=3.5 kbpot=4
                 be=0.01  isc=1  ipc=1 /
&OVERLAP kn1=38  ic1=1 ic2=2 in=1 kind=0 nn=4 l=3 sn=0.5 j=3.5 kbpot=4
                 be=0.01    isc=1  ipc=1 /
&OVERLAP kn1=39  ic1=1 ic2=2 in=1 kind=0 nn=4 l=3 sn=0.5 j=3.5 kbpot=4
                 be=0.01 isc=1  ipc=1 /
&OVERLAP kn1=40  ic1=1 ic2=2 in=1 kind=0 nn=4 l=3 sn=0.5 j=3.5 kbpot=4
                 be=0.01  isc=1  ipc=1 /
&OVERLAP kn1=41  ic1=1 ic2=2 in=1 kind=0 nn=4 l=3 sn=0.5 j=3.5 kbpot=4
                 be=0.01  isc=1  ipc=1 /
&OVERLAP kn1=42  ic1=1 ic2=2 in=1 kind=0 nn=4 l=3 sn=0.5 j=3.5 kbpot=4
                 be=0.01  isc=1  ipc=1 /
&OVERLAP kn1=43  ic1=1 ic2=2 in=1 kind=0 nn=4 l=3 sn=0.5 j=3.5 kbpot=4
                 be=0.01  isc=1  ipc=1 /
&OVERLAP kn1=44  ic1=1 ic2=2 in=1 kind=0 nn=4 l=3 sn=0.5 j=3.5 kbpot=4
                 be=0.01  isc=1  ipc=1 /
&OVERLAP kn1=45  ic1=1 ic2=2 in=1 kind=0 nn=4 l=3 sn=0.5 j=3.5 kbpot=4
                 be=0.01  isc=1  ipc=1 /
&OVERLAP kn1=46  ic1=1 ic2=2 in=1 kind=0 nn=4 l=3 sn=0.5 j=3.5 kbpot=4
                 be=0.01  isc=1  ipc=1 /
&OVERLAP kn1=47  ic1=1 ic2=2 in=1 kind=0 nn=4 l=3 sn=0.5 j=3.5 kbpot=4
                 be=0.01  isc=1  ipc=1 /
&OVERLAP kn1=48  ic1=1 ic2=2 in=1 kind=0 nn=4 l=3 sn=0.5 j=3.5 kbpot=4
                 be=0.01  isc=1  ipc=1 /
&OVERLAP kn1=49  ic1=1 ic2=2 in=1 kind=0 nn=4 l=3 sn=0.5 j=3.5 kbpot=4
                 be=0.01  isc=1  ipc=1 /
&OVERLAP kn1=50  ic1=1 ic2=2 in=1 kind=0 nn=4 l=3 sn=0.5 j=3.5 kbpot=4
                 be=0.01  isc=1  ipc=1 /
&OVERLAP kn1=51  ic1=1 ic2=2 in=1 kind=0 nn=4 l=3 sn=0.5 j=3.5 kbpot=4
                 be=0.01  isc=1  ipc=1 /
&OVERLAP kn1=52  ic1=1 ic2=2 in=1 kind=0 nn=4 l=3 sn=0.5 j=3.5 kbpot=4
                 be=0.01  isc=1  ipc=1 /
&overlap /

&COUPLING icto=-2 icfrom=1 kind=7 ip1=0 ip2=0 ip3=0  /
&CFP in=2 ib=1   ia=1 kn=1   a=1.0 /
```

```
&CFP in=1 ib=1   ia=1 kn=2   a=1.0 /
&CFP in=1 ib=2   ia=1 kn=3   a=1.0 /
&CFP in=1 ib=3   ia=1 kn=4   a=1.0 /
&CFP in=1 ib=4   ia=1 kn=5   a=1.0 /
&CFP in=1 ib=5   ia=1 kn=6   a=1.0 /
&CFP in=1 ib=6   ia=1 kn=7   a=1.0 /
&CFP in=1 ib=7   ia=1 kn=8   a=1.0 /
&CFP in=1 ib=8   ia=1 kn=9   a=1.0 /
&CFP in=1 ib=9   ia=1 kn=10  a=1.0 /
&CFP in=1 ib=10  ia=1 kn=11  a=1.0 /
&CFP in=1 ib=11  ia=1 kn=12  a=1.0 /
&CFP in=1 ib=12  ia=1 kn=13  a=1.0 /
&CFP in=1 ib=13  ia=1 kn=14  a=1.0 /
&CFP in=1 ib=14  ia=1 kn=15  a=1.0 /
&CFP in=1 ib=15  ia=1 kn=16  a=1.0 /
&CFP in=1 ib=16  ia=1 kn=17  a=1.0 /
&CFP in=1 ib=17  ia=1 kn=18  a=1.0 /
&CFP in=1 ib=18  ia=1 kn=19  a=1.0 /
&CFP in=1 ib=19  ia=1 kn=20  a=1.0 /
&CFP in=1 ib=20  ia=1 kn=21  a=1.0 /
&CFP in=1 ib=21  ia=1 kn=22  a=1.0 /
&CFP in=1 ib=22  ia=1 kn=23  a=1.0 /
&CFP in=1 ib=23  ia=1 kn=24  a=1.0 /
&CFP in=1 ib=24  ia=1 kn=25  a=1.0 /
&CFP in=1 ib=25  ia=1 kn=26  a=1.0 /
&CFP in=1 ib=26  ia=1 kn=27  a=1.0 /
&CFP in=1 ib=27  ia=1 kn=28  a=1.0 /
&CFP in=1 ib=28  ia=1 kn=29  a=1.0 /
&CFP in=1 ib=29  ia=1 kn=30  a=1.0 /
&CFP in=1 ib=30  ia=1 kn=31  a=1.0 /
&CFP in=1 ib=31  ia=1 kn=32  a=1.0 /
&CFP in=1 ib=32  ia=1 kn=33  a=1.0 /
&CFP in=1 ib=33  ia=1 kn=34  a=1.0 /
&CFP in=1 ib=34  ia=1 kn=35  a=1.0 /
&CFP in=1 ib=35  ia=1 kn=36  a=1.0 /
&CFP in=1 ib=36  ia=1 kn=37  a=1.0 /
&CFP in=1 ib=37  ia=1 kn=38  a=1.0 /
&CFP in=1 ib=38  ia=1 kn=39  a=1.0 /
```

```
&CFP in=1 ib=39  ia=1 kn=40  a=1.0 /
&CFP in=1 ib=40  ia=1 kn=41  a=1.0 /
&CFP in=1 ib=41  ia=1 kn=42  a=1.0 /
&CFP in=1 ib=42  ia=1 kn=43  a=1.0 /
&CFP in=1 ib=43  ia=1 kn=44  a=1.0 /
&CFP in=1 ib=44  ia=1 kn=45  a=1.0 /
&CFP in=1 ib=45  ia=1 kn=46  a=1.0 /
&CFP in=1 ib=46  ia=1 kn=47  a=1.0 /
&CFP in=1 ib=47  ia=1 kn=48  a=1.0 /
&CFP in=1 ib=48  ia=1 kn=49  a=1.0 /
&CFP in=1 ib=49  ia=1 kn=50  a=1.0 /
&CFP in=1 ib=50  ia=1 kn=51  a=1.0 /
&CFP in=1 ib=51  ia=1 kn=52  a=1.0 /
&cfp /
&coupling /
```

C.2 Transfer to the continuum

```
7Li(98Rb,101Sr)4He - TRITON TRANSFER - STATES IN THE CONTINUUM
NAMELIST
&FRESCO hcm=0.1 rmatch=30. rintp=0.1 hnl=0.1 rnl=3.5 centre=-0.05
        jtmin=0.0 jtmax=40. absend=-0.005
        thmin=0.0 thmax=180.0 thinc=1.0 cutl=3. cutr=3.
        iter=1
        chans=1 smats=2 xstabl=1
        elab=244.0 /

&PARTITION namep="98Rb"  massp=97.941703     zp=37
           namet="7Li"   masst=7.016004      zt=3 qval=0.0 nex=1 /
&STATES jp=0   bandp=+1  ep=0.0000   cpot=1  jt=1.5  bandt=-1  et=0.0000 /
&PARTITION namep="101Sr" massp=100.940517    zp=38
           namet="4He"   masst=4.002603      zt=2 qval=13.587628 nex=61 /
&STATES jp=2.5 bandp=-1  ep=0.000    cpot=2  jt=0.0  bandt=+1   et=0.000 /
&STATES jp=0.5 bandp=+1  ep=16.7580  cpot=2       copyt=1       /
&STATES jp=0.5 bandp=+1  ep=17.2258  cpot=2       copyt=1       /
&STATES jp=0.5 bandp=+1  ep=17.8141  cpot=2       copyt=1       /
&STATES jp=0.5 bandp=+1  ep=18.5230  cpot=2       copyt=1       /
&STATES jp=0.5 bandp=+1  ep=19.3525  cpot=2       copyt=1       /
&STATES jp=0.5 bandp=+1  ep=20.3025  cpot=2       copyt=1       /
&STATES jp=0.5 bandp=+1  ep=21.3730  cpot=2       copyt=1       /
&STATES jp=0.5 bandp=+1  ep=22.5641  cpot=2       copyt=1       /
&STATES jp=0.5 bandp=+1  ep=23.8758  cpot=2       copyt=1       /
&STATES jp=0.5 bandp=+1  ep=25.3080  cpot=2       copyt=1       /
&STATES jp=1.5 bandp=-1  ep=16.7580  cpot=2       copyt=1       /
&STATES jp=1.5 bandp=-1  ep=17.2258  cpot=2       copyt=1       /
&STATES jp=1.5 bandp=-1  ep=17.8141  cpot=2       copyt=1       /
&STATES jp=1.5 bandp=-1  ep=18.5230  cpot=2       copyt=1       /
&STATES jp=1.5 bandp=-1  ep=19.3525  cpot=2       copyt=1       /
&STATES jp=1.5 bandp=-1  ep=20.3025  cpot=2       copyt=1       /
&STATES jp=1.5 bandp=-1  ep=21.3730  cpot=2       copyt=1       /
&STATES jp=1.5 bandp=-1  ep=22.5641  cpot=2       copyt=1       /
&STATES jp=1.5 bandp=-1  ep=23.8758  cpot=2       copyt=1       /
&STATES jp=1.5 bandp=-1  ep=25.3080  cpot=2       copyt=1       /
&STATES jp=2.5 bandp=+1  ep=16.7580  cpot=2       copyt=1       /
```

```
&STATES jp=2.5 bandp=+1  ep=17.2258  cpot=2        copyt=1        /
&STATES jp=2.5 bandp=+1  ep=17.8141  cpot=2        copyt=1        /
&STATES jp=2.5 bandp=+1  ep=18.5230  cpot=2        copyt=1        /
&STATES jp=2.5 bandp=+1  ep=19.3525  cpot=2        copyt=1        /
&STATES jp=2.5 bandp=+1  ep=20.3025  cpot=2        copyt=1        /
&STATES jp=2.5 bandp=+1  ep=21.3730  cpot=2        copyt=1        /
&STATES jp=2.5 bandp=+1  ep=22.5641  cpot=2        copyt=1        /
&STATES jp=2.5 bandp=+1  ep=23.8758  cpot=2        copyt=1        /
&STATES jp=2.5 bandp=+1  ep=25.3080  cpot=2        copyt=1        /
&STATES jp=3.5 bandp=-1  ep=16.7580  cpot=2        copyt=1        /
&STATES jp=3.5 bandp=-1  ep=17.2258  cpot=2        copyt=1        /
&STATES jp=3.5 bandp=-1  ep=17.8141  cpot=2        copyt=1        /
&STATES jp=3.5 bandp=-1  ep=18.5230  cpot=2        copyt=1        /
&STATES jp=3.5 bandp=-1  ep=19.3525  cpot=2        copyt=1        /
&STATES jp=3.5 bandp=-1  ep=20.3025  cpot=2        copyt=1        /
&STATES jp=3.5 bandp=-1  ep=21.3730  cpot=2        copyt=1        /
&STATES jp=3.5 bandp=-1  ep=22.5641  cpot=2        copyt=1        /
&STATES jp=3.5 bandp=-1  ep=23.8758  cpot=2        copyt=1        /
&STATES jp=3.5 bandp=-1  ep=25.3080  cpot=2        copyt=1        /
&STATES jp=4.5 bandp=+1  ep=16.7580  cpot=2        copyt=1        /
&STATES jp=4.5 bandp=+1  ep=17.2258  cpot=2        copyt=1        /
&STATES jp=4.5 bandp=+1  ep=17.8141  cpot=2        copyt=1        /
&STATES jp=4.5 bandp=+1  ep=18.5230  cpot=2        copyt=1        /
&STATES jp=4.5 bandp=+1  ep=19.3525  cpot=2        copyt=1        /
&STATES jp=4.5 bandp=+1  ep=20.3025  cpot=2        copyt=1        /
&STATES jp=4.5 bandp=+1  ep=21.3730  cpot=2        copyt=1        /
&STATES jp=4.5 bandp=+1  ep=22.5641  cpot=2        copyt=1        /
&STATES jp=4.5 bandp=+1  ep=23.8758  cpot=2        copyt=1        /
&STATES jp=4.5 bandp=+1  ep=25.3080  cpot=2        copyt=1        /
&STATES jp=5.5 bandp=-1  ep=16.7580  cpot=2        copyt=1        /
&STATES jp=5.5 bandp=-1  ep=17.2258  cpot=2        copyt=1        /
&STATES jp=5.5 bandp=-1  ep=17.8141  cpot=2        copyt=1        /
&STATES jp=5.5 bandp=-1  ep=18.5230  cpot=2        copyt=1        /
&STATES jp=5.5 bandp=-1  ep=19.3525  cpot=2        copyt=1        /
&STATES jp=5.5 bandp=-1  ep=20.3025  cpot=2        copyt=1        /
&STATES jp=5.5 bandp=-1  ep=21.3730  cpot=2        copyt=1        /
&STATES jp=5.5 bandp=-1  ep=22.5641  cpot=2        copyt=1        /
&STATES jp=5.5 bandp=-1  ep=23.8758  cpot=2        copyt=1        /
```

```
&STATES jp=5.5 bandp=-1  ep=25.3080  cpot=2       copyt=1       /
&partition /
&POT kp=1 ap=0.0 at=98.0 rc=1.3 /
&POT kp=1 type=1 shape=0
          p1=114.2 p2=1.286 p3=0.853 p4=15.643 p5=1.739 p6=0.809 /
&POT kp=2 ap=0.0 at=101.0 rc=1.3 /
&POT kp=2 type=1 shape=0
          p1=140.00 p2=1.2 p3=1.2 p4=10.000 p5=1.2 p6=1.2/
&POT kp=3 ap=0.0 at=4.0 rc=1.950 /
&POT kp=3 type=1 shape=2 p1=83.78 p2=0.0 p3=2.520 /
&POT kp=3 type=3 shape=2 p1=2.006 p2=0.0 p3=2.520 /
&POT kp=4 ap=0.0 at=98.0 rc=1.3 /
&POT kp=4 type=1 shape=0 p1=50.0 p2=1.25 p3=0.650 /
&pot /


&OVERLAP kn1=1  ic1=1 ic2=2 in=2 kind=0 nn=2 l=1 sn=0.5 j=1.5 kbpot=3
                be=2.46670 isc=1  ipc=1 /
&OVERLAP kn1=2  ic1=1 ic2=2 in=1 kind=0 nn=5 l=3 sn=0.5 j=2.5 kbpot=4
                be=16.0543 isc=1  ipc=1 /
&OVERLAP kn1=3  ic1=1 ic2=2 in=1 kind=0 nn=0 l=0 sn=0.5 j=0.5 kbpot=4
                be=-0.7037 isc=4 ipc=1 nk=100 er=-0.4075 /
&OVERLAP kn1=4  ic1=1 ic2=2 in=1 kind=0 nn=0 l=0 sn=0.5 j=0.5 kbpot=4
                be=-1.1715 isc=4 ipc=1 nk=100 er=-0.5280 /
&OVERLAP kn1=5  ic1=1 ic2=2 in=1 kind=0 nn=0 l=0 sn=0.5 j=0.5 kbpot=4
                be=-1.7598 isc=4 ipc=1 nk=100 er=-0.6486 /
&OVERLAP kn1=6  ic1=1 ic2=2 in=1 kind=0 nn=0 l=0 sn=0.5 j=0.5 kbpot=4
                be=-2.4687 isc=4 ipc=1 nk=100 er=-0.7692 /
&OVERLAP kn1=7  ic1=1 ic2=2 in=1 kind=0 nn=0 l=0 sn=0.5 j=0.5 kbpot=4
                be=-3.2982 isc=4 ipc=1 nk=100 er=-0.8897 /
&OVERLAP kn1=8  ic1=1 ic2=2 in=1 kind=0 nn=0 l=0 sn=0.5 j=0.5 kbpot=4
                be=-4.2482 isc=4 ipc=1 nk=100 er=-1.0103 /
&OVERLAP kn1=9  ic1=1 ic2=2 in=1 kind=0 nn=0 l=0 sn=0.5 j=0.5 kbpot=4
                be=-5.3187 isc=4 ipc=1 nk=100 er=-1.1308 /
&OVERLAP kn1=10 ic1=1 ic2=2 in=1 kind=0 nn=0 l=0 sn=0.5 j=0.5 kbpot=4
                be=-6.5098 isc=4 ipc=1 nk=100 er=-1.2514 /
&OVERLAP kn1=11 ic1=1 ic2=2 in=1 kind=0 nn=0 l=0 sn=0.5 j=0.5 kbpot=4
                be=-7.8215 isc=4 ipc=1 nk=100 er=-1.3720 /
```

```
&OVERLAP kn1=12 ic1=1 ic2=2 in=1 kind=0 nn=0 l=0 sn=0.5 j=0.5 kbpot=4
                be=-9.2537 isc=4 ipc=1 nk=100 er=-1.4925 /
&OVERLAP kn1=13 ic1=1 ic2=2 in=1 kind=0 nn=0 l=1 sn=0.5 j=1.5 kbpot=4
                be=-0.7037 isc=4 ipc=1 nk=100 er=0.40750 /
&OVERLAP kn1=14 ic1=1 ic2=2 in=1 kind=0 nn=0 l=1 sn=0.5 j=1.5 kbpot=4
                be=-1.1715 isc=4 ipc=1 nk=100 er=-0.5280 /
&OVERLAP kn1=15 ic1=1 ic2=2 in=1 kind=0 nn=0 l=1 sn=0.5 j=1.5 kbpot=4
                be=-1.7598 isc=4 ipc=1 nk=100 er=-0.6486 /
&OVERLAP kn1=16 ic1=1 ic2=2 in=1 kind=0 nn=0 l=1 sn=0.5 j=1.5 kbpot=4
                be=-2.4687 isc=4 ipc=1 nk=100 er=-0.7692 /
&OVERLAP kn1=17 ic1=1 ic2=2 in=1 kind=0 nn=0 l=1 sn=0.5 j=1.5 kbpot=4
                be=-3.2982 isc=4 ipc=1 nk=100 er=-0.8897 /
&OVERLAP kn1=18 ic1=1 ic2=2 in=1 kind=0 nn=0 l=1 sn=0.5 j=1.5 kbpot=4
                be=-4.2482 isc=4 ipc=1 nk=100 er=-1.0103 /
&OVERLAP kn1=19 ic1=1 ic2=2 in=1 kind=0 nn=0 l=1 sn=0.5 j=1.5 kbpot=4
                be=-5.3187 isc=4 ipc=1 nk=100 er=-1.1308 /
&OVERLAP kn1=20 ic1=1 ic2=2 in=1 kind=0 nn=0 l=1 sn=0.5 j=1.5 kbpot=4
                be=-6.5098 isc=4 ipc=1 nk=100 er=-1.2514 /
&OVERLAP kn1=21 ic1=1 ic2=2 in=1 kind=0 nn=0 l=1 sn=0.5 j=1.5 kbpot=4
                be=-7.8215 isc=4 ipc=1 nk=100 er=-1.3720 /
&OVERLAP kn1=22 ic1=1 ic2=2 in=1 kind=0 nn=0 l=1 sn=0.5 j=1.5 kbpot=4
                be=-9.2537 isc=4 ipc=1 nk=100 er=-1.4925 /
&OVERLAP kn1=23 ic1=1 ic2=2 in=1 kind=0 nn=0 l=2 sn=0.5 j=2.5 kbpot=4
                be=-0.7037 isc=4 ipc=1 nk=100 er=0.40750 /
&OVERLAP kn1=24 ic1=1 ic2=2 in=1 kind=0 nn=0 l=2 sn=0.5 j=2.5 kbpot=4
                be=-1.1715 isc=4 ipc=1 nk=100 er=-0.5280 /
&OVERLAP kn1=25 ic1=1 ic2=2 in=1 kind=0 nn=0 l=2 sn=0.5 j=2.5 kbpot=4
                be=-1.7598 isc=4 ipc=1 nk=100 er=-0.6486 /
&OVERLAP kn1=26 ic1=1 ic2=2 in=1 kind=0 nn=0 l=2 sn=0.5 j=2.5 kbpot=4
                be=-2.4687 isc=4 ipc=1 nk=100 er=-0.7692 /
&OVERLAP kn1=27 ic1=1 ic2=2 in=1 kind=0 nn=0 l=2 sn=0.5 j=2.5 kbpot=4
                be=-3.2982 isc=4 ipc=1 nk=100 er=-0.8897 /
&OVERLAP kn1=28 ic1=1 ic2=2 in=1 kind=0 nn=0 l=2 sn=0.5 j=2.5 kbpot=4
                be=-4.2482 isc=4 ipc=1 nk=100 er=-1.0103 /
&OVERLAP kn1=29 ic1=1 ic2=2 in=1 kind=0 nn=0 l=2 sn=0.5 j=2.5 kbpot=4
                be=-5.3187 isc=4 ipc=1 nk=100 er=-1.1308 /
&OVERLAP kn1=30 ic1=1 ic2=2 in=1 kind=0 nn=0 l=2 sn=0.5 j=2.5 kbpot=4
                be=-6.5098 isc=4 ipc=1 nk=100 er=-1.2514 /
```

```
&OVERLAP kn1=31 ic1=1 ic2=2 in=1 kind=0 nn=0 l=2 sn=0.5 j=2.5 kbpot=4
                be=-7.8215 isc=4 ipc=1 nk=100 er=-1.3720 /
&OVERLAP kn1=32 ic1=1 ic2=2 in=1 kind=0 nn=0 l=2 sn=0.5 j=2.5 kbpot=4
                be=-9.2537 isc=4 ipc=1 nk=100 er=-1.4925 /
&OVERLAP kn1=33 ic1=1 ic2=2 in=1 kind=0 nn=0 l=3 sn=0.5 j=3.5 kbpot=4
                be=-0.7037 isc=4 ipc=1 nk=100 er=0.40750 /
&OVERLAP kn1=34 ic1=1 ic2=2 in=1 kind=0 nn=0 l=3 sn=0.5 j=3.5 kbpot=4
                be=-1.1715 isc=4 ipc=1 nk=100 er=-0.5280 /
&OVERLAP kn1=35 ic1=1 ic2=2 in=1 kind=0 nn=0 l=3 sn=0.5 j=3.5 kbpot=4
                be=-1.7598 isc=4 ipc=1 nk=100 er=-0.6486 /
&OVERLAP kn1=36 ic1=1 ic2=2 in=1 kind=0 nn=0 l=3 sn=0.5 j=3.5 kbpot=4
                be=-2.4687 isc=4 ipc=1 nk=100 er=-0.7692 /
&OVERLAP kn1=37 ic1=1 ic2=2 in=1 kind=0 nn=0 l=3 sn=0.5 j=3.5 kbpot=4
                be=-3.2982 isc=4 ipc=1 nk=100 er=-0.8897 /
&OVERLAP kn1=38 ic1=1 ic2=2 in=1 kind=0 nn=0 l=3 sn=0.5 j=3.5 kbpot=4
                be=-4.2482 isc=4 ipc=1 nk=100 er=-1.0103 /
&OVERLAP kn1=39 ic1=1 ic2=2 in=1 kind=0 nn=0 l=3 sn=0.5 j=3.5 kbpot=4
                be=-5.3187 isc=4 ipc=1 nk=100 er=-1.1308 /
&OVERLAP kn1=40 ic1=1 ic2=2 in=1 kind=0 nn=0 l=3 sn=0.5 j=3.5 kbpot=4
                be=-6.5098 isc=4 ipc=1 nk=100 er=-1.2514 /
&OVERLAP kn1=41 ic1=1 ic2=2 in=1 kind=0 nn=0 l=3 sn=0.5 j=3.5 kbpot=4
                be=-7.8215 isc=4 ipc=1 nk=100 er=-1.3720 /
&OVERLAP kn1=42 ic1=1 ic2=2 in=1 kind=0 nn=0 l=3 sn=0.5 j=3.5 kbpot=4
                be=-9.2537 isc=4 ipc=1 nk=100 er=-1.4925 /
&OVERLAP kn1=43 ic1=1 ic2=2 in=1 kind=0 nn=0 l=4 sn=0.5 j=4.5 kbpot=4
                be=-0.7037 isc=4 ipc=1 nk=100 er=0.40750 /
&OVERLAP kn1=44 ic1=1 ic2=2 in=1 kind=0 nn=0 l=4 sn=0.5 j=4.5 kbpot=4
                be=-1.1715 isc=4 ipc=1 nk=100 er=-0.5280 /
&OVERLAP kn1=45 ic1=1 ic2=2 in=1 kind=0 nn=0 l=4 sn=0.5 j=4.5 kbpot=4
                be=-1.7598 isc=4 ipc=1 nk=100 er=-0.6486 /
&OVERLAP kn1=46 ic1=1 ic2=2 in=1 kind=0 nn=0 l=4 sn=0.5 j=4.5 kbpot=4
                be=-2.4687 isc=4 ipc=1 nk=100 er=-0.7692 /
&OVERLAP kn1=47 ic1=1 ic2=2 in=1 kind=0 nn=0 l=4 sn=0.5 j=4.5 kbpot=4
                be=-3.2982 isc=4 ipc=1 nk=100 er=-0.8897 /
&OVERLAP kn1=48 ic1=1 ic2=2 in=1 kind=0 nn=0 l=4 sn=0.5 j=4.5 kbpot=4
                be=-4.2482 isc=4 ipc=1 nk=100 er=-1.0103 /
&OVERLAP kn1=49 ic1=1 ic2=2 in=1 kind=0 nn=0 l=4 sn=0.5 j=4.5 kbpot=4
                be=-5.3187 isc=4 ipc=1 nk=100 er=-1.1308 /
```

```
&OVERLAP kn1=50 ic1=1 ic2=2 in=1 kind=0 nn=0 l=4 sn=0.5 j=4.5 kbpot=4
                be=-6.5098 isc=4 ipc=1 nk=100 er=-1.2514 /
&OVERLAP kn1=51 ic1=1 ic2=2 in=1 kind=0 nn=0 l=4 sn=0.5 j=4.5 kbpot=4
                be=-7.8215 isc=4 ipc=1 nk=100 er=-1.3720 /
&OVERLAP kn1=52 ic1=1 ic2=2 in=1 kind=0 nn=0 l=4 sn=0.5 j=4.5 kbpot=4
                be=-9.2537 isc=4 ipc=1 nk=100 er=-1.4925 /
&OVERLAP kn1=53 ic1=1 ic2=2 in=1 kind=0 nn=0 l=5 sn=0.5 j=5.5 kbpot=4
                be=-0.7037 isc=4 ipc=1 nk=100 er=0.40750 /
&OVERLAP kn1=54 ic1=1 ic2=2 in=1 kind=0 nn=0 l=5 sn=0.5 j=5.5 kbpot=4
                be=-1.1715 isc=4 ipc=1 nk=100 er=-0.5280 /
&OVERLAP kn1=55 ic1=1 ic2=2 in=1 kind=0 nn=0 l=5 sn=0.5 j=5.5 kbpot=4
                be=-1.7598 isc=4 ipc=1 nk=100 er=-0.6486 /
&OVERLAP kn1=56 ic1=1 ic2=2 in=1 kind=0 nn=0 l=5 sn=0.5 j=5.5 kbpot=4
                be=-2.4687 isc=4 ipc=1 nk=100 er=-0.7692 /
&OVERLAP kn1=57 ic1=1 ic2=2 in=1 kind=0 nn=0 l=5 sn=0.5 j=5.5 kbpot=4
                be=-3.2982 isc=4 ipc=1 nk=100 er=-0.8897 /
&OVERLAP kn1=58 ic1=1 ic2=2 in=1 kind=0 nn=0 l=5 sn=0.5 j=5.5 kbpot=4
                be=-4.2482 isc=4 ipc=1 nk=100 er=-1.0103 /
&OVERLAP kn1=59 ic1=1 ic2=2 in=1 kind=0 nn=0 l=5 sn=0.5 j=5.5 kbpot=4
                be=-5.3187 isc=4 ipc=1 nk=100 er=-1.1308 /
&OVERLAP kn1=60 ic1=1 ic2=2 in=1 kind=0 nn=0 l=5 sn=0.5 j=5.5 kbpot=4
                be=-6.5098 isc=4 ipc=1 nk=100 er=-1.2514 /
&OVERLAP kn1=61 ic1=1 ic2=2 in=1 kind=0 nn=0 l=5 sn=0.5 j=5.5 kbpot=4
                be=-7.8215 isc=4 ipc=1 nk=100 er=-1.3720 /
&OVERLAP kn1=62 ic1=1 ic2=2 in=1 kind=0 nn=0 l=5 sn=0.5 j=5.5 kbpot=4
                be=-9.2537 isc=4 ipc=1 nk=100 er=-1.4925 /
&overlap /

&COUPLING icto=-2 icfrom=1 kind=7 ip1=0 ip2=0 ip3=0  /
&CFP in=2 ib=1   ia=1 kn=1   a=1.0 /
&CFP in=1 ib=1   ia=1 kn=2   a=1.0 /
&CFP in=1 ib=2   ia=1 kn=3   a=1.0 /
&CFP in=1 ib=3   ia=1 kn=4   a=1.0 /
&CFP in=1 ib=4   ia=1 kn=5   a=1.0 /
&CFP in=1 ib=5   ia=1 kn=6   a=1.0 /
&CFP in=1 ib=6   ia=1 kn=7   a=1.0 /
&CFP in=1 ib=7   ia=1 kn=8   a=1.0 /
&CFP in=1 ib=8   ia=1 kn=9   a=1.0 /
```

```
&CFP in=1 ib=9   ia=1 kn=10  a=1.0 /
&CFP in=1 ib=10  ia=1 kn=11  a=1.0 /
&CFP in=1 ib=11  ia=1 kn=12  a=1.0 /
&CFP in=1 ib=12  ia=1 kn=13  a=1.0 /
&CFP in=1 ib=13  ia=1 kn=14  a=1.0 /
&CFP in=1 ib=14  ia=1 kn=15  a=1.0 /
&CFP in=1 ib=15  ia=1 kn=16  a=1.0 /
&CFP in=1 ib=16  ia=1 kn=17  a=1.0 /
&CFP in=1 ib=17  ia=1 kn=18  a=1.0 /
&CFP in=1 ib=18  ia=1 kn=19  a=1.0 /
&CFP in=1 ib=19  ia=1 kn=20  a=1.0 /
&CFP in=1 ib=20  ia=1 kn=21  a=1.0 /
&CFP in=1 ib=21  ia=1 kn=22  a=1.0 /
&CFP in=1 ib=22  ia=1 kn=23  a=1.0 /
&CFP in=1 ib=23  ia=1 kn=24  a=1.0 /
&CFP in=1 ib=24  ia=1 kn=25  a=1.0 /
&CFP in=1 ib=25  ia=1 kn=26  a=1.0 /
&CFP in=1 ib=26  ia=1 kn=27  a=1.0 /
&CFP in=1 ib=27  ia=1 kn=28  a=1.0 /
&CFP in=1 ib=28  ia=1 kn=29  a=1.0 /
&CFP in=1 ib=29  ia=1 kn=30  a=1.0 /
&CFP in=1 ib=30  ia=1 kn=31  a=1.0 /
&CFP in=1 ib=31  ia=1 kn=32  a=1.0 /
&CFP in=1 ib=32  ia=1 kn=33  a=1.0 /
&CFP in=1 ib=33  ia=1 kn=34  a=1.0 /
&CFP in=1 ib=34  ia=1 kn=35  a=1.0 /
&CFP in=1 ib=35  ia=1 kn=36  a=1.0 /
&CFP in=1 ib=36  ia=1 kn=37  a=1.0 /
&CFP in=1 ib=37  ia=1 kn=38  a=1.0 /
&CFP in=1 ib=38  ia=1 kn=39  a=1.0 /
&CFP in=1 ib=39  ia=1 kn=40  a=1.0 /
&CFP in=1 ib=40  ia=1 kn=41  a=1.0 /
&CFP in=1 ib=41  ia=1 kn=42  a=1.0 /
&CFP in=1 ib=42  ia=1 kn=43  a=1.0 /
&CFP in=1 ib=43  ia=1 kn=44  a=1.0 /
&CFP in=1 ib=44  ia=1 kn=45  a=1.0 /
&CFP in=1 ib=45  ia=1 kn=46  a=1.0 /
&CFP in=1 ib=46  ia=1 kn=47  a=1.0 /
```

```
&CFP in=1 ib=47  ia=1 kn=48  a=1.0 /
&CFP in=1 ib=48  ia=1 kn=49  a=1.0 /
&CFP in=1 ib=49  ia=1 kn=50  a=1.0 /
&CFP in=1 ib=50  ia=1 kn=51  a=1.0 /
&CFP in=1 ib=51  ia=1 kn=52  a=1.0 /
&CFP in=1 ib=52  ia=1 kn=53  a=1.0 /
&CFP in=1 ib=53  ia=1 kn=54  a=1.0 /
&CFP in=1 ib=54  ia=1 kn=55  a=1.0 /
&CFP in=1 ib=55  ia=1 kn=56  a=1.0 /
&CFP in=1 ib=56  ia=1 kn=57  a=1.0 /
&CFP in=1 ib=57  ia=1 kn=58  a=1.0 /
&CFP in=1 ib=58  ia=1 kn=59  a=1.0 /
&CFP in=1 ib=59  ia=1 kn=60  a=1.0 /
&CFP in=1 ib=60  ia=1 kn=61  a=1.0 /
&CFP in=1 ib=61  ia=1 kn=62  a=1.0 /
&cfp /
&coupling /
```

APPENDIX D

Papers

Part of the work presented in this thesis is published in *Acta Physics Polonica B* [98]. A paper discussing all the results is in preparation and it will be submitted to *Physical Review C*.

Vol. 45 (2014) *ACTA PHYSICA POLONICA B* No 2

γ SPECTROSCOPY OF NEUTRON-RICH NUCLEI WITH $A \approx 100$ PRODUCED BY CLUSTER TRANSFER REACTIONS AT REX-ISOLDE*

S. Bottoni[a,b,d], S. Leoni[a,b], B. Fornal[c], R. Raabe[d], G. Benzoni[b]
A. Bracco[a,b], F.C.L. Crespi[a,b], A. Morales[b], B. Bednarczyk[c]
N. Cieplicka[c], W. Królas[c], A. Maj[c], B. Szpak[c], M. Callens[d]
J. Bouma[d], J. Elseviers[d], F. Falvigny[d], R. Orlandi[d], K. Rusek[e]
P. Reiter[f], M. Seidlitz[f], S. Klupp[g], D. Mücher[g], G. Georgiev[h]
D. Balabanski[i], M. Sferrazza[j], M. Kowalska[k], E. Rapisarda[k]

and the MINIBALL–T-REX Collaboration

[a]Università degli Studi di Milano, Milano, Italy
[b]INFN Sezione di Milano, Milano, Italy
[c]The H. Niewodniczański Institute of Nuclear Physics, Kraków, Poland
[d]Instituut voor Kern- en Stralingsfysisca, KU Leuven, Leuven, Belgium
[e]Heavy Ion Laboratory, University of Warsaw, Warszawa, Poland
[f]Institut für Kernphysik der Universität zu Köln, Köln, Germany
[g]Physik Department, Technische Universität München, München, Germany
[h]CSNSM, Orsay, France
[i]IRNE-BAS, Sofia, Bulgaria
[j]Université Libre de Bruxelles, Bruxelles, Belgium
[k]ISOLDE, CERN, Geneve, Switzerland

(Received November 19, 2013)

In this work, we present an exploratory experiment performed at REX-ISOLDE to investigate neutron-rich Sr, Y and Zr nuclei around mass $A = 100$ by cluster transfer reactions of radioactive ^{98}Rb/^{98}Sr beams on a ^{7}Li target. The goal of the experiment is to test the potential of cluster-transfer mechanism to study the low-lying structure of neutron-rich nuclei, performing, as a first case, a γ-spectroscopy study of the structure in deformed nuclei beyond $N = 60$ populated, so far, only via β decay and spontaneous fission experiments.

DOI:10.5506/APhysPolB.45.343
PACS numbers: 25.70.Hi, 29.30.Kv, 21.10.Re

---

* Presented at the XXXIII Mazurian Lakes Conference on Physics, Piaski, Poland, September 1–7, 2013.

1. Introduction

Neutron-rich nuclei play an important role in the study of nuclear structure and shell evolution towards the neutron drip line. During the last decade, the employment of radioactive ion beams made it possible to investigate new isotopes, not accessible by stable beam-target combinations. To study even more exotic regions of the nuclide chart, new experimental techniques must be developed to face the new challenges of modern nuclear physics and take advantage of the new generation of radioactive ion beams facilities, such as HIE-ISOLDE, SPIRAL2, SPES, *etc.* It has been shown that multi-nucleon transfer reactions represent a powerful tool to study neutron-rich nuclei and, in particular, cluster-transfer reaction can be used to populate exotic nuclei at medium-high spin and excitation energy [1]. ^{7}Li is especially suitable for this purpose since it has a pronounced cluster structure, with an α and a t as components. Owing to a separation energy of 2.5 MeV, it easily breaks up and one of the two fragments has a sizeable probability to be captured. In this work, for the first time, the combination of a radioactive beam with cluster transfer reactions is presented. This technique may turn out to be very useful in future and the present experiment is meant as a first step of a research program aiming at γ-spectroscopy studies of the low-lying structures of neutron-rich nuclei produced employing cluster-transfer reactions.

2. Experiment

The experiment has been performed at REX-ISOLDE [2] accelerating a radioactive ^{98}Rb beam at 2.85 MeV/A, with an average intensity of 2×10^4 pps, on a 1.5 mg/cm^2 thick LiF target. Due to the short ^{98}Rb lifetime ($\approx$ 100 ms), a strong component of ^{98}Sr, the β-daughter of ^{98}Rb, has been observed in the beam. The experimental set-up was made by the HpGe array MINIBALL [3] coupled to the Si detector set-up T-REX [4] to measure γ-particle coincidences. The MINIBALL spectrometer is a high-resolution HpGe detector consisting of 24 six-fold segmented crystals, characterized by good spatial resolution. In the present experiment, it had an efficiency of 5% at 1 MeV. T-REX is a Si detector set-up optimized for transfer reactions in inverse kinematics and designed to be used in combination with the MINIBALL array. It is made by two CD detectors [5] placed at forward and backward angles plus eight lateral square detectors forming a barrel. In the present experiment, only the forward CD detector has been used in the new configuration at 22 mm from the target. This resulted in a wide angular coverage between 21° and 62°. The forward CD detector is made by two layers of 140 μm and 1500 μm, respectively, and it is used as a ΔE–E telescope to detect and identify charge particles.

3. Discussion

In the experiment, α or t transfer reactions were selected by detecting the complementary charged particle, t or α, in coincidence with the γ cascade. This gives a precise trigger on the final channel. Due to the high excitation energy, above the neutron threshold, γ emission is preceded by 2- or 3-neutron evaporation. Figure 1 shows the ΔE–E spectrum measured by the Si detectors. The most intense channels are the elastic scattering of ^{7}Li and protons (the latter were target contaminants), and the inelastic scattering of ^{7}Li and ^{19}F that cannot be identified since they were stopped in the ΔE detector. The channels of interest in this experiment correspond to the detection of α and t (t and α transfer respectively), whose events lie in the spectrum together with ^{7}Li elastic break-up. Thanks to the coincident detection of characteristic γ-rays, transfer events could be identified providing an estimate for the elastic break-up events of about 20% of the total α and t detected.

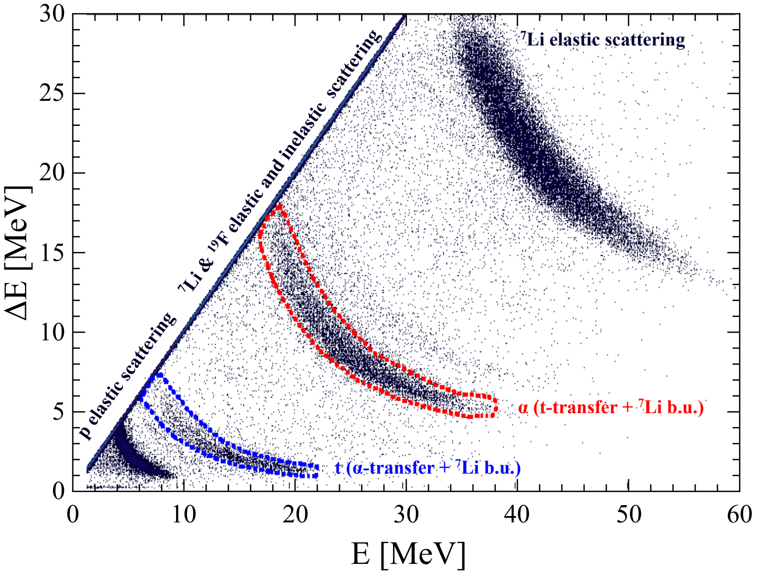

Fig. 1. E–ΔE spectrum measured by the Si telescopes of the T-REX setup. The regions delineated by dark grey/red and grey/blue dotted lines are associated to α and t particles, respectively. Elastic scattering of ^{7}Li and protons (contaminants on the LiF target) is also identified clearly, while diagonal events are associated to inelastic scattering of ^{7}Li and ^{19}F particles (fully stopped into the ΔE detector).

Figure 2 shows γ-rays measured in coincidence with α and t after 2- or 3-neutron evaporation. The spectra are Doppler corrected on an event-by-event basis. For this purpose, only the position of MINIBALL crystals has been used since the very inverse kinematics ensures that reaction products are limited in a small forward cone and travel downstream along the beam direction. Thus, to a first approximation, no recoil detection was needed for Doppler correction. Since reactions took place both on ^{98}Rb and ^{98}Sr (the two components of the beam), γ-rays in the two cases have been identified. While in the Rb case both 2- and 3-neutron evaporation chan-

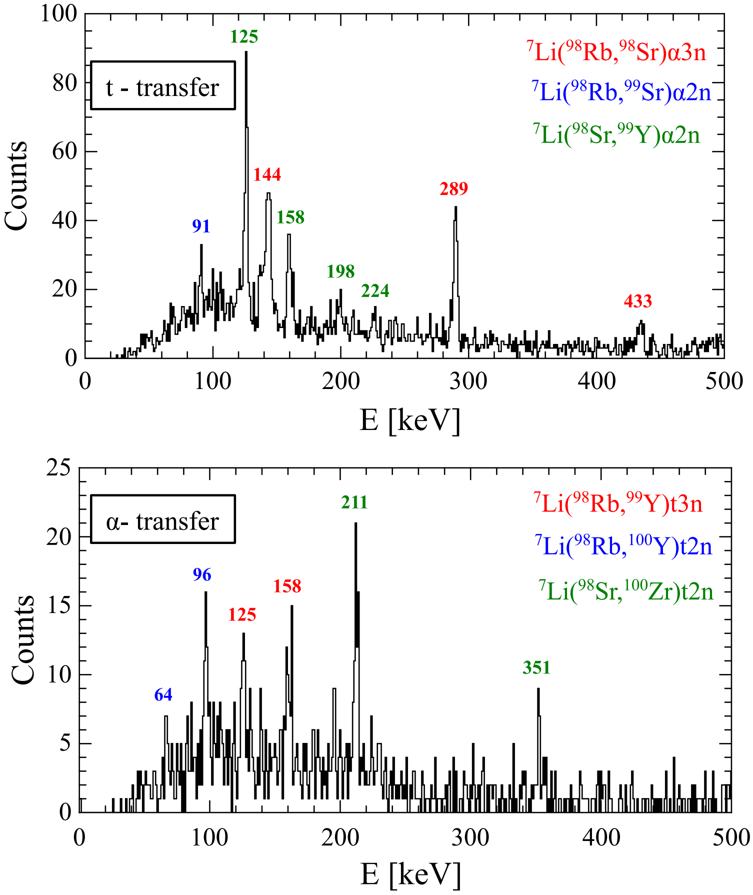

Fig. 2. γ-rays detected in coincidence with α (top panel) and t (bottom panel) corresponding to t and α transfer, respectively. In both spectra, transitions in Sr, Y and Zr isotopes can be identified and associated to different final channels, as explained in the text.

nels have been observed, in the Sr case only the $2n$-channel can be seen. By t-transfer on ^{98}Rb, $^{99-98}$Sr have been populated, while on ^{98}Sr the final channel is ^{99}Y. In the α-transfer channel, $^{99-100}$Y can be associated to reaction on ^{98}Rb, while on ^{98}Sr only ^{100}Zr can be observed. The difference in neutron evaporation can be associated to different neutron binding energy in the reaction products. The corresponding level schemes show that, in the t-transfer channel, states with spin up to $6\hbar$ have been populated, while in the α-transfer a maximum of $4\hbar$ has been seen. Despite the high excitation energy reached after the transfer (≈ 20 MeV in t-transfer and ≈ 15 MeV in α-transfer), only low-lying γ transitions belonging to the ground state bands have been measured after neutron evaporation. We speculate that the limited spin and excitation energy distribution here observed is probably related to the poor statistics collected in this first test experiment.

4. Conclusion

In this work, for the first time, the potential of cluster-transfer reactions in combination with radioactive beams as probes of nuclear structure properties has been studied. A test experiment has been performed at REX-ISOLDE using a ^{98}Rb/^{98}Sr beam on a ^{7}Li target. On the one hand, the analysis shows that particle-γ measurements make it possible to achieve a very clean identification of final reaction products. On the other hand, it has been seen that a large variety of nuclei has been populated with spin up to $6\hbar$, confirming the power of such a technique for nuclear structure studies. In the future, the same approach can be used to study even more exotic nuclei with a new generation of radioactive ion beams.

REFERENCES

[1] G.D. Dracoulis *et al.*, *J. Phys. G: Nucl. Part. Phys.* **23**, 1191 (1997).

[2] P. Van Duppen, K. Riisager, *J. Pyhs. G: Nucl. Part. Phys.* **38**, 024005 (2011).

[3] N. Warr *et al.*, *Eur. Phys. J.* **A49**, 40 (2013).

[4] V. Bildstein *et al.*, *Eur. Phys. J.* **A48**, 85 (2012).

[5] A.N. Ostrowski *et al.*, *Nucl. Instrum. Methods* **A480**, 448 (2002).

Bibliography

[1] T. Otsuka, Phys. Scr. **T152**, 014007 (2013).

[2] R. Kanungo, Phys. Scr. **T152**, 014002 (2013).

[3] A. Gade, Phys. Scr. **T152**, 014004 (2013).

[4] R. V. F. Janssens, Phys. Scr. **T152**, 014005 (2013).

[5] E. Khan, Phys. Scr. **T152**, 014008 (2013).

[6] H.Grawe, K.Langanke, G.Martinez-Pinedo, Rep. Prog. Phys. **70**, 1525 (2007).

[7] M. Huyse, Lect. Notes Phys. **651**, 1 (2004).

[8] R. Broda, J. Phys. G: Nucl. Part. Phys. **32**, R151 (2006).

[9] L. Corradi, G. Pollarolo and S. Szilner, J. Phys. G: Nucl. Part. Phys. **36**, 113101 (2009).

[10] D. Montanari et al., Phys. Rev. C. **85**, 044301 (2012).

[11] S. Bottoni et al., Phys. Rev. C. **85**, 064621 (2012).

[12] G. D. Dracoulis et al., J. Phys. G:Nucl. Part. Phys. **23**, 1191 (1997).

[13] R. M. Clark et al., Phys. Rev. C **72**, 054605 (2005).

[14] A. Jungclaus et al., Phys. Rev. C **67**, 034302 (2003).

[15] D. S. Judson et al., Phys. Rev. C **76**, 054306 (2007).

[16] H. Watanabe et al., Phys. Rev. C **79**, 024306 (2009).

[17] S. M. Mullins et al., Phys. Rev. C **61**, 044315 (2000).

[18] D. R. Tilley et al., Nucl. Phys. A **708**, 3 (2002).

[19] P.E. Hodgson, E. Betak, Phys. Rep. **374**, 1 (2003).

[20] F. K. Wohn et al., Phys. Rev. Lett. **51**, 873 (1983).

[21] G. Lhersonneau et al., Phys. Rev. C **65**, 024318 (2002).

[22] M.A.C. Hotchkins et al, Nucl. Phys. A 530, 111 (1991).

[23] G. Lhersonneau et al, Phys. Rev. C **63**, 054302 (2001).

[24] R. F. Petry et al, Phys. Rev. C **31**, 621 (1985).

[25] F. K. Wohn et al., Phys. Rev. C **36**, 1118 (1987).

[26] J. K. Hwang et al., Phys. Rev. C **58**, 3252 (1998).

[27] F. K. Wohn et al., Phys. Rev. C **33**, 677 (1986).

[28] J. K. Hwang et al, Phys. Rev. C **74**, 017303 (2006).

[29] E. Kugler, Hyperf. Int. **129**, 23 (2002).

[30] N. Warr et al., Eur. Phys. J. A **49**, 40 (2013).

[31] V. Bildstein et al., Prog. Part. Nucl. Phys. **59**, 386 (2007).

[32] V. Bildstein et al., Eur. Phys. J. A **48**, 85 (2012).

[33] I. J. Thompson and F. M. Nunes, Nuclear Reaction for Astrophysics, Cambridge University Press, 2009.

[34] I. J. Thomspon, Comput. Phys. Rep. **7**, 167 (1988).

[35] A. Bohr, B.R. Mottelson, Nuclear Structure, Vol. I and II, W.A. Benjamin, 1975.

[36] O. Sorlin and M.-G. Porquet, Prog. Part. Nucl. Phys. **61**, 602 (2008).

[37] K. Heyde and J. L. Wood, Rev. Mod. Phys **83**, 1467 (2011).

[38] D. Savran, T. Aumann, A. Zilges, Prog. Part Nuc. Phys. **70**, 245 (2013).

[39] E. M. Burbidge, Rev. Mod. Phys. **29**, 547 (1957).

[40] J. Äystö, J. Phys.: Conference Series **420**, 012045 (2013).

[41] R. Neugart, G. Neyens, Lect. Notes Phys. **700**, 135 (2006).

[42] B. Rubio, W. Gelletly, Lect. Notes Phys. **764**, 99 (2009).

[43] L. Corradi, J. Phys.: Conf. Ser. **282**, 012005 (2011).

[44] J. Wilczynski, Nucl. Phys. A **280**, 2 (1977).

[45] M. Dasgupta et al., Phys. Rev. C **66**, 041602R (2002).

[46] D. Bucurescu et al., J. Phys. G **7**, L123 (1981).

[47] N. Marginean et al., Phys. Rev. C **80**, 021301 (2009).

[48] G. R. Satchler, Direct nuclear reactions, Clarendon Press, 1983.

[49] R. Broglia and A. Winther, Heavy Ion Reactions, Redwood City, CA: Addison-Wesley, 1991.

[50] R. Bass, Nuclear Reactions with Heavy Ions, Springer-Verlag, 1980.

[51] B. Buck and A. A. Pilt, Nucl. Phys. A **280**, 133 (1977).

[52] W. R. Phillips, Rep. Prog. Phys **40**, 345407 (1977).

[53] P. Van Duppen and K. Riisager, J. Phys. G: Nucl. Part. Phys.**38**, 024005 (2011).

[54] ISOLDE Web-page, `http://www.isolde.web.cern.ch/`.

[55] National Nuclear Data Center, `http://www.nndc.bnl.gov/`.

[56] A. N. Ostrowski et al., Nucl. Instr. Meth. A **480**, 448 (2002).

[57] K. Wimmer, PhD thesis, Technische Universität München, (2010)

[58] J. Bouma, Master thesis, KU Leuven (2013).

[59] X-ray Instruments Associates, `http://www.xia.com/DGF-4C.html`.

[60] Mesytec, `http://www.mesytec.com`.

[61] R. Lutter et al., Nucl. Sci. **47**, 280 (2000).

[62] R. Lutter et al., Marabou Data Acquisition, `http://www.bl.physik.uni-muenchen.de/marabou/htmldoc/`, 2003.

[63] ROOT, A Data Analysis Framework, `http://root.cern.ch/drupal/`.

[64] S. Agostinelli et al., Nucl. Instrum. Methods A **506**, 250 (2003).

[65] G. F. Knoll, Radiation Detection and Measurement, Fourth Edition, Wiley, 2010.

[66] I.J. Kim, C.S. Park and H.D. Choi, Appl. Radiat. Isot. **58**, 227 (2003).

[67] N. Kesteloot, Master thesis, KU Leuven (2010).

[68] S. Klupp, Documentation of the calibration of the T-REX detectors and of MINIBALL (2012).

[69] J. Cook, Nucl. Phys. A **388**, 153 (1988)

[70] D. Cline. Annual Review of Nuclear and Particle Science **36**, 683 (1986).

[71] E. Clement, *Private Communication*.

[72] D. H. Luong et al., Phys. Lett. B **695**, 105 (2011).

[73] F. Puhlhofer, Nucl. Phys. A **280**, 267 (1977).

[74] J. Diriken, PhD thesis, KU Leuven 2013.

[75] A. Shrivastava et al., Phys. Lett. B **280**, 931 (2013).

[76] A. Diaz-Torres et al., Phys. Rev. Lett. **98**, 152701 (2007).

[77] B. Buck and A. C. Merchant, J. Phys. G: Nucl. Part. Phys. **14**, 211 (1988).

[78] G. Prete, A. Covello, SPES Technical Design Report 2008, INFN-LNL 223 `http://www.spes.lnl.infn.it/`.

[79] CARIBU, `http://www.phy.anl.gov/atlas/caribu/index.html`

[80] HIE-ISOLDE, `https://hie-isolde.web.cern.ch/hie-isolde/`

[81] B. Cheal et al., Phys. Lett. B **645**, 133 (2007)

[82] D. Mengoni et al., LNL Annual Report 2013, p.68.

[83] S. Akkoyun et al., Nucl. Instr. Methods A **668**, 26 (2012).

[84] A. Gadea et al., Nucl. Instr. Methods A **654**, 88 (2011).

[85] D. Mengoni et al., Nucl. Instr. Methods A **764**, 241 (2014).

[86] A. Giaz et al., Nucl. Instr. Methods A **729**, 910 (2013).

[87] A. Maj et al., Act. Phys. Pol. B **40**, 3 (2009).

[88] J.B. Snyder et al., Phys. Lett. B **723**, 61 (2013).

[89] F.R. Xu, et al., Phys. Rev. C **65**, 021303 (2002).

[90] F. Xu, et al., Phys. Lett. B **435**, 257 (1998).

[91] ATLAS, `http://www.phy.anl.gov/atlas/`

[92] I. Y. Lee, Nucl. Phys. A **520**, 641 (1990).

[93] I. Y. Lee, M. A. Deleplanque, K. Vetter, Rep. Prog. Phys **66**, 1095 (2003).

[94] Phoswich Wall
`http://www.chemistry.wustl.edu/~dgs/papers/PhosWall.pdf`

[95] G. Colò, *private communication*

[96] M. N. Harakeh and A. van der Woude, Giant Resonances, Fundamental High-Frequency Modes of Nuclear Excitation, Oxford Science Publications, 2006.

[97] W. Digl et al., Nucl. Phys. A **217**, 269 (1973).

[98] S. Bottoni et al., Act. Phys. Pol. B **45**, 343 (2014).